ENVIRONMENTALLY INDUCED CRACKING OF AN AL-ZN-MG-CU ALLOY

by

Francine S. Bovard

B.S. in Chemistry, University of Pittsburgh, 1998

Submitted to the Graduate Faculty of

School of Engineering in partial fulfillment

of the requirements for the degree of

Master of Science

University of Pittsburgh

2005

UNIVERSITY OF PITTSBURGH

SCHOOL OF ENGINEERING

This thesis was presented

by

Francine S. Bovard

It was defended on

December 7, 2005

and approved by

Dr. Jorg Wiezorek, PhD, Associate Professor, Materials Science and Engineering Dept.

Dr. James P. Moran, PhD, Alloy Technology Dept., Alcoa Technical Center

Dr. John A. Barnard, PhD, Professor and Chairman, Materials Science and Engineering Dept.

Thesis Advisor: Dr. Frederick S. Pettit, PhD, Professor Emeritus, Materials Science Dept.

ENVIRONMENTALLY INDUCED CRACKING OF AN AL-ZN-MG-CU ALLOY

Francine S. Bovard, M.S.

University of Pittsburgh, 2005

Although numerous mechanistic studies have been conducted over the past three decades that have correlated stress corrosion cracking (SCC) susceptibility with various parameters, a comprehensive mechanistic understanding of the SCC susceptibility of aluminum-magnesium-zinc-copper alloys is still lacking. Most mechanistic theories support either an anodic dissolution type of mechanism or a hydrogen embrittlement type of mechanism but within each of these two types of environmentally induced cracking (EIC) mechanisms there is little consensus on the mechanistic details. In fact, it seems likely that both anodic dissolution and hydrogen embrittlement phenomena play critical roles in the EIC of 7xxx aluminum alloys.

In this study, crack growth rates (CGR) in humid air (90%RH) were measured for AA7050 isothermally aged at 325˚F for various times. Ln-ln plots of CGR as a function of aging time show linear relationships. However, a distinct change in slope after ~10 hours of aging indicates a change in the rate controlling process for environmentally induced cracking (EIC). Transmission electron microscopy (TEM) analyses of AA7050 under the same aging conditions and mechanically strained 2% indicate that the change in the slope of the CGR behavior coincides with a transition in the morphology of the dislocation glide induced defect structures. For materials that exhibit slower CGR's homogeneously distributed dislocation structures are observed, while materials with more rapid CGR exhibit characteristically more localized band-like dislocation structures. This change in the morphology of dislocation structures after straining implies a critical change in the dominant interactions of gliding dislocations with the different populations of strengthening precipitates. Band-like dislocation structure morphologies have classically been interpreted as signs of planar slip behavior associated with particle shearing as the predominant mode of dislocation-precipitate interaction. The absence of the band-like dislocation structure morphologies for the materials with slower CGR's is consistent with more homogeneously distributed dislocation glide activity, presumably promoted by a change to an Orowan-type of by-passing mechanism as the dominant interaction between gliding dislocations

and the precipitate population. The possible implications of these results on the mechanistic understanding of EIC of Al-Mg-Zn-Cu alloys are discussed.

TABLE OF CONTENTS

LIST OF TABLES

LIST OF FIGURES

ACKNOWLEDGMENTS

1.0   INTRODUCTION

High strength 7xxx aluminum alloys have been used in the aerospace industry for many years. Numerous alloy composition and process developments have been made over the past 30 years to improve mechanical properties (i.e. strength, fracture toughness and fatigue resistance) while maintaining acceptable stress corrosion performance in these alloys. Many of the developments related to stress corrosion cracking (SCC) resistance have been made based largely on empirical knowledge. SCC of aluminum alloys is a very complex phenomenon that involves chemical, electrochemical, microstructural, and mechanical interactions. Although numerous mechanistic studies have been conducted over the past three decades that have successfully correlated SCC susceptibility with various parameters, a comprehensive mechanistic understanding of the SCC susceptibility of these aluminum-magnesium-zinc-copper alloys is still lacking. In the mechanistic studies that have been conducted, most of the theories developed support either an anodic dissolution type of mechanism or a hydrogen embrittlement type of mechanism, but within each of these two types of environmentally induced cracking (EIC) mechanisms there is little consensus on the mechanistic details. It seems likely that both anodic dissolution and hydrogen embrittlement phenomena play critical roles in the EIC of 7xxx aluminum alloys.

From 1996 to 2000, a multidisciplinary research program was carried out by researchers from University of Virginia, Lehigh University, and Alcoa Technical Center to study the EIC mechanisms in 7xxx series aluminum alloys. The results from this program verified and quantified the empirically known effects of Cu content and temper on crack growth kinetics.[1-3] Additionally, results of this program provided new evidence to support critical roles of both hydrogen embrittlement and anodic dissolution in the EIC of AA7050. The role of hydrogen was supported by establishing a correlation between hydrogen uptake and Stage II crack growth rates,[1] demonstrating Arrhenius dependence of crack growth in humid air,[2] and establishing a

correlation between the observed changes in the activation energy for bulk or volume diffusion of hydrogen with temper and the corresponding changes in activation energy for crack growth.[2] The primary evidence for an anodic dissolution contribution to the SCC process is the observation that development of an aggressive localized environment at the crack tip is a pre-requisite for high crack growth rates.[3] Near surface ingress of hydrogen also appeared to be surface controlled rather than diffusion controlled which implies that crack growth rate may be controlled by kinetic limitations of the surface reaction processes and/or mass transport processes within the localized crack chemistry that controls hydrogen adsorption.[1,2]

The microstructural characterization portion of this project was inconclusive.[4,5] Analytical electron microscopy (AEM) of precipitate particles in the AA7050 materials indicated some subtle differences in the composition of the precipitates, but failed to identify significant differences that could be correlated with the EIC behavior of these materials. The microstructural characterization effort in this program focused on chemical composition of the grain boundary precipitates, solute depleted zone, and matrix but did not characterize changes in size or coherency of the matrix precipitates, differences in sub-grain structure, dislocation structure and/or dislocation-particle interactions.

In 1969, Speidel[6] investigated the influence of the microstructure on susceptibility to intergranular stress corrosion cracking of AA7075. He found that aging conditions that had low resistance to SCC had long straight narrow slip bands and pile-ups at grain boundaries after deformation, while material conditions (both severely underaged and overaged) that had high resistance to SCC exhibited more homogeneous slip after deformation. These observations imply that the important factors in determining SCC susceptibility are related to matrix particle-dislocation interactions and the slip mechanism during plastic deformation. Several subsequent studies have also linked the environmental sensitivity of 7xxx type alloys to strain localization and slip planarity.[7-14] Additionally, several researchers[11-17] have demonstrated the effect of hydrogen on the enhanced mobility of dislocations in aluminum and have invoked hydrogen enhanced localized plasticity (HELP) mechanistic theories to explain the hydrogen embrittlement of aluminum. An earlier study on AA7075[18] observed the presence of dislocation networks in the SCC susceptible T6 temper and absence of these networks in the SCC resistant T7 temper.

This study is intended to follow up on some of the key findings and unanswered questions from the recent program conducted by the University of Virginia, Lehigh University,

and Alcoa. In this introductory section the relevant external literature is reviewed and a brief synopsis of the University of Virginia, Lehigh University, and Alcoa cooperative program is provided.

1.1   RELEVANT EXTERNAL LITERATURE

Many of the developments related to SCC resistance have been made based largely on empirical knowledge. SCC of aluminum alloys is a very complex phenomenon that involves chemical, electrochemical, microstructural, and mechanical interactions. Numerous studies have been conducted over the past three decades that have correlated SCC susceptibility with influences of alloy composition, thermo-mechanical processing conditions, mechanical factors, and chemical or electrochemical aspects of environmental exposures.

1.1.1   Factors that Influence EIC of 7xxx Alloys

Influences of alloy composition, thermo-mechanical processing conditions, mechanical factors, and chemical or electrochemical aspects of environmental exposures on EIC performance of 7xxx alloys have been established primarily based on experimental evidence. The influence of any one parameter however can be significantly impacted by the other factors. The complex nature of EIC is a result of the interdependence of all of these factors.

1.1.1.1   Alloy Composition

Within the 7xxx family of aluminum alloys the major alloying elements (Zn, Mg, and Cu) significantly influence the EIC performance of the materials. It is well known that the vulnerability to EIC susceptibility increases with the Zn and Mg content. It has also been demonstrated that the ratio of these elements (Zn:Mg) is of equal importance.[19-20] On the other hand, Cu additions are known to improve the EIC performance of Al-Zn-Mg alloys. While the Zn, Mg and Cu alloy composition parameters are by far the most influential on EIC

susceptibility, other alloy additions and impurities can have secondary influences on EIC behavior.

Gruhl[19,20] conducted a series of experiments on AlZnMg(Cu) alloys with a variety of compositions and thermal treatments and consequently a wide range of SCC susceptibility. He also used TEM EDX to measure the Zn, Mg and Cu concentrations in solid solution in the grain boundary area. The most significant result was that there was a definite linear relationship between the concentration of Zn in solid solution and the logarithm of the time to failure at a constant stress level (Figure 1.1). There was no apparent relation between Mg concentration in solid solution and SCC performance).

Gruhl's experiments on Al-Zn-Mg alloys with total solute content of Zn + Mg of 8%, indicated that EIC resistance was optimized by maintaining a Zn:Mg ratio of 2.7 to 2.9 as illustrated in Figure 1.2.[19-21] This is an atomic Zn:Mg ratio of ~1, which corresponds to the equilibrium line between the α-phase and T-phase in the Al-Zn-Mg phase diagram.[19] Addition of Cu improved the EIC resistance of Al-Zn-Mg alloys. In the peak-aged (T6) temper, addition of 1% Cu to the alloys with varying Zn:Mg ratios increases the 'duration of life' or EIC resistance by an order of magnitude as illustrated in Figure 1.2. Alloy development activities at Alcoa Technical Center have also indicated similar influences of the Zn:Mg ratio and the Cu content on SCC resistance. However, the optimal Zn/Mg ratio appeared to vary somewhat with variations in the total solute. For experimental alloys with Zn+Mg contents of ~4.5-6.0 the optimum Zn:Mg ratio was ~2.5 while for Zn+Mg contents somewhat greater than 8% the optimum Zn:Mg ratio appeared to be greater than 3.

Speidel and Hyatt[22] measured crack growth rates on AA7079 (4.3Zn, 2.25Mg, 0.6Cu), AA7075 (5.6Zn, 2.5Mg, 1.6Cu) and AA7178 (6.8Zn, 2.75Mg, 2.0Cu) in saturated aqueous NaCl as a function of over-aging time. The crack growth rates for the peak-aged temper (0 hours over-aging in Figure 1.3) of the higher Cu alloys are 2.5 to 3 orders of magnitude lower than that for the low Cu AA7079. The results in Figure 1.3 also indicate a significant influence of Cu on the effectiveness of over-aging treatments for improving EIC resistance. Over-aging of the higher Cu alloys (7075 and 7178) significantly decreased crack growth rates, but over-aging of the low Cu alloy, 7079, did not substantially decrease the crack growth rate. It is also interesting to note that there appears to be a distinct change in the slope of the curve after ~10 hours over-aging at 320°F (160°C) for the high Cu alloys implying that there may be two different rate controlling

processes involved. The differences in EIC behavior for these three commercial alloys have been attributed to differences in Cu content, but it should also be noted that the Zn and Mg levels in these three alloys are different which could also affect the crack growth rates. Although all three alloys have Zn:Mg ratios less than the optimum 2.7-3.0 range, the low Cu AA 7079 (Zn:Mg ratio = 1.9) also has a lower Zn:Mg ratio than the higher Cu alloys, AA7075 (Zn:Mg ratio = 2.2) and AA7178 (Zn:Mg ratio = 2.5) which could also contribute to differences in EIC susceptibility as previously discussed.

An earlier Alcoa supported project at the University of Virginia, conducted in 1981 by Sarkar, Marek and Starke, systematically evaluated the effect of Cu Content and heat treatment on the stress corrosion characteristics of Al-6Zn-2Mg-XCu (i.e. 7050 type) alloys.[17] The compositions, processing, and heat treatments were carefully controlled to obtain similar grain structures for all four Cu content variations so that the effects of Cu could be unambiguously evaluated. Their results indicated that Stage II crack growth rates of T651 temper decreases systematically as Cu content increases from 0 to 2.1% (Figure 1.4a). Over-aging significantly decreased crack growth rates, even for the 0% Cu alloy (Figure 1.4b), but only after considerable over-aging at a severe strength penalty.

Many investigations have correlated the size and or composition of precipitate free zones (PFZ) and/or solute depleted zones (SDZ) adjacent to the grain boundaries to SCC performance.[5, 23-29] The explanations provided for the influences of PFZ's and SDZ's contradict one another. Most of these studies indicate that the importance of the PFZ or SDZ is electrochemical. Thomas and Nutting[28] however observed that intercrystalline mechanical fractures of Al-Zn-Mg(Cu) alloys in peak aged condition was associated with preferential slip in the PFZ. They hypothesized that the stress concentration effects at the grain boundaries combined with the "soft" PFZ may allow dislocation movement to take place in the PFZ at stresses well below the macroscopic yield stress. McEvily et al.[29] also observed that the softness of the PFZ enhances localized plasticity at the grain boundary. Other studies indicate that they see no correlation between PFZ composition or width and SCC resistance.[30-32] The inconsistency of correlation between PFZ's and/or SDZ's and SCC resistance implies that while a PFZ may be a contributing factor in some instances, they may not be an essential microstructural feature in the EIC mechanism.
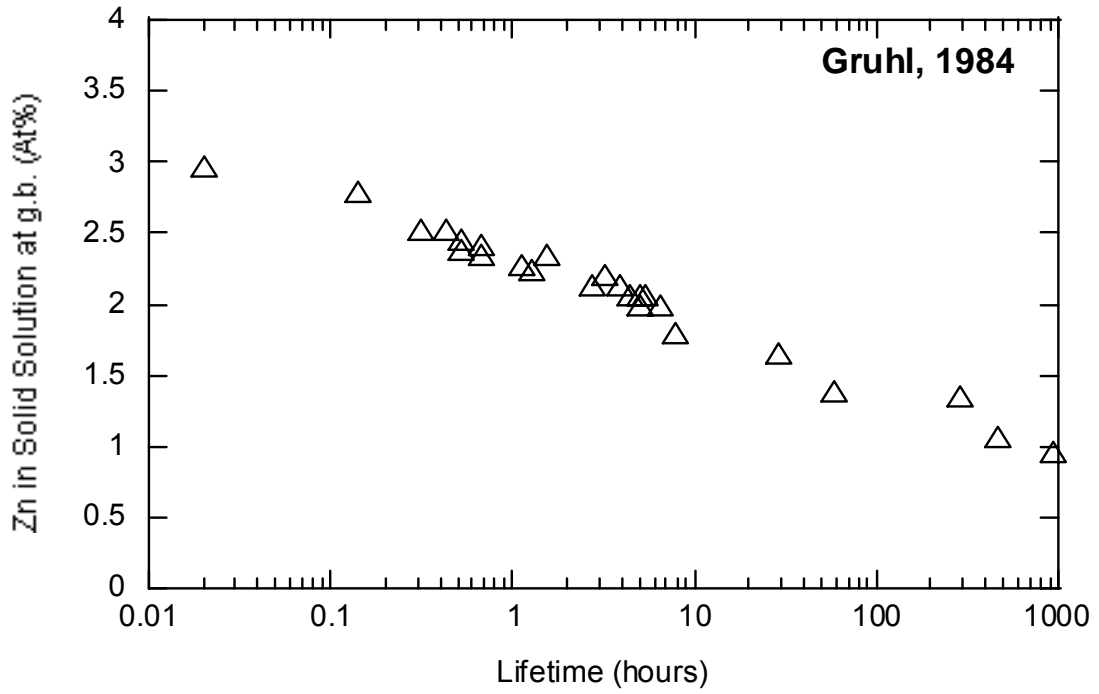
Figure 1.1 Relationship between the Zn content of the grain boundary area and time to fracture of AlZnMg (Cu) alloys, $\sigma = 250$ MPa. (Gruhl, 1984) [20]
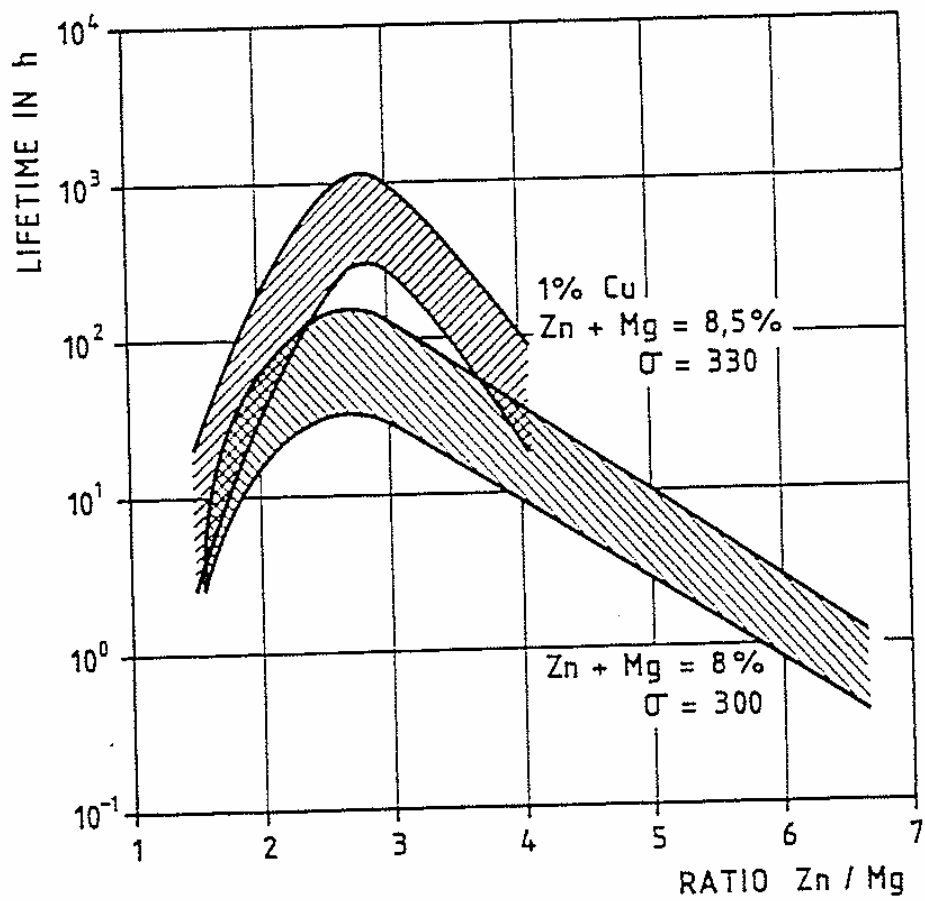
Figure 1.2 Influence on Zn:Mg ratio on SCC susceptibility of Al-Zn-Mg and Al-Zn-Mg-Cu alloys; stress = 300 MPa, heat treatment = 480°C (896°F) SHT/WQ/120 hours at 90°C (194°F). (W. Gruhl, 1978)[19]
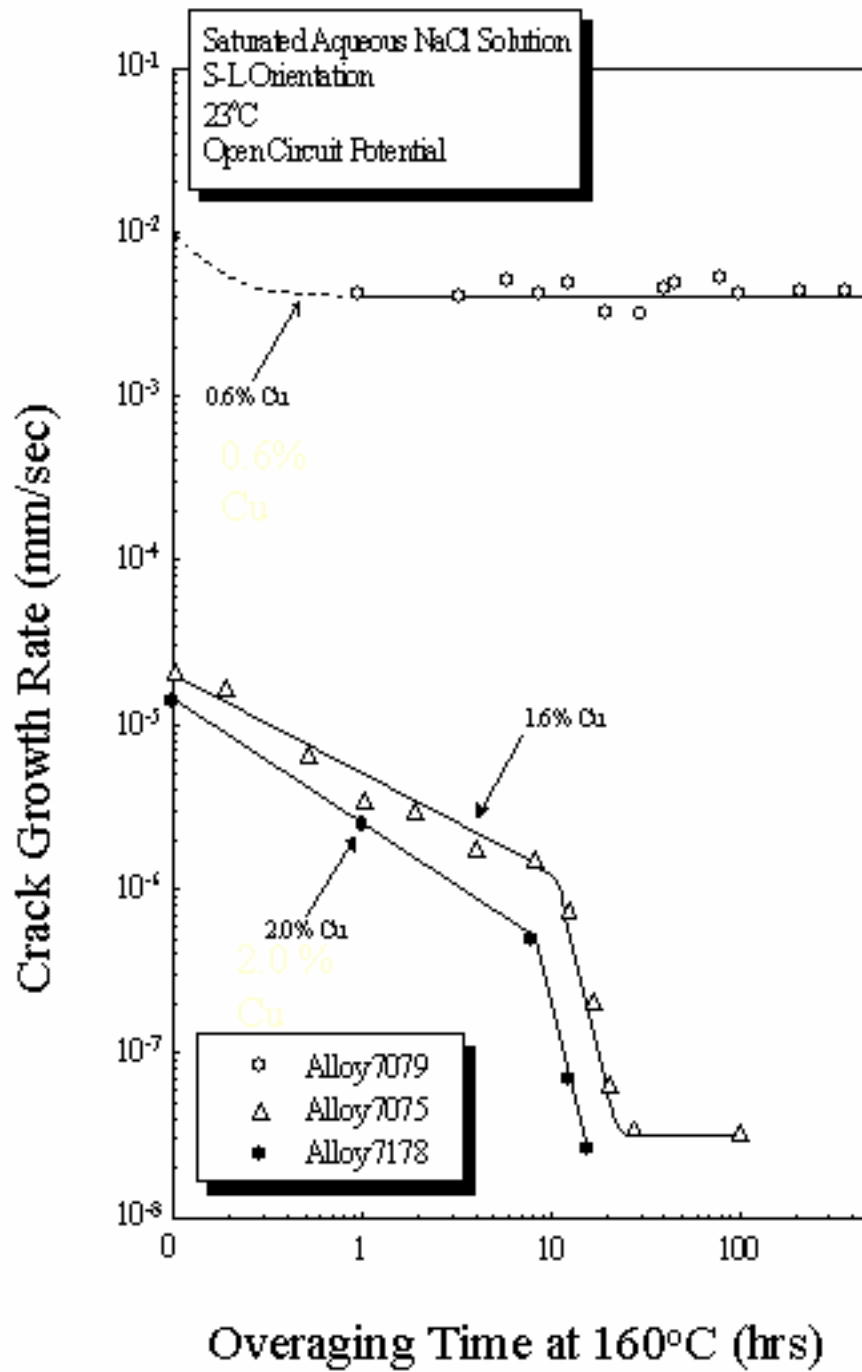
Figure 1.3 Crack growth rates for 7xxx alloys with varying Cu contents as a function of over-aging time. (Speidel and Hyatt, 1972)[22]
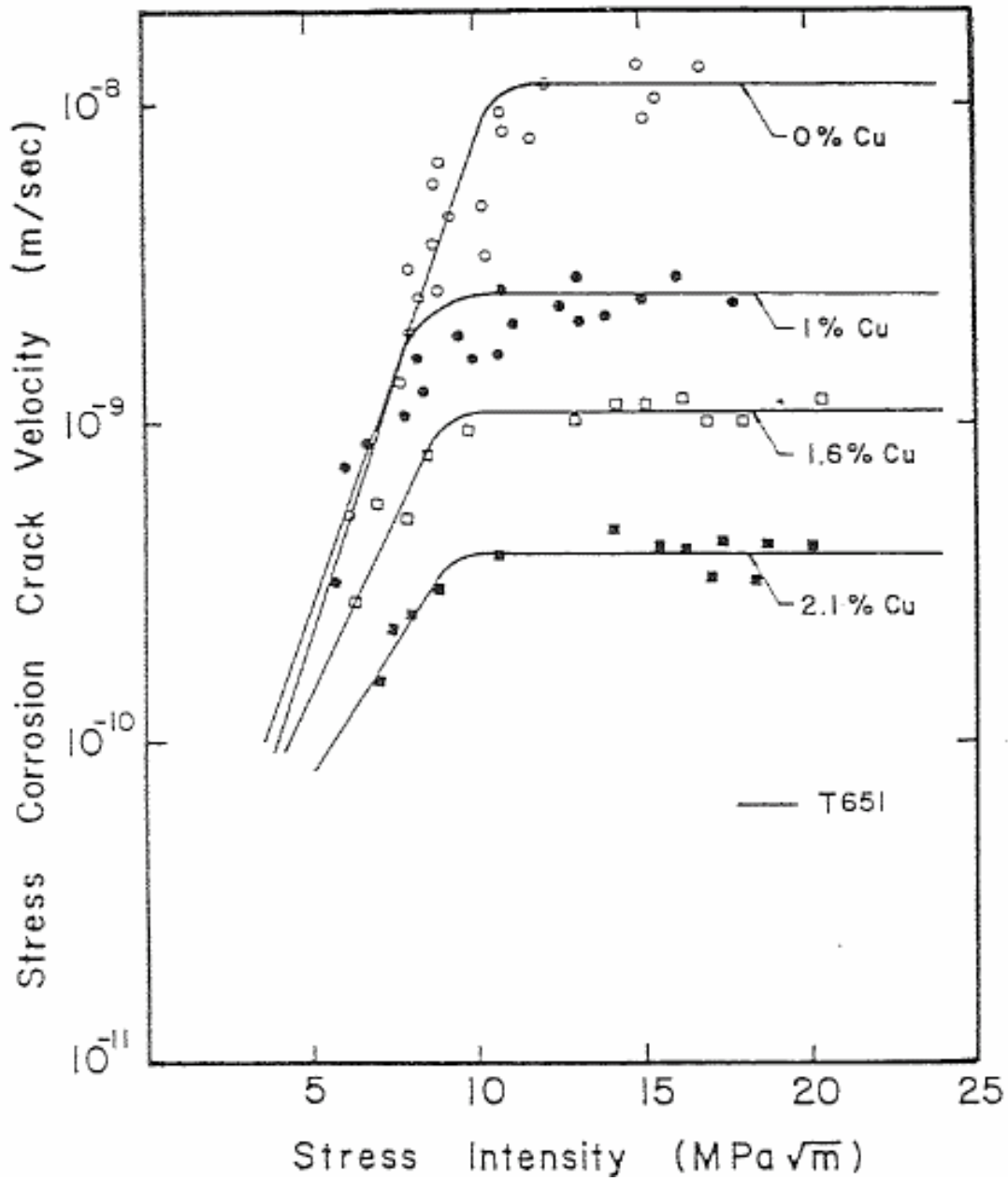
Figure 1.4a Effect of stress intensity on stress corrosion crack velocity of Al-6Zn-2Mg-XCu in 3.5% NaCl for varying copper contents. (Sarkar, Marek and Starke, 1981)[9]
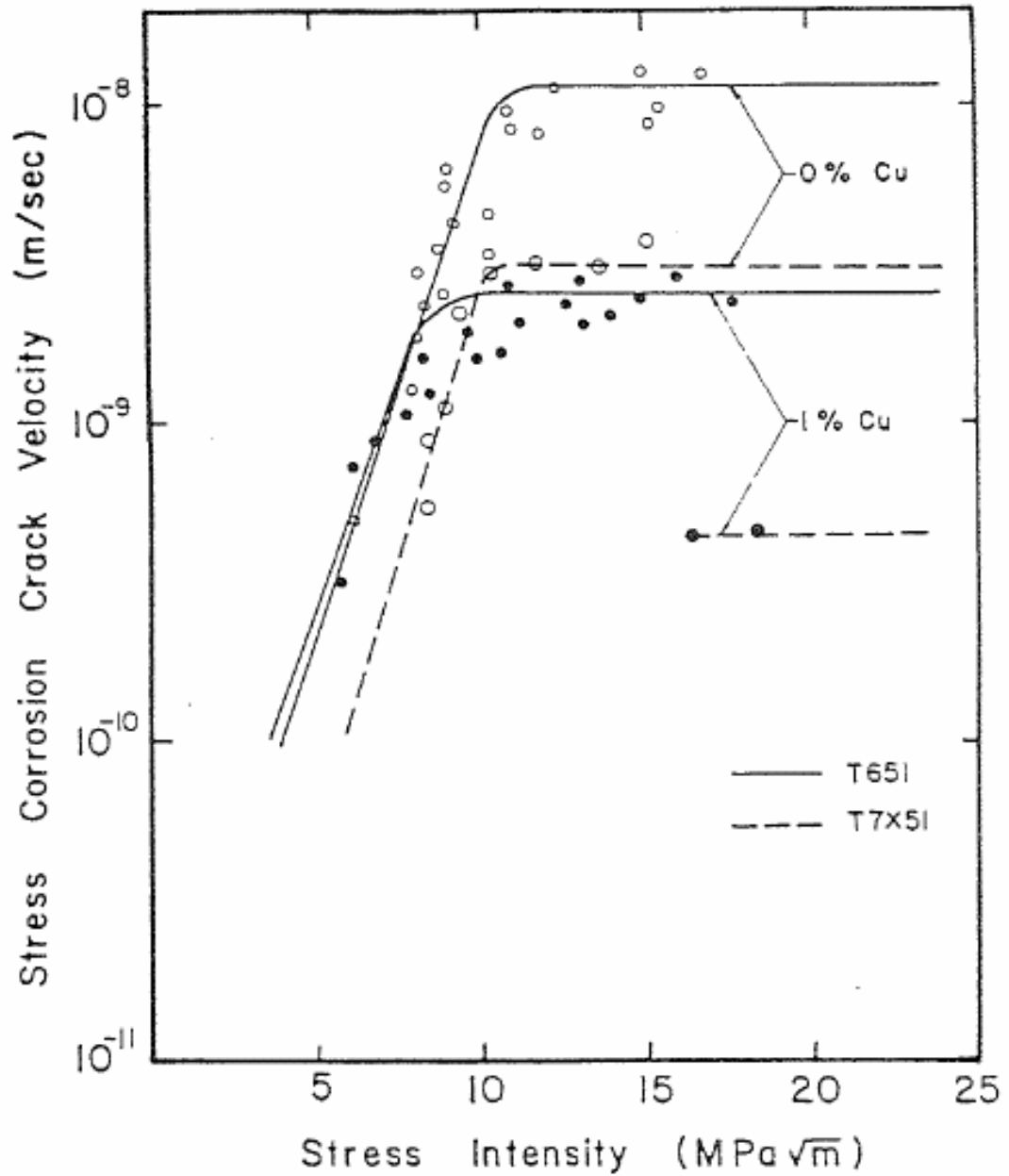
Figure 1.4b Effect of stress intensity on stress corrosion crack velocity of Al-6Zn-2Mg-XCu in 3.5% NaCl for -T651 and -T7x51 type aging treatments. (Sarkar, Marek and Starke, 1981)[9]

1.1.1.2   Microstructure

As the Al-Zn-Mg alloys are thermally treated from under-aged through peak strength to the over-aged condition, the generally accepted precipitation sequence is as follows:[33,34]

$$\alpha_{ssss} \rightarrow \alpha'' + G.P.\ (coherent) \rightarrow \alpha' + \eta'\ (semi\text{-}coherent) \rightarrow \alpha + \eta\ (incoherent)\ \ [1.1]$$
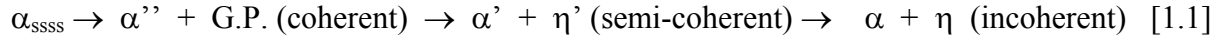
Under certain conditions of composition and temperature, an alternative precipitation sequence is possible:

$$\alpha_{ssss} \rightarrow \alpha'' + G..P.\ (coherent) \rightarrow \alpha' + T'\ (semi\text{-}coherent) \rightarrow \alpha + T\ (incoherent)\ [1.2]$$
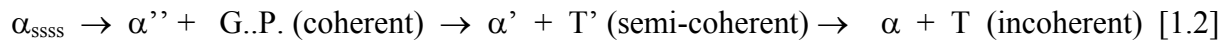
Table 1.1 summarizes pertinent information regarding these precipitates.

In the quaternary system of Al-Zn-Mg-Cu the three phases from the Al-Mg-Zn ternary system are isomorphous and completely miscible with three phases from the Al-Cu-Mg system. In alloys with 5-8%Zn and 2-3%Mg, which is generally the composition range of commercial interest, the main precipitates are the $MgZn_2$-CuMgAl and/or the $CuMg_4Al_6$-$Al_2Mg_3Zn_3$ phases. At temperatures of 260°F (127°C) to 315°F (157°C) the precipitation sequence is reported to be the same as the ternary alloys:[34]   However, in the quaternary system, the GP zones, the η'-metastable phase and the η- equilibrium phase, all contain some copper.[34-36]   The composition of the η-phases in the quaternary system can vary widely, but increases in aging temperature tend to increase the Cu and Al content of the precipitates.[37, 38] Bigot et al.[37] have reported results for AA 7050 that indicate that the precipitates in materials aged at 120˚C (248˚F) contain ~2 at% Cu while those aged at 160˚C contained ~8 at% Cu. At both aging temperatures the particles had Zn/Mg atomic ratios of ~1.

Aging of Al-Zn-Mg alloys at temperatures from room temperature to approximately 127°C (260°F) results in the formation of spherical GP zones. The addition of Cu increases the temperature range for GP zone stability. At peak strength, T6 tempers, the size of the GP zones is typically 20-35 angstroms. Very small amounts of the metastable η'-phase, which is coherent on the $(111)_{Al}$ planes, can also generally be detected in the peak aged condition. The strength in these alloys is very sensitive to GP zone size and the η'-phase is considerably less effective for

11

strengthening. The metastable η'-phase and the equilibrium η-phase are frequently present on the grain boundaries immediately after quenching, particularly in thick section products where it is difficult to achieve fast quench rates.[39]

Isothermal treatments for maximizing strength generally consist of 24-30 hours at 120-135°C (248-275°F). Optimal strengthening in these isothermal treatments is attributed to maximizing nucleation and precipitation of GP zones. Subsequent aging for longer aging times and/or at higher temperatures leads to strength losses due to over-aging. For isothermally aged Al-Zn-Mg alloys there is generally an inverse relationship between strength and EIC resistance as illustrated in Figure1.5 where both are plotted qualitatively as a function of isothermal aging time.[22]

Isothermal aging at higher temperatures, 160-170°C (320-338°F), is known to result in substantial improvements in SCC performance but maximum attainable tensile strength properties are significantly lower. The lower maximum achievable strength is attributed to the direct precipitation of a less numerous distribution η' precipitates instead of either GP zones alone and/or GP zones followed by η' precipitation at or on a more numerous distribution of GP zones.

Additionally, over-aging in the lower temperature range of 120-135°C (248-275°F) for extended times to achieve the same tensile properties as the higher temperature treatment, does not result in the same degree of SCC improvement. This is illustrated by the tensile property and SCC data for AA7050 in Table 1.2. The aging times for the T6F and the T74F thermal treatments at 250°F yield similar tensile properties and electrical conductivities to the T6 and T74 aging treatments at 325˚F but the SCC performance is inferior. The combination of tensile yield strength properties and electrical conductivity of 7xxx alloys aged at ~300-350˚F has been widely used to predict acceptable SCC performance based on the criteria in Figure 1.6 but this method is not valid for the low temperature aging treatments. The electrical conductivity is most strongly affected by solute atoms. Changes in conductivity at standard aging temperature are therefore indicators of the amount of solute that has been precipitated out of solid solution. The relative impact of the various solute atoms varies and inconsistencies in conductivity due to temperature of aging are likely related to different rates of diffusion and precipitation at those temperatures.

Luetjering and Gysler[40] provided a detailed description of the strengthening processes in 7xxx alloys. In the under-aged condition, coherent particles (GP zones) are precipitated and strengthening occurs because the particles must be sheared for motion of dislocations past the particles. As the coherent particles increase in size, shearing becomes more difficult and the yield stress increases. The shearing mechanism leads to an inhomogeneous distribution of plastic strain in slip bands. The high stress concentration at the intersection of the slip band with the grain boundaries causes crack nucleation by shearing off and fracturing the grain boundaries. The cracks then propagate along grain boundaries or along slip bands. Beyond a critical size the particles are no longer shearable and the particles must be by-passed. At some point during the over aging the particles coarsen at the expense of smaller particles and the inter-particle spacing increases resulting in a decrease in the yield strength. Luetjering and Gysler also indicated that reducing grain size improves tensile ductility by limiting slip length (pile up length) for the shearing mechanism and reducing stress concentrations.[40]

In 1969, Speidel[6] investigated the influence of the microstructure on susceptibility to intergranular stress corrosion cracking of AA7075. He found that aging conditions that had low resistance to SCC had long straight narrow slip bands and pile-ups at grain boundaries after deformation while aging conditions (both severely underaged and overaged) that had high resistance to SCC exhibited more homogeneous slip after deformation. These observations imply that the important factors in determining SCC susceptibility are related to matrix particle-dislocation interactions and the slip mechanism during plastic deformation. However, the aging conditions Speidel chose to produce susceptible materials consisted of low temperatures for short times while those with high SCC resistance were aged at higher temperatures for relatively long times. These aging conditions would be expected to produce considerable differences in precipitate size and distribution that would represent relatively extreme differences in slip character.

In the 1981 study by Sarkar, Marek and Starke[9], SEM obtained from a surface replica of a stress corrosion fracture surface indicated the presence of parallel slip steps on the intergranular facets for a 0% Cu version of alloy 7050 in the T651 condition. These steps imply that dislocation movement on preferred planes, which intersect the grain boundary, produced dislocation pile-ups and created stress concentrations at the grain boundary. Fracture surfaces of more slowly cracking conditions were too corroded to allow detailed examination. TEM

characterization of thin foils prepared from specimens deformed to 1% plastic strain showed inhomogeneous planar deformation in the 0 and 1% Cu alloys in the T651 condition and homogeneous looping in the higher Cu alloys. In the T7x51 condition all of the alloys showed homogeneous deformation. This is consistent with Gruhl's observation that coarse grain materials, which show very marked slip band formation from minimal plastic deformation, are extremely susceptible to SCC.[11]

Another study by Carter et al.[10] also showed different slip character for under-aged (UA) and over-aged (OA) 7475 in TEM images (Figure 1.7). Aging treatments for the UA and OA tempers were chosen such that they had the same hardness (so presumably similar yield strengths). Strain localization in planar deformation bands was observed in UA temper while th OA temper promoted homogeneous deformation. UA temper produces coherent precipitates that are sheared by dislocations resulting in planar slip. Over-aging produces incoherent precipitates that are looped or by-passed by dislocations resulting in wavy slip. Figure 1.8 shows aging curves at 120°C and 160°C that indicate that UA, 6h @120°C is approaching max hardness for GP zones. A second reaction is indicated at aging times of ~12-24h with peak hardness at 20 hours. The OA temper, 17 hours at 160°C, is significantly passed the peak hardness for that aging temperature at 6 hours @ 160°C.

Lin and Starke[7] also attributed the environmental sensitivity of low copper 7xxx type alloys to the fact that localized slip bands intensify the metal-environment interactions. They demonstrated that although strain localization and planar slip improve fatigue crack growth resistance in an inert environment (vacuum) by enhancing slip reversibility, most of this advantage disappears when testing is conducted in laboratory air due to increased environmental sensitivity with strain localization.

From 1979 through 1983 Albrecht, Bernstein, Hardwick and Thompson[12-14] conducted a series of studies on underaged, peak aged (T6) and overaged (T73) AA7075 and AA7050. They used cathodic charging and concurrent plastic straining (Straining Electrode Technique =SET) to evaluate hydrogen embrittlement of these materials. The marked embrittlement of the underaged condition was attributed to "a microstructure which allows for planar dislocation arrays and long slip lengths."

Table 1.1 Probable Precipitation Processes in Al-Zn-Mg [33-35]

Phase	Composition	Structure	Lattice Parameter (nm)	Remarks
G.P. zones	Zn- rich	Spheres		Coherent; Possibly two types
η' (or M')	$MgZn_2$	hexagonal	a = 0.50 c = 0.87	Semi-coherent; May form from GP zones in alloys with Zn:Mg >3:1; Orientation relationship with matrix $(0001)_\eta$ // $(110)_\alpha$; $[11\text{-}20]_\eta$ // $[112]_\alpha$
η (or M)	$MgZn_2$	Hexagonal $P6_3$/mmc 12 atoms /unit cell	a = 0.52 c = 0.85	Incoherent; Forms at or from η', 9 possible orientation relationships with matrix most common are: $(10\text{-}10)_\eta$ // $(001)_\alpha$; $(0001)_\eta$ // $(110)_\alpha$ and $(0001)_\eta$ // $(1\text{-}1\text{-}1)_\alpha$; $(10\text{-}10)_\eta$ // $(110)_\alpha$
T'	$Al_2Mg_3Zn_3$ or $Mg_{32}(Al,Zn)_{49}$	hexagonal	a = 1.39 c = 2.75	Semi-coherent; May form instead of η in alloys with low Zn:Mg ratios; $(0001)_T$ // $(111)_\alpha$; $(10\text{-}11)_T$ // $(11\text{-}2)_\alpha$
T	$Al_2Mg_3Zn_3$ or $Mg_{32}(Al,Zn)_{49}$	Cubic Im3 162 atoms/ unit cell	a = 1.42	Incoherent; May form from η if aging temperature > 190°C; or from T" in alloys with low Zn:Mg ratios; $(100)_T$ // $(112)_\alpha$; $[001]_\eta$ // $[100]_\alpha$

Table 1.2 Tensile Properties, SCC Performance and Electrical Conductivity of AA7050.[39]

Temper	Aging	Longitudinal Properties		Short Transverse Properties		SCC Test Results ASTM G44 @ 25 ksi		Electrical Cond. (%IACS)
		TYS (ksi)	UTS (ksi)	YTS (ksi)	UTS (ksi)	#Fail/ #Tested	Days	
T6 @ 325F	6hr/325F	76.4	80.2	75.1	82.6	3/3	23,33,40	37.5
T74@ 325F	27hr/325F	64.8	73.7	62.5	73.8	0/3	(>90)	41.5
T6F @ 250F	750hr/250F	75.5	80.1	74.5	83.4	3/3	2,2,2	36.3
T74F @ 250F	2000hr/250F	67.7	76.0	72.6	82.1	3/3	2,13,19	40.6
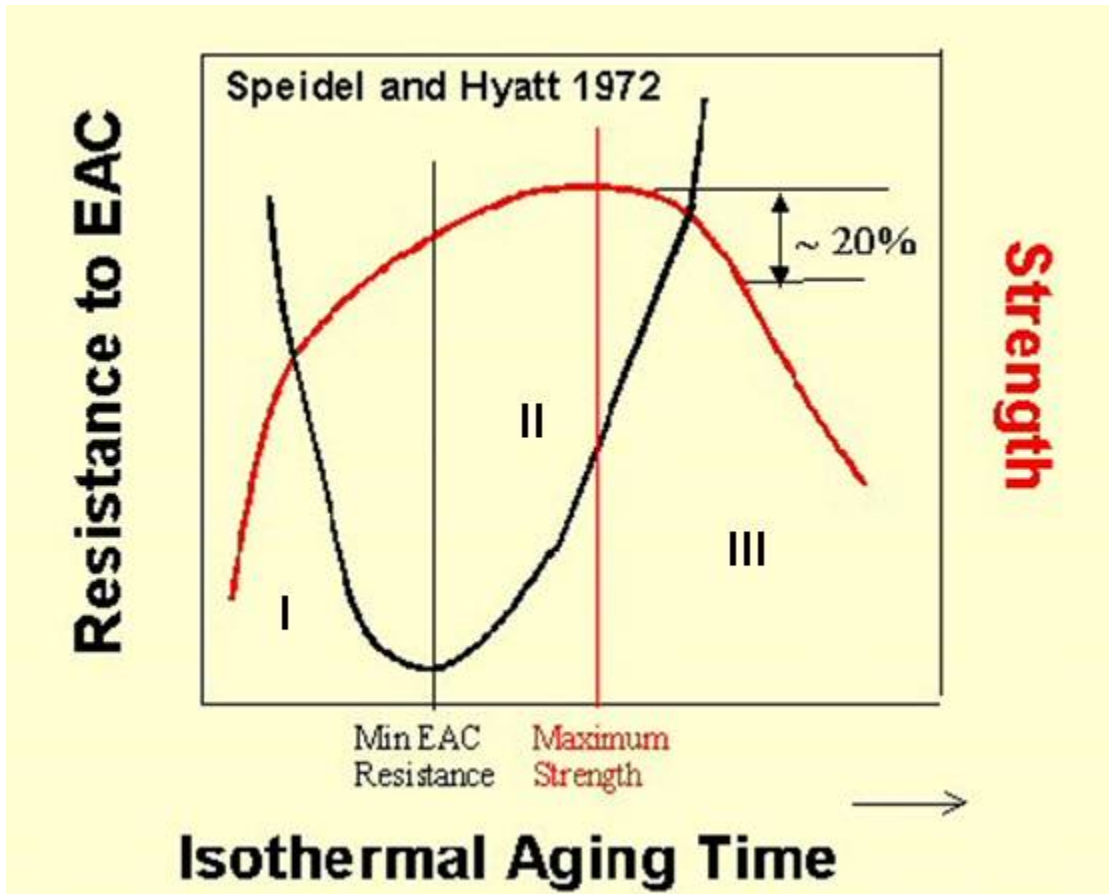
Figure 1.5 Effect of isothermal aging on strength and EAC resistance (Speidel and Hyatt).[22]
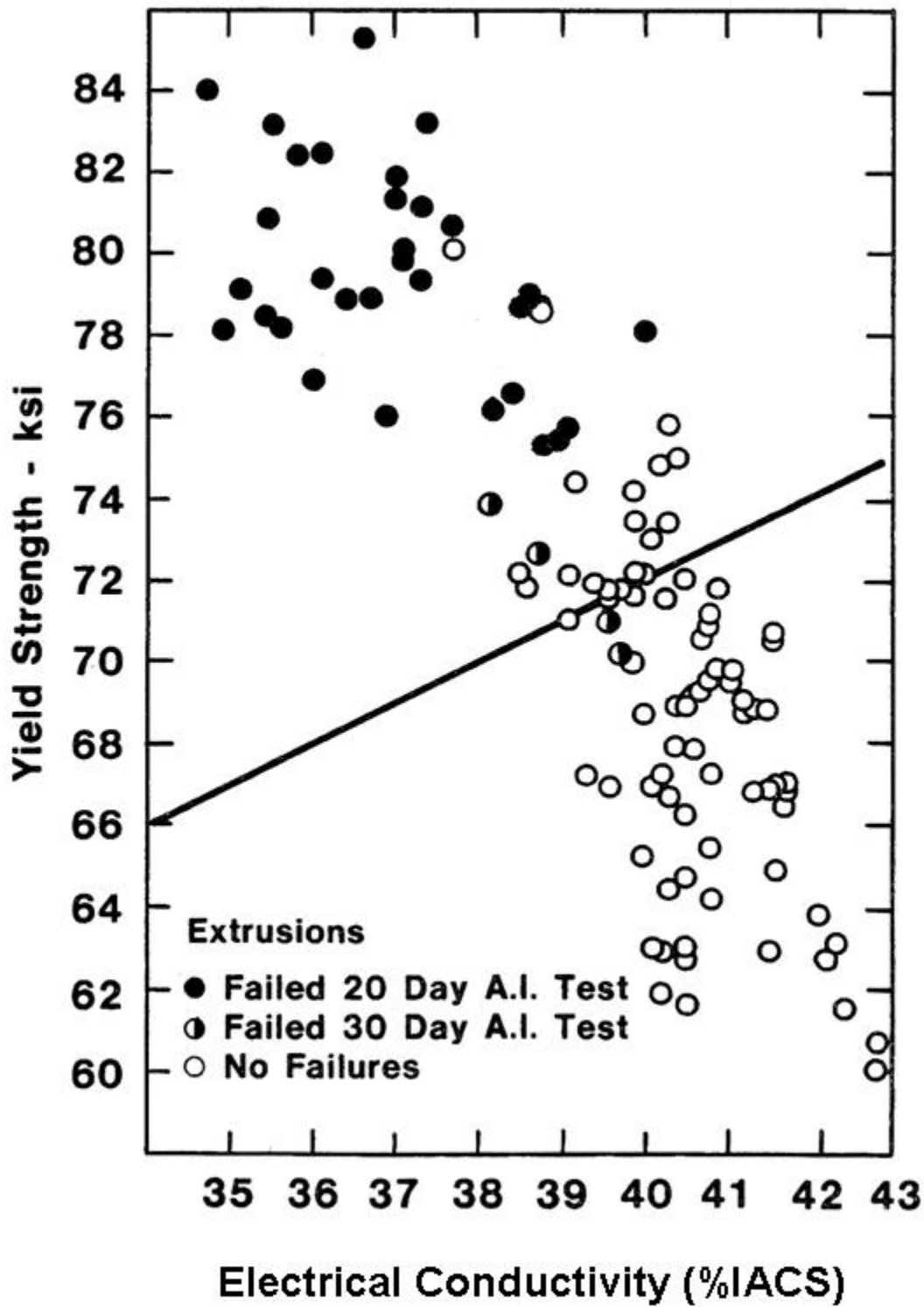
Figure 1.6 Correlation of SCC resistance with strength and electrical conductivity used as a screening tool for SCC resistance of 7xxx alloys aged at 325°F (163°C).[39]

a.   b.
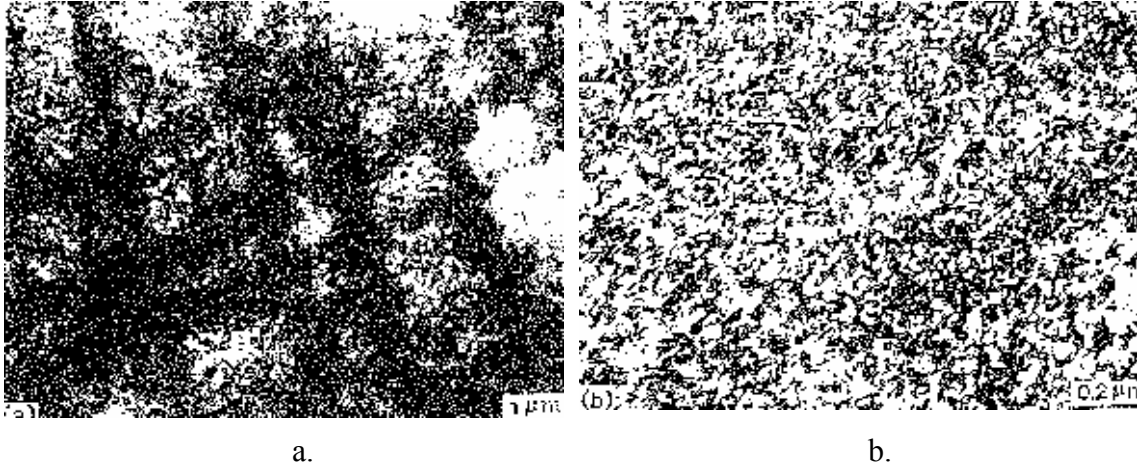
Figure 1.7 TEM image showing different slip character for AA7475 in a. under-aged and b. over-aged conditions. (Carter et al)[10]
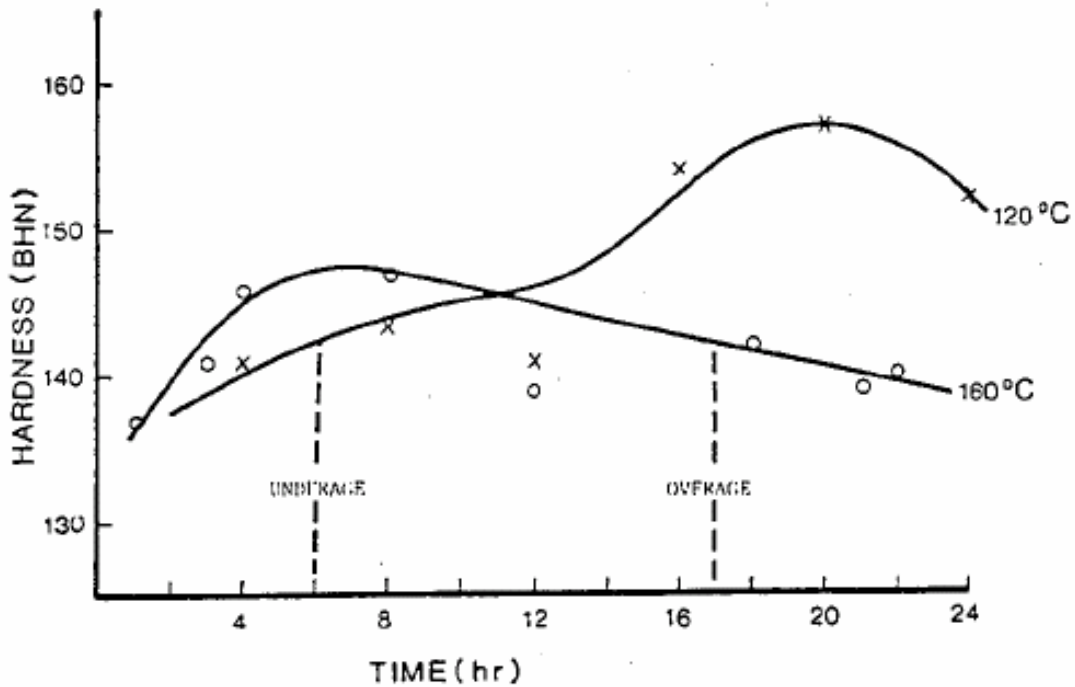
Figure 1.8 Aging curves for AA7475 at 120°C and 160°C indicating times and temperatures used by Carter et al. for the under-aged and over-aged conditions. [10]

1.1.1.3 Mechanical Aspects

SCC failures often initiate at stress raisers or flaws (e.g. notches, bolt holes, fatigue cracks, etc.). The magnitude of the stress field surrounding a stress raiser, the stress intensity factor (K), is a function of the applied stress (σ), the flaw size (a) and other geometric considerations that depend on the configuration and the manner the stress is applied. Fatigue pre-cracked specimens such as double cantilever beam (DCB) specimens used to measure stress corrosion crack propagation rates, are designed to maintain plane strain loading conditions. The crack velocity (v) vs. stress intensity (K) curve (v-K curve) provides a quantitative measure of the resistance to SCC of an alloy under stress in the presence of a flaw. The v-K curve generally exhibits three regions (referred to as Stages I, II and III) as illustrated in Figure 1.9. At relatively low stress intensities (Stage I) the velocity of cracking increases rapidly as stress intensity increases. At the lower end of Region I there may or may not be a stress intensity threshold (K_{ISCC}) i.e. stress intensity below which, no SCC will occur. At intermediate stress intensities, Stage II, the crack velocity is independent of stress intensity. The constant velocity attained in Stage II is also referred to as the plateau velocity. At relatively high stress intensities, some materials exhibit another region of stress dependent cracking, Stage III.[22]

A stress raiser such as an existing crack creates a localized region of biaxial or triaxial stress near the tip of the crack. The stress concentration at the tip of a fine crack can produce high localized stresses that exceed the yield strength of the metal in the region surrounding the crack tip. This region is therefore referred to as the plastic zone. The size of the plastic zone depends on the applied stress intensity and the yield strength of the material. Under plane strain conditions the size or radius is estimated by the following equation :

$$r_y \approx (1/6\pi)(K^2/\sigma_{ys}^2) \quad [1.3]$$

The high triaxial stresses in this plastic zone ahead of the crack tip provide potential sites for accumulation of hydrogen that enters the metal by diffusion from the surface. Troiano[41] first noted that hydrogen would be attracted to the triaxial stress region because of the dilational field. Imposition of a stress creates a chemical potential gradient driving hydrogen to the triaxial stress region and diffusion occurs according to the Einstein drift equation:

$$J = -(Dc/kT)(\delta\mu/\delta R) \quad [1.4]$$

19

High hydrogen fugacities on the order of 10^{40} atmospheres are possible in the triaxial stress region.[1]

Significant environmental effects are also observed under cyclic loading conditions for 7xxx aluminum alloys. It therefore seems likely that at least some aspects of the fracture mechanism for corrosion fatigue and stress corrosion cracking are related. Magnin et al.[42] made some interesting observations comparing stress corrosion cracking (SCC), which occurs under sustained tensile loads and/or at slow strain rates and corrosion fatigue (CF) which occurs under cyclic or dynamic loading conditions. At the free corrosion potential, corrosion fatigue occurs at all strain rates from 1E-8 to 1E-2 s^{-1} unlike SCC, which only occurs at strain rates < 2E-5 s^{-1} for 7020-T4 UA and 8E-7 for 7020 OA (T6DR). At strain rates > ε(SCC) transgranular CF micro-cracks are formed by a combined effect of the plastic strain localization due to fatigue and the localization of the breakdown of the passive film. At strain rates < ε(SCC) intergranular micro-cracks can be formed by SCC, CF is enhanced by SCC. However, if a cathodic potential (-1100 mV vs. SCE) is immediately imposed upon exposure to the electrolyte, SCC does not occur because micro-crack formation requires anodic dissolution. CF occurs by H entry and embrittlement at mechanically formed micro-cracks. These observations support the necessity of a surface defect for hydrogen entry. For SCC the surface defect is created by anodic dissolution while in CF the surface defect is created by mechanical means. It was therefore proposed by Magnin et al. that anodic dissolution contributes mainly to initiation phase and hydrogen to the propagation phase.

Selines et al.[43] also measured fatigue crack growth rates of AA7075 as a function of environment, frequency, stress wave form, alloy chemistry and thermomechanical treatment. Varying the test frequency changes the total crack tip exposure time. Within each cycle, the total crack tip exposure time includes the opening time, the time at peak load and the closing time. The opening time was varied by using different stress wave forms. Although it was known that crack growth extension in inert environments occurs only during the opening portion of each cycle, it had generally been presumed that the enhanced corrosion fatigue crack propagation rates were related to exposure of the crack tip to the corrosive environment during the time at peak load. For square wave form stresses the crack growth rates measured however, were independent of the frequency such that varying the time the crack is held open at peak load does not effect the crack growth rate. Correlation of variations in the opening time with crack growth

rate indicate that the effect of the corrosive environment on the crack growth rates is a synergistic effect taking place only during the opening part of the load cycle rather than by the time spent at peak load. They considered a corrosion-plastic flow interaction model which states that during opening of a fatigue crack, adsorbed ions at the crack tip facilitate the egress of dislocations at the crack tip resulting in a net corrosion component per cycle that is proportional to the amount of fresh crack tip surface exposed. The influence of the environment on dislocation motion at the free surface was attributed to "interaction of an 'adsorbed ion' with the stress field of dislocations near a free surface." The rise time dependence of the corrosion effect was speculated to be related to the rate of formation of an oxide film.

Taheri et al.[44] evaluated strain rate dependence of hydrogen embrittlement for three conditions (under aged temper = UT, T6 and T73) after cathodically pre-charging in HCl solution (pH=1). Strain rates ranging over 4 orders of magnitude showed that all three tempers exhibited a maximum in embrittlement (based on reduction in area, RA) at intermediate strain rates. The strain rate of maximum brittleness increased with degree of aging as illustrated in Figure 1.10. The explanation provided was that at low strain rates accumulation of hydrogen atoms at trap sites is reduced by diffusional escape and at high strain rates the hydrogen atoms can neither diffuser nor be carried by dislocations. The data is consistent with the Tien et al.[45] dislocation sweep model which predicts a critical strain rate proportional to the critical velocity at which the dislocation line would be expected to break away from its hydrogen cloud so that dislocation sweeping is no longer effective. In this model the embrittlement would be proportional to the strain rate at strain rates below the critical strain rate.
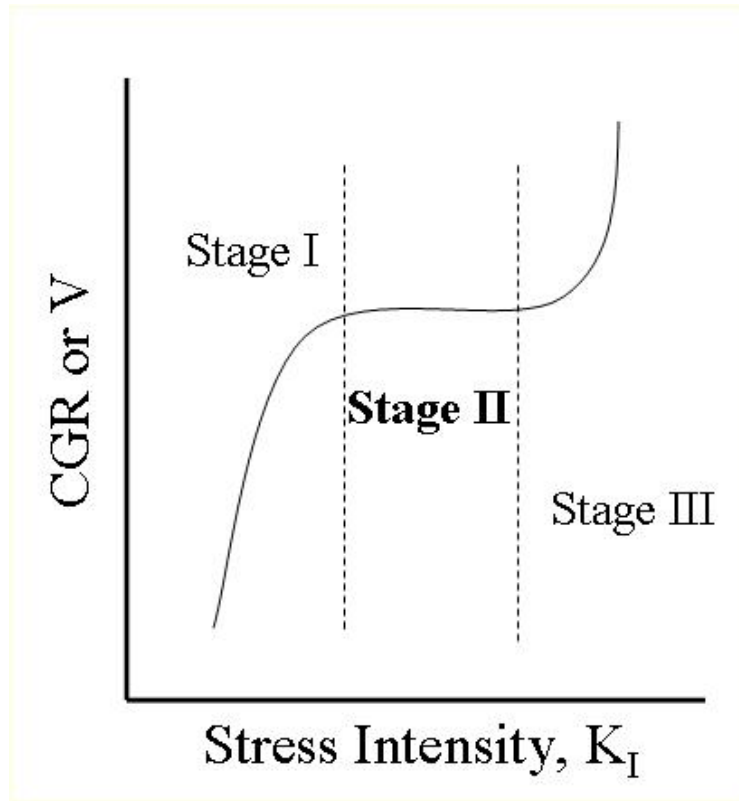
Figure 1.9 Effect of stress intensity on SCC crack growth rates a.k.a. v-K curve. In this paper the regions in the v-K curve are referred to as Stages I, II and II while Regions I, II, and III are used to refer to the regions in the plot of SCC susceptibility vs. aging time in Figure 1.5.
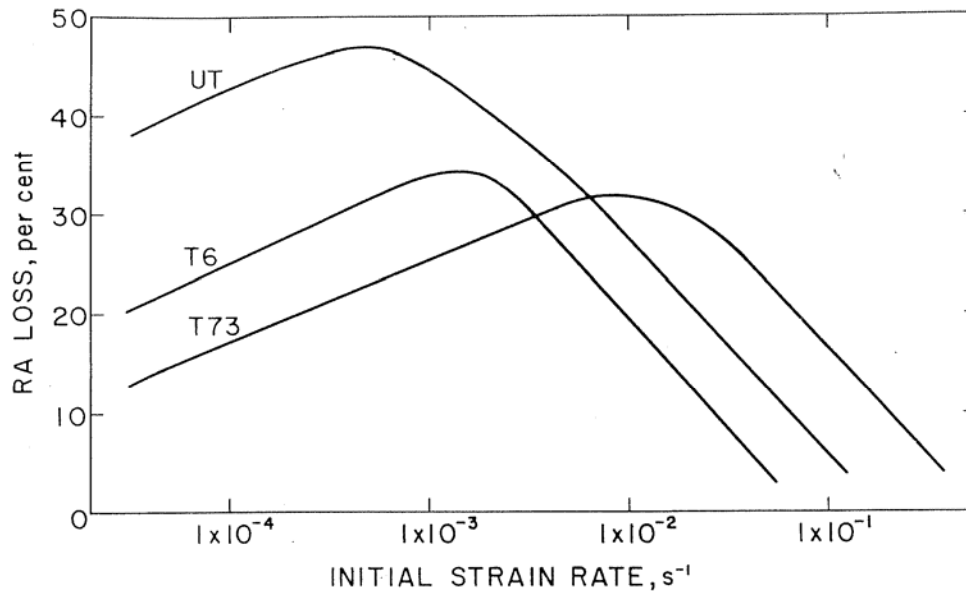
Figure 1.10 Loss of Reduction in Area (RA) in hydrogen charged specimens as a function of strain rate (Taheri et al.).[44]

1.1.1.4 Environment

The environment has a critical effect on the initiation and propagation of subcritical stress corrosion cracking in high strength aluminum alloys. Measured crack velocities for a single alloy can vary over nine orders of magnitude depending on the environment. Outdoor service relevant exposures consist of wet and dry periods. Intermittent exposures (cyclic wet/dry conditions) are more apt to cause stress corrosion failures than constant immersion conditions where other forms of corrosion such as pitting dominate. The importance of the wet dry cycles for SCC has generally been attributed to the concentrating of aggressive ions such as chloride ions. This transition from SCC susceptibility under intermittent exposure conditions to pitting in constant immersion exposures implies that a particular balance between anodic dissolution and passivity may be important to the SCC mechanism.

Neither initiation nor propagation of stress corrosion cracks is observed for susceptible tempers of 7xxx alloys in dry (<0.01%RH) air or in other dry gases such as argon, or nitrogen.[22] Addition of moisture to any of these gaseous environments results in immediate crack propagation of pre-cracked specimens. At 100% RH in each of these gases at room temperature (73°F) the plateau or Stage II crack growth rate (stress-independent crack growth rate) is ~10^{-3} in./hr. The analogous crack growth behavior in various gaseous environments indicates that the water vapor causes SCC of high strength aluminum alloys. Tests on 7075-T651 at varying levels of RH in air have shown a linear dependence of crack growth rate on the log (RH) as illustrated in Figure 1.11. In contrast, Stage I crack velocities are dependent on stress intensity but are not significantly affected by the differences in the water vapor concentration. At low stress intensities in Stage I the crack growth rate increases with increases in the applied stress intensity until the crack growth reaches a rate that is reaction limited and crack growth rate remains relatively constant with further increases in stress intensity. The dependence of the plateau crack growth rate on water vapor content implies that the transition from Stage I (stress-dependent) to Stage II (stress independent) crack growth is due to a reaction or process kinetic limitation related to the available water vapor.[22]

Cracking observed in high humidity environments is presumably due to the reaction of aluminum with water to form high fugacity hydrogen gas through the overall reaction:

$$2Al + (3+X) H_2O (g) \rightarrow Al_2O_3 \cdot (X)H_2O (s) + 3H_2 (g) \quad [1.5]$$
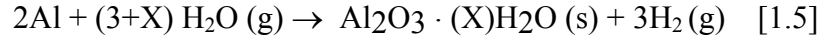
Although the overall reaction indicates production of hydrogen gas, the reaction actually occurs in multiple steps.[46] The first step is generally an electronation reaction. The reduction of water at the oxide metal interface produces atomic hydrogen, which can either be absorbed into the metal or recombine to form H_2 gas.

$$H_2O + M(e^-) \rightarrow (OH^-) + MH(ads) \quad [1.6]$$

In neutral to acidic aqueous solutions the electronation reaction can occur by proton discharge, i.e. reduction of hydrated protons:
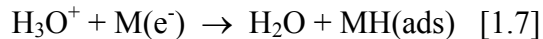
$$H_3O^+ + M(e^-) \rightarrow H_2O + MH(ads) \quad [1.7]$$

The recombination of adsorbed hydrogen, can occur by two possible types of paths. It can occur without charge transfer by chemical desorption (a.k.a. catalytic recombination) or by means of an electrodic desorption step such as:

Chemical Desorption: $2MH(ads) \rightarrow 2M + H_2 (g)$ [1.8]

Electrodic Desorption: $MH + H_3O^+ + M(e^-) \rightarrow 2M + H_2O + H_2 (g)$ [1.9]
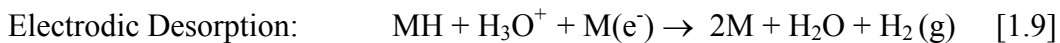
If the actual reaction path on a particular metal electrode involves a fast electronation reaction step followed by a slow (rate-determining) desorption step, adsorbed hydrogen atoms will accumulate on the metal surface and a high surface coverage of adsorbed hydrogen atoms will exist at steady state conditions. On the other hand, if proton discharge is slow, then the formation of adsorbed hydrogen is difficult and the hydrogen atoms that do arrive on the surface rapidly form hydrogen gas so the surface coverage remains low.

The heat of absorption associated with the gas phase adsorption of atomic hydrogen is approximately equal to the strength of the metal-hydrogen bond.[46] For the transition metals the bond strength is related to the d-band character of the metal. As the d-band character increases, the current density at cathodic overpotentials decreases, M-H bond strength increases, the hydrogen adsorption energy decreases, and coverage with hydrogen atoms increases. For metals with sp valence orbitals (no d electrons) the current density at cathodic overpotentials increases as M-H bond strength increases.

The exchange current density for the hydrogen-evolution reaction provides a relative measure of the reaction rate on a metal electrode.[46,47] Noble metals such as platinum and palladium are efficient catalysts for the hydrogen evolution reaction with exchange current densities of approximately 1mA/cm^2 while other metals that are poor catalysts for hydrogen evolution such as mercury and lead have exchange current densities on the order of 10^{-12} A/cm^2. Aluminum is a relatively poor catalyst for the hydrogen evolution reaction with an exchange current density on the order of 10^{-9} A/cm^2. For 7xxx series alloys the electronic nature of the various alloying elements in solid solution may significantly influence the exchange current density for the hydrogen evolution reaction. Zinc is a poorer catalyst than aluminum with an exchange current density on the order of 10^{-10} A/cm^2, which is consistent with the lack of unpaired d band electrons in zinc. Copper on the other hand is a relatively good catalyst for the hydrogen evolution reaction with an exchange current density on the order of 10^{-6} A/cm^2. Therefore zinc in solid solution could enhance the adsorption of hydrogen while copper in solid solution could significantly reduce the hydrogen absorption of the alloys.

Accurate determination of the actual reaction path can generally be accomplished by a combination of the evaluation of the dependence of hydrogen coverage,θ, on the electrochemical overpotential, η, and evaluations of the transfer coefficient (Tafel slope α), reaction order and reaction stoichiometry. Evaluation of these parameters on copper electrodes indicates a rate determining proton discharge mechanism with low coverage of the metal surface with hydrogen.[48] This reactivity of copper implies that one possible contribution of copper for SCC resistance of 7xxx alloys may be to reduce the adsorption of hydrogen i.e. to catalyze recombination/hydrogen evolution.

Adsorbed hydrogen can either recombine to form hydrogen gas or diffuse into the metal. High surface coverage on metals for which the desorption step is slow favors hydrogen uptake in the metal because of the longer residence times. Numerous investigations have evaluated the diffusion of hydrogen in aluminum but with little agreement on the diffusivity and activation energy values.[49-53]

Increases in temperature decrease the time to failure in SCC tests using smooth tensile bars. Quantitative measurements of crack growth rates in pre-cracked specimens as a function of stress intensity and temperature have shown that increasing the temperature generally increases the Stage II crack growth rate and sometimes shifts Stage I to lower stress intensities, i.e.

decreases K_{ISCC} as illustrated for AA7079-T651 and AA7039-T651in Figure1.12. In fact, if the logarithm of the crack growth rate (log da/dt) is plotted versus reciprocal temperature a linear relationship has been observed indicating that SCC is a thermally activated process with characteristic Arrhenius behavior as illustrated in Figure 1.13. Therefore, Stage II crack velocity is apparently related to temperature by the following general equation:

$$V_{II} = V_0 \exp(-Q/RT) \qquad [1.10]$$

where V_{II} is the Stage II crack velocity (da/dt), V_0 is a pre-exponential experimental constant, R is the gas constant (8.314 J/mol °K), T is the temperature (°K), and Q is the apparent activation energy for crack growth.[22]

In Stage I, the crack velocity is dependent on both stress intensity and temperature as follows:

$$V_I = V_0 \exp[-Q + bK)/RT] \qquad [1.11]$$

where V_I is the Stage I crack velocity (da/dt), K is the stress intensity, and b is an experimentally determined constant that is related to the crack tip geometry.

$$b = 2U/(\pi\rho)^{1/2} \qquad [1.12]$$

U is the activation volume and ρ is the radius of the crack tip curvature.[22] These relationships imply that the stress dependence of the crack velocity should decrease as the radius of the crack tip curvature increases. Therefore, enhanced plastic relaxation of the crack tip as yield strength decreases should result in reduced stress dependence of crack velocity. For 7xxx alloys this reduced stress dependence has been observed as a function of over-aging time where decreases in yield strength correspond with decreasing slopes in Stage I of the v-K curve.[22]
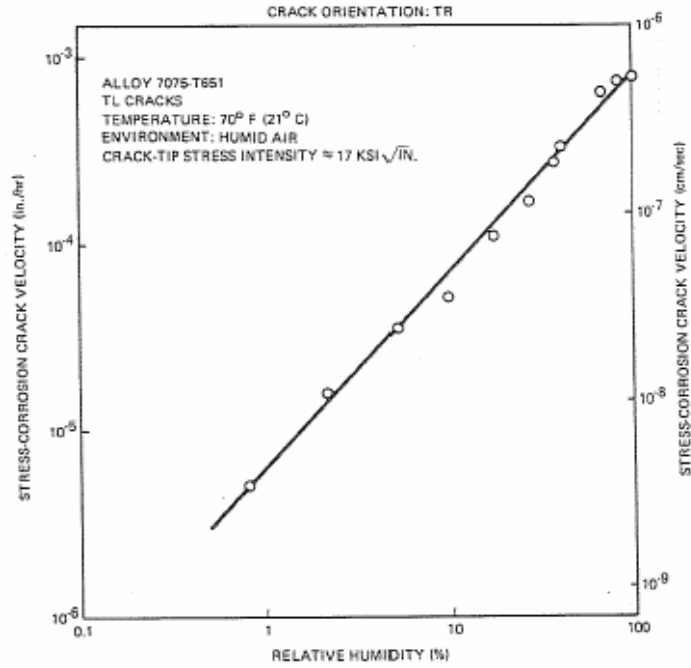
Figure 1.11 Effect of humidity of air on stress independent crack velocity of a high strength aluminum alloy (Speidel and Hyatt).[22]
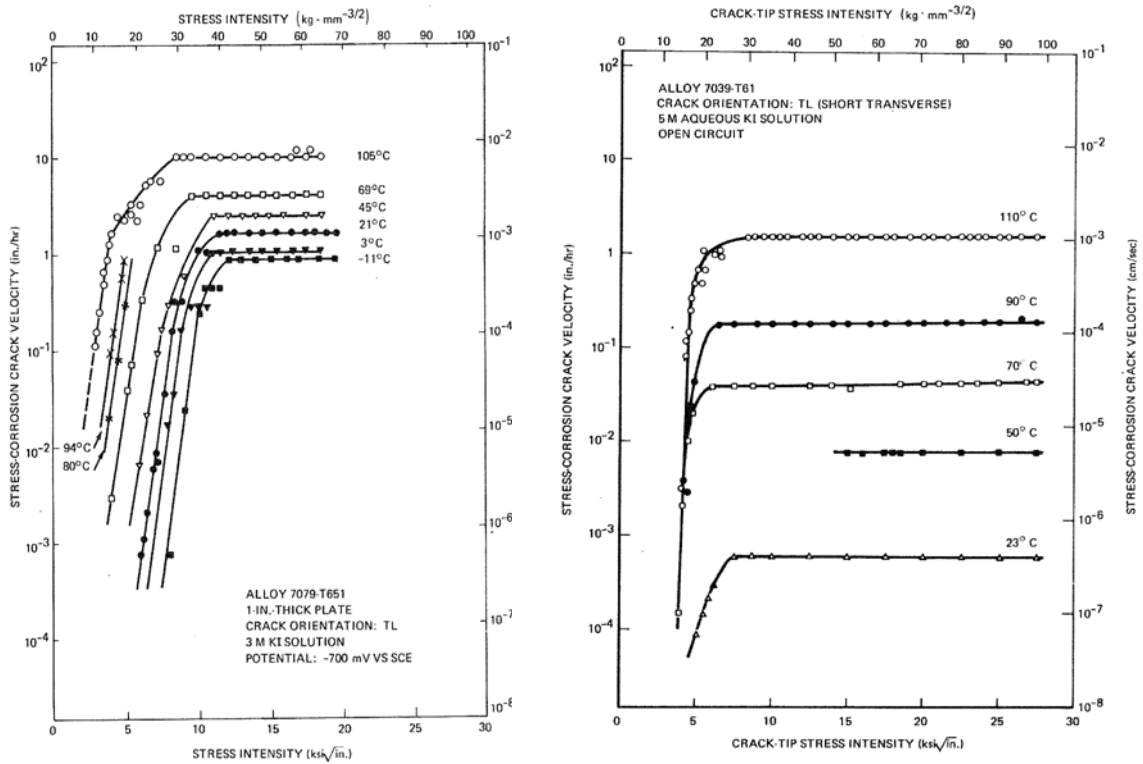
Figure 1.12. Effect of temperature and stress intensity on crack growth rates for a. 7079-T651 and b. 7039-T651. (Speidel and Hyatt)[22]

27
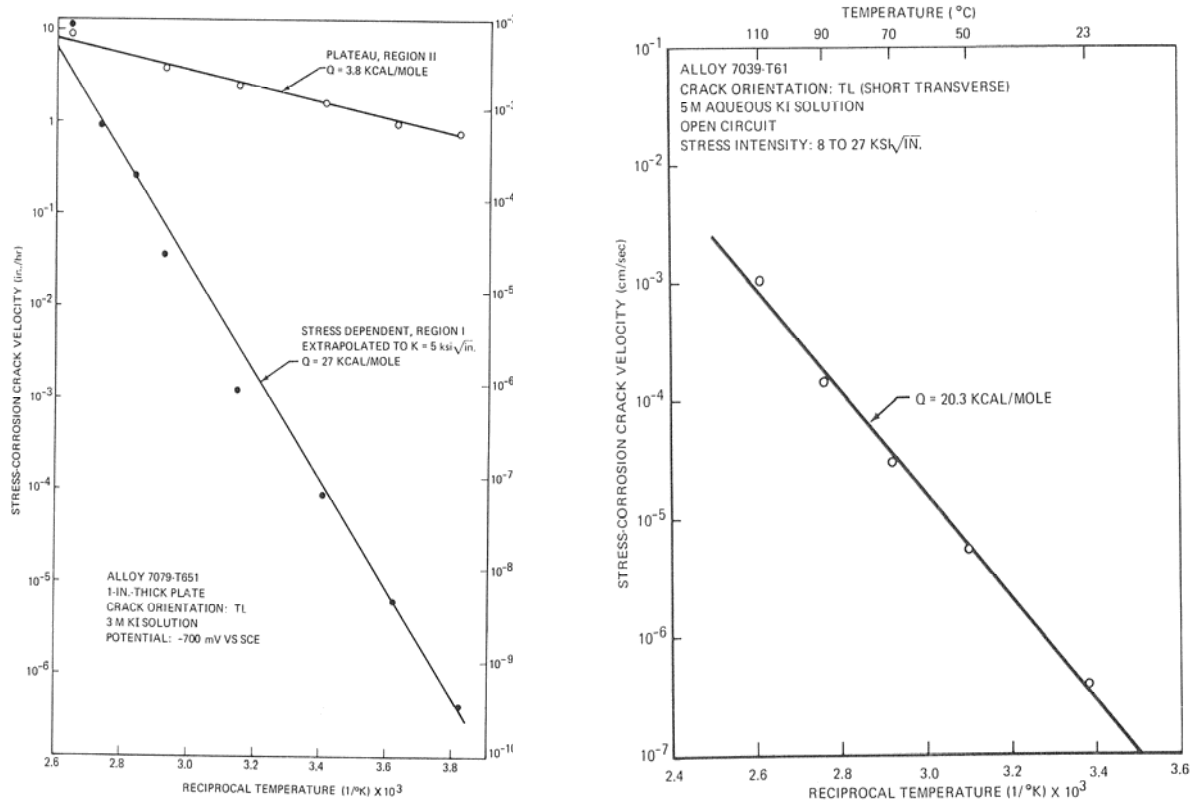
Figure 1.13 Crack velocity vs. reciprocal temperature plots for a. 7079-T651 and b. 7039-T651 where the slope is the apparent activation energy for crack growth. For EIC of 7079-T651 Stage I (stress intensity dependent region) and Stage II (stress intensity independent region) cracking are thermally activated while for 7039-T651 only Stage II varies with temperature. (Speidel and Hyatt)[22]

1.1.2   EIC Mechanistic Theories

Until the mid 1970's SCC of Al-Zn-Mg alloys was thought to occur by anodic dissolution of the grain boundary region exacerbated by stress. More recently many investigators have demonstrated hydrogen embrittlement is involved in the EIC mechanism of these alloys. The original anodic dissolution mechanistic understanding and the most prevalent proposed hydrogen embrittlement mechanisms are summarized in this section.

1.1.2.1 Anodic Dissolution/ Film Rupture Mechanisms

Aluminum alloys that are susceptible to SCC generally are characterized by microstructures that exhibit localized decomposition at the grain boundaries establishing electrochemically active paths. In anodic dissolution theory, corrosion along these localized paths produces fissures with normal components of the tensile stress concentrated at the tip of the fissures. With sufficient concentration of stress to cause localized plastic deformation at certain grain boundaries, the fissures propagate exposing fresh unfilmed metal to the corrosive electrolyte. Strain–assisted corrosion results in further metal separation and increased rate of penetration due to the mutually accelerating effects of plastic strain and corrosion.[54] This generalized theory, proposed nearly 60 years ago, is consistent with many experimental observations. There are however, some experimental observations that it does not explain. As Speidel[55] has pointed out, it does not account for the experimentally observed reality that some materials that are susceptible to intergranular corrosion are not susceptible to intergranular stress corrosion cracking (IGSCC) and others are susceptible to IGSCC without apparent susceptibility to intergranular corrosion. Also, in some cases crack growth rates are proportional to anodic dissolution currents at straining electrodes, but in other systems crack growth rates are faster than can be accounted for by electrochemical dissolution rates.

At the tip of a growing pit or stress-corrosion crack in a neutral or slightly alkaline chloride bulk environment (bromide or iodide behave similarly but are less common) bare metal oxidizes via the half cell reaction $Al \rightarrow Al^{3+} + 3e^-$. In aqueous environments with relatively low chloride concentrations the aluminum ions will react with water to form a hydrated oxide and hydrogen ions:

$$Al + 3H_2O \rightarrow Al_2O_3 + 6H^+ + 6e^- \quad [1.13]$$
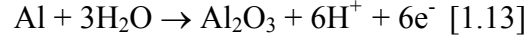
Or alternatively, with higher concentrations of chloride ions:

$$Al^{3+} + 3Cl^- \rightarrow AlCl_3 \quad [1.14]$$
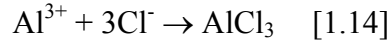
Combinations of these reactions and/or similar reactions to form halogenated oxides and/or oxy-hydroxides are also possible. The Mass Transport Kinetics (MTK) model[22] assumes that some active species, e.g. chloride, is required at the crack tip for accelerated stress corrosion crack growth, and that the cracking velocity is limited by the rate of transport of that species to the crack tip. If the rate at which chloride ions are transported is measured as current density, $I\_$ (per unit thickness of the specimen):

$$I\_ = 2nq_xV \quad [1.15]$$

Where n is the number of monolayers of halide ions adsorbed on the surface of the crack walls, q_x is the charge density of a monolayer and V is the crack tip velocity. A probable estimate of n for aluminum is n=30.[22] The current is related to the mass transport flux (j):

$$I\_ = zFAj \quad [1.16]$$

Where z is the valence number, F is Faraday's equivalent (96500 coulombs), and A is the cross-sectional area of the crack in the unit thickness:

$$j\_ = -D(dC/dy) - zFA(z/RT)DC(D\phi/dy) \quad [1.17]$$

where D is the diffusivity of the species (chloride), C is the concentration of the species, y is the distance from the tip of the crack, and ϕ is the electrochemical potential. Therefore:

$$V = \{D[-zFA(dC/dy) - zFA(zF/RT)C(d\phi dy)]\}/2nq_x \quad [1.18]$$

The first term is a diffusion term and the second term is an electro-migration term. The crack growth velocity is proportional to the concentration (C) of the species (chloride). The diffusivity (D) has an exponential dependence on reciprocal temperature (1/T) and is the dominant

temperature dependence. Assuming the crack tip remains at the mixed potential, there should be a linear relationship between the potential difference (dφ) (between the externally applied potential and the crack tip potential) and the Stage II crack velocity. For an established crack where the tip is saturated with $AlCl_3$, the migration term is dominant and the diffusion term can be neglected.

1.1.2.2 Hydrogen Mechanisms

Many investigators have suggested that the brittle nature of environmentally induced fractures can only be accounted for by a hydrogen embrittlement (HE) mechanism. Yet, the mechanism or mechanisms by which hydrogen induces cracking are not entirely understood. Currently, the three most commonly suggested mechanisms are decohesion, hydride formation, and enhanced localized plasticity. A brief description of each mechanism follows.

In the decohesion model, which was advanced by Oriani,[52] dissolved hydrogen is believed to weaken the inter-atomic bonding forces and thereby reduce the cohesive stress or cohesive energy. Calculations of atomic bond forces using cluster variation methods[53,54] and embedded atom[55] methods provide theoretical support for the decohesion model. While theoretical modeling support for this mechanism exists, direct evidence of bond weakening may not be possible.

DV-Xα cluster method, a molecular orbital method, was used by Yukawa [53] et al. to evaluate the electronic interactions between Mg solute atoms and H atoms in octahedral interstitial sites in aluminum. The effects of other alloying elements (Ti, Cr, Zn, Cu, Li, and Si) on these interactions were also evaluated. The electron density maps on the (100) plane generated by the models showed strong interactions between Mg and H with a concomitant decrease in the electron densities between the two Al atoms neighboring the Mg atom, indicating that the bond strength between these Al atoms was reduced by the existence of hydrogen atoms in the cluster. Without the interstitial H present, the Mg atoms increased the electron density between the Al atoms. The interaction between H and Mg atoms was found to be modified significantly by the substitution of a Cu atom for a Mg atom, decreasing the Mg-H interaction. Similar to Mg, Ti, Cr, and Li strongly interact with the H atoms.

Hydrogen embrittlement in some metals has been reported to be the result of stress induced hydride formation and subsequent cleavage fracture of the brittle hydride phase.[54-57] A hydride phase generally has a large ΔV of formation that can be stabilized by the stress fields at the crack tip. Although this mechanism has generally been linked to metallic systems that form stable hydrides in the absence of stress, in some cases metallic hydrides that are not stable in the absence of stress but become thermodynamically stable under high stress conditions. The hydride is brittle and the critical stress intensity for crack propagation is reduced. Crack propagation is discontinuous as the cracks propagate by cleavage through the hydride to the hydride-matrix interface and then stops until more hydride is formed.

Other authors have proposed mechanisms that involve hydrogen enhanced plasticity (HELP).[13-17, 62,63] In the HELP mechanistic models, high local stress fields at elastic singularities such as crack tips or precipitate particles reduce the chemical potential of solute hydrogen and hydrogen diffusion leads to high H concentrations locally at the tip of the crack. Both Lynch[62, 63] and Birnbaum et al.[17] have supported this basic tenet of the HELP mechanism. Beyond this point however, their views on the mechanism are quite different. In Lynch's view the shear strength of inter-atomic bonds at or very near the surface in the vicinity of the crack tip is reduced by hydrogen adsorption. The locally reduced shear strength facilitates the nucleation of dislocations and cracks propagate via localized plastic flow.

The HELP mechanism as proposed by Birnbaum et al.[17] differs in that they consider the hydrogen effect to occur in the volume of the metal, not just at the surface. In this mechanism the effect of hydrogen is to reduce the stress for dislocation motion. Using time-lapse imaging in TEM experiments, they have observed enhanced dislocation motion in pure aluminum due to presence of hydrogen gas in the chamber. Possible explanations for hydrogen enhanced dislocation mobility include:

1. A decrease in the Peierls-Nabaro stress
2. A decrease in the effectiveness of certain defects such as solute atoms as barriers
3. An increase in kink nucleation rate

Based on direct observation of the behavior of dislocation arrangements in pile-ups including experimental evidence that the direction of the dislocation motion in pure aluminum could be reversed by removing the hydrogen atmosphere, Birnbaum et al. believe the primary

influence of hydrogen is to reduce the interactions between the dislocations and other elastic centers. Their in situ TEM experiments have also shown that fracture occurs along slip planes in a saw-toothed morphology. Pyramidal features bounded by {111} slip planes have been observed on macroscopic fracture surfaces.[64]

G. Lu et al.[16] have used a Semi-discrete Variational Peierls-Nabarro (SVPN) model with ab initio determined γ-surfaces and elastic constants to examine the interaction of interstitial H with dislocations in aluminum. Their calculations indicate a strong binding of H to the dislocation cores that varies with dislocation character. The binding energy to edge dislocations was higher than for screw or mixed dislocations, which would contribute to observed restrictions in cross slip and slip planarity in the presence of H. Their SVPN calculations also indicate that the Peierls stress is reduced by more than an order of magnitude in the presence of interstitial hydrogen.

1.2   SYNOPSIS OF UNIV. OF VIRGINIA, LEHIGH UNIV, ALCOA PROGRAM

Fundamental understanding of the processes responsible for EIC is lacking in part because the role of the localized environment within the crack is not well understood. It is known that the crack environment can differ significantly from bulk conditions. Local acidification results from hydrolysis of cations produced by anodic dissolution and anions from the bulk electrolyte concentrate within the crack to maintain charge neutrality. Ohmic potential drop results from migration and diffusion of ions.[3]

1.2.1   Support for Role of Anodic Dissolution

K. Cooper's work showed that the crack tip environment plays a critical role in the crack growth rate (da/dt) of EAC-susceptible alloys.[3] The transition from slow incubation cracking to steady state high-rate da/dt coincides with the establishment of a critical aggressive tip chemistry and tip depolarization (Figure 1.14). Development of the critical occluded chemistry necessary for accelerated da/dt is a competitive process between opposing forces. Electrochemical

dissolution, hydrolysis and migration tend to promote generation of an aggressive environment whereas diffusion acts to reduce concentration gradients and thereby retard the formation of an occluded chemistry different from the bulk.

Cooper[3] demonstrated a positive correlation between crack growth rate (da/dt) and the tip $[Al^{3+}]$, $[Cl^-]$ and $[H^+]$ for EAC-susceptible AA 7050-T6 material exposed to a corrosion-inhibiting chromate-chloride solution. Tip pH was 2 to 4 and presumed to be established by the $[Al^{3+}]$ via the reaction: $Al^{3+} + H_2O = AlOH^{2+} + H^+$. The tip potential ($E_{Tip}$) was approximately -0.90 V_{SCE} and independent of E_{App} over a wide range. The low E_{Tip} and acidic conditions promote H^+ reduction.

The exceptional EAC resistance of over-aged AA 7050 however, appeared to be intrinsic. Injection of an acidic $AlCl_3$ solution at the tip of a crack of this material while polarized to a high E_{App} failed to induce brittle crack advance. Analysis of the environment within fracture specimens exposed 20 years to an industrial atmosphere corroborated the intrinsic cracking behavior of AA 7xxx alloys as a function of aging condition. Although the occluded chemistry was essentially independent of aging condition, crack extension was significantly greater for peak-aged material in comparison to over-aged material. Modeling of the crack potential distribution indicated that the crack tip dissolution kinetics are sufficient to account for 10 to 100% of the observed da/dt of peak-aged AA 7050 but cannot account for the strong E_{App}-dependence of da/dt suggesting that HE also plays a significant role in the crack tip damage mechanism.[3]

L. Young[2] evaluated the effects of applied electrode potential on crack growth of AA 7050 in chromate inhibited chloride solution (0.5M Na_2CrO_4 + 0.05M NaCl) and observed that the response to applied potential was rather complex in this environment. The peak-aged and under-aged tempers exhibited a transition potential, below which intergranular crack growth occurred with a mild dependence on applied potential as illustrated for the T6 temper in Figure 1.15. Above the transition potential, fast rate intergranular cracking occurred. Subsequently lowering the applied potential below the transition potential decreased CGR with a strong dependence on applied potential but did not return CGR to the low pre-transition rates. The transition potential increased to more noble potentials as isothermal aging time increased. Over-aged AA 7050-T74 did not exhibit a transition potential or a dependence of crack growth on applied potential over a wide range of applied potentials.

As discussed in the Isothermal Aging Treatments section, over-aging in the lower temperature range of 120-135°C (248-275°F) for extended times to achieve the same tensile properties as the higher temperature treatment (160-170°C), does not result in the same degree of SCC improvement as measured by time to failure. The fast crack rates (above the transition potential) in Figure 1.16 for material thermally processed at these low aging temperatures indicates no difference in the crack growth rates when compared with material aged at the higher temperatures to the same %IACS in direct contrast to the time to failure results in Table 1.2. Electrochemical evaluations in a far less inhibited chloride environment of 0.1M NaCl + 0.01 NaHCO$_3$ M show a significant difference in the repassivation potentials of EIC resistant tempers and EIC susceptible tempers that is more consistent with the time to failure results[65] (Figure 1.17). The repassivation potentials (E$_{rp}$) for a limited selection of the aging times at 325˚F used in this study were evaluated in this previous work and are summarized in Table 1.3.

Table 1.3 Repassivation potentials for AA 7050
with selected aging times at 325˚F. [65]

Aging Time at 325˚F (hours)	E$_{rp}$ (V vs SCE)
1	-0.845
6	-0.779
18	-0.742
27	-0.735

Crack Length *vs.* Time

7050 #50-103
12 hour at 163 °C
0.5 M Na$_2$CrO$_4$ + 0.05 M NaCl, pH 9.2

Change E$_{APP}$

Probe Hole

Applied and Crack Potential *vs.* Time

Applied E

Crack E

pH and [Cl$^-$] *vs.* Time

Bulk pH

Cl$^-$

Bulk Cl

pH
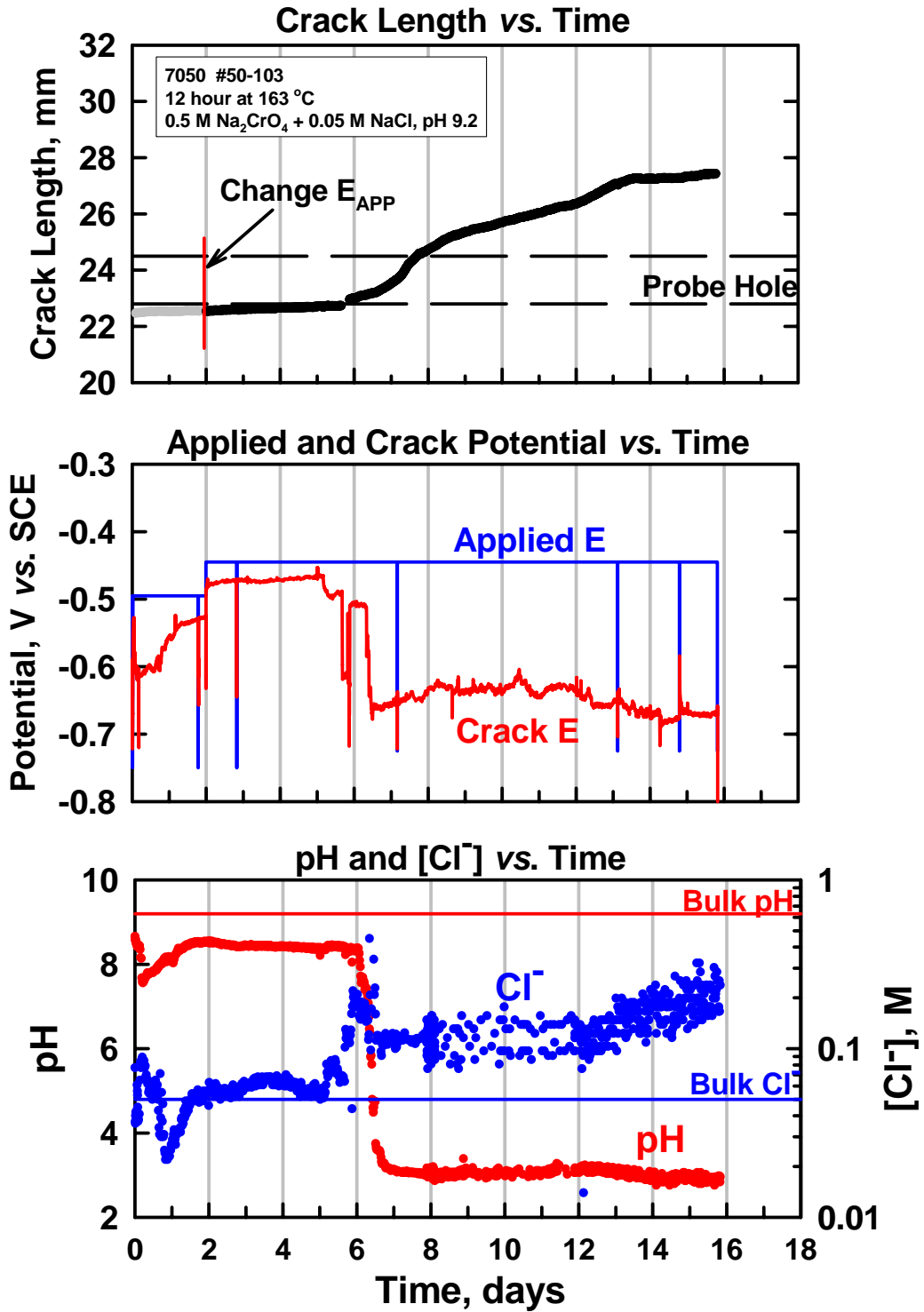
Figure 1.14   In–situ crack pH and Cl$^-$ and potential measurements. (K. Cooper)[3]
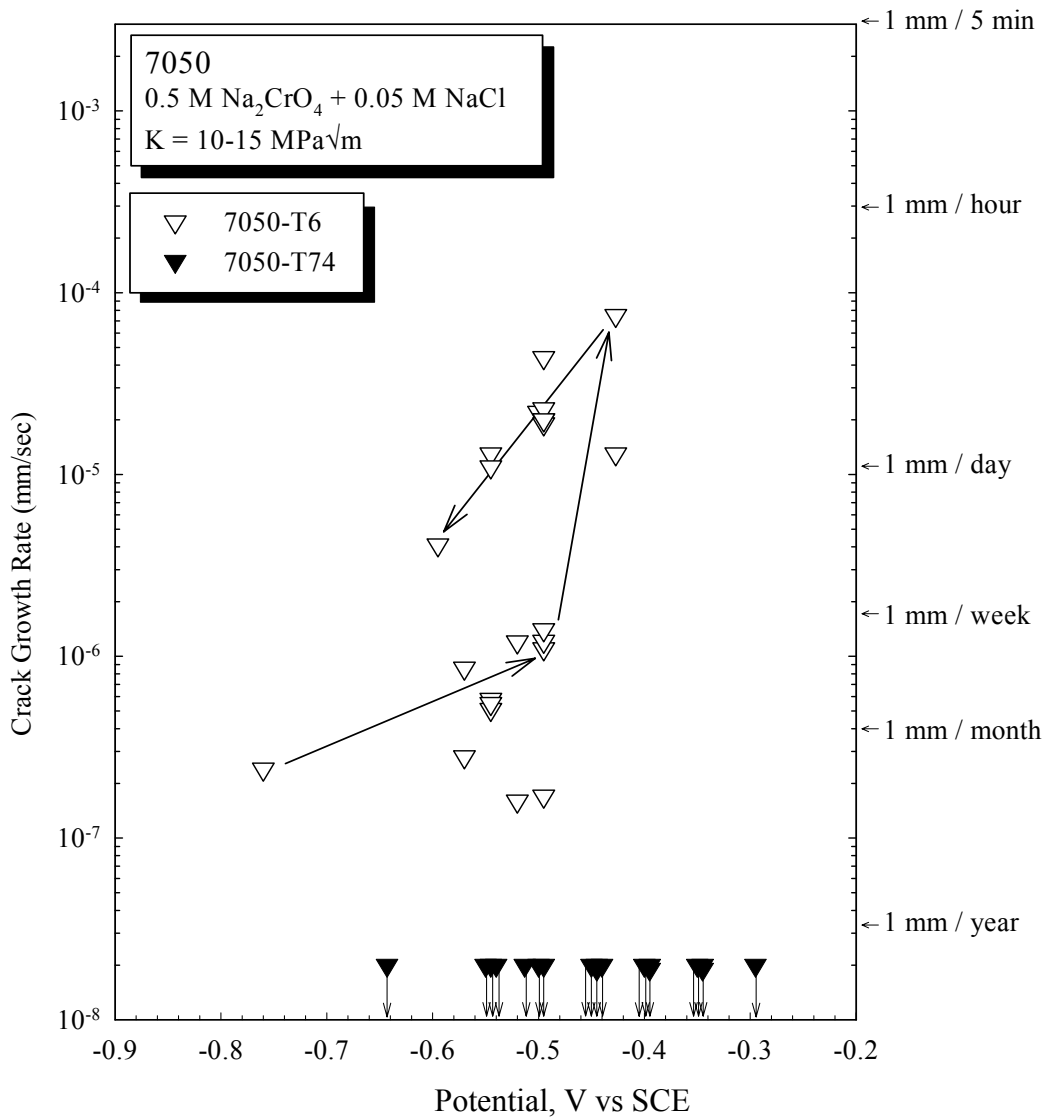
Figure 1.15 Potential Dependence of EIC crack growth rates of peak-aged (T6) and over-aged (T74) AA7050 in chromate inhibited NaCl solution. (L. Young)[2]
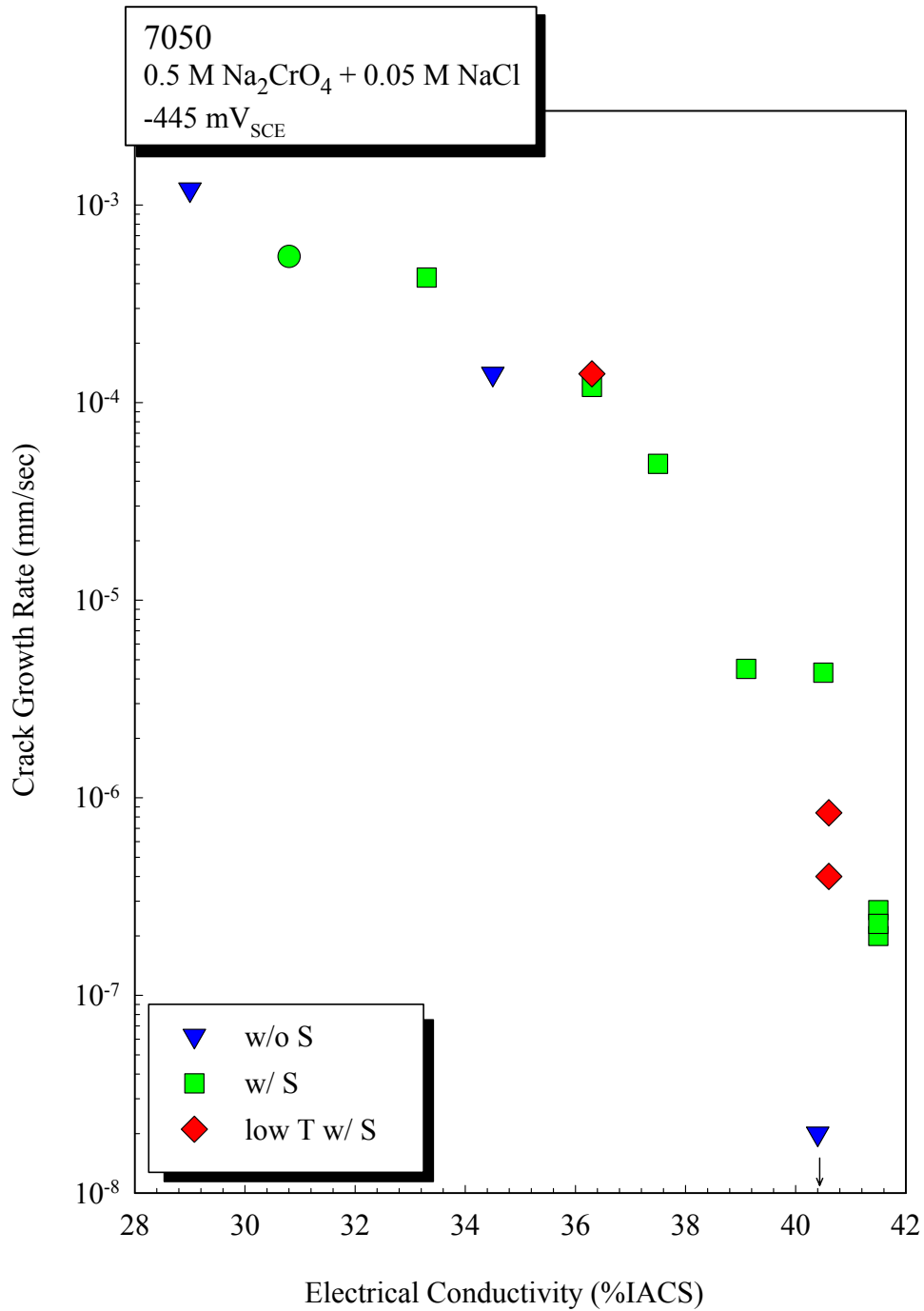
Figure 1.16   Crack growth rate measurements for various tempers of AA 7050 in chromate inhibited environment under applied potential above transition potential showing that low aging temperature (163°C vs. 121°C) does not affect da/dt when compared at equal %IACS. (L. Young)[2]
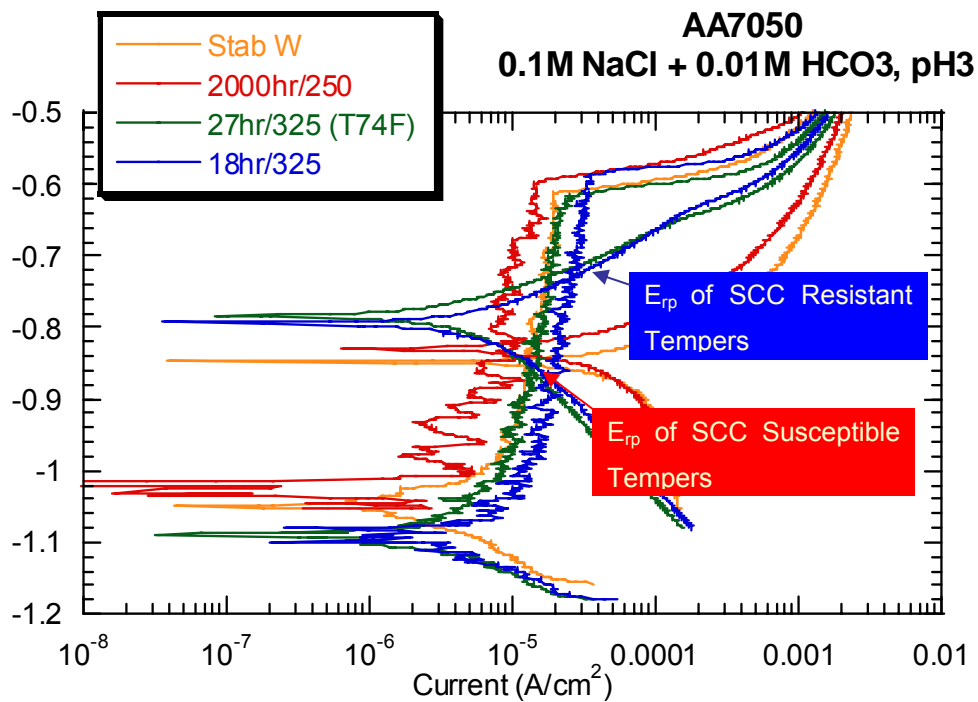
Figure 1.17   Potentiodynamic polarization curves for various tempers of AA 7050 in 0.1M NaCl + 0.01 NaHCO$_3$ M showing a significant difference in the repassivation kinetics of EIC resistant tempers and EIC susceptible tempers that is consistent with the time to failure results in ASTM G44 testing. [65]

1.2.2 Support for Role of Hydrogen Embrittlement

G. Young[2] measured crack growth rates for various tempers of AA 7050 in 90% RH air at temperatures ranging from 25°C to 90°C and observed this Arrhenius-type temperature dependence of Stage II crack velocities (Figure 1.18). His results indicate that both V_0 and $Q_{effective}$ in Equation 1.10 increase with increasing aging time from under-aged to peak aged to over-aged. Note that increases in $Q_{effective}$ would reduce crack growth rates while increases in V_0 would produce higher crack growth rates. Crack growth rate temperature dependence was also evaluated for a low Cu version of 7050. Both V_0 and $Q_{effective}$ are significantly lower for the low Cu material relative to AA 7050. Additionally, V_0 appears to decrease slightly and $Q_{effective}$ remains unchanged with aging from peak-aged condition to over-aged condition (Figure 1.19). Stage II (stress independent) crack growth rates for AA 7050 and low Cu variant shown in a) exhibit Arrhenius-type temperature dependence of a thermally activated process. Activation energies in b) show increases in the activation energy with aging from under aged condition (UA) to peak aged condition (PA) and from peak aged to over aged condition (OA) for AA 7050, but no increase in activation energy for low Cu variant for aging from PA to OA.(G. Young, 1999)[2]

A thorough investigation of diffusion and trapping of hydrogen in high purity aluminum and AA 7050 was also conducted by G. Young.[2] The investigation included constant heating rate desorption and differential scanning calorimetry of pre-charged specimens to elucidate the effects of microstructural trap states on hydrogen egress, isothermal desorption to determine apparent activation energy and diffusivity for lattice diffusion, and straining electrode tests to evaluate the influence of trap states on the effective diffusion coefficient. The results of the investigation on high purity polycrystalline aluminum indicate that the discrepancies in the previously reported values were due to lack of understanding of hydrogen-microstructure interactions. By quantifying the trapping effects of lattice defects (dislocations and vacancies) he showed that some of the literature values reflect lattice diffusion while others appear to be trap-affected values. The diffusivity and activation energy for lattice diffusion in high purity aluminum determined by this study were $1.75 \pm 0.15 \times 10^{-8}$ m^2/s and $16.2 + 1.5$ kJ/mol respectively, with 95% confidence.

For AA 7050 he found that the under-aged and peak-aged tempers had approximately the same activation energy for hydrogen diffusion as high purity aluminum (~16kJ/mol) but the over-aged temper had significantly higher activation energy for hydrogen diffusion (~32kJ/mol). The low copper variant included in these studies exhibited activation energy for hydrogen diffusion of ~14kJ/mol in the peak-aged temper and the activation energy did not increase with over-aging (Figure 1.20). The observed changes in activation energy for lattice diffusion with over-aging also appeared to correlate with the changes in activation energy for crack growth measured in the same study as illustrated in (Figure 1.22). The activation energy for crack growth and the activation energy for lattice diffusion of hydrogen both increase by ~16kJ/mol when AA7050 is aged from peak strength to the over-aged condition. It should however be noted that the activation energy for crack growth also increases by ~16 kJ/mol with aging from the under-aged condition to the peak aged condition (Figure 1.19) but no corresponding change in activation energy for lattice hydrogen diffusion was observed (Figure 1.21). For the low copper version there is no apparent change in either activation energy between the peak aged condition and the over-aged condition (Figure 1.22).

L. Young[1] correlated hydrogen uptake as measured by thermal desorption spectroscopy with crack growth rates that were measured under exposure to an inhibited aqueous chloride solution (0.5M Na_2CrO_4 + 0.05M NaCl). If the cracking mechanism involves hydrogen embrittlement a correlation should exist between the crack growth rate and hydrogen uptake. Initially a clear correlation was not observed but, assuming that the continued uptake of hydrogen in the crack wake during tests of variable time lengths may be confounding the correlation, the authors normalized the measured hydrogen concentrations by dividing by the square root of the average wake exposure time. A clear correlation between normalized hydrogen uptake and crack growth rate was observed for under-aged ('Stabilized' and 1 hr/163°C) and peak-aged conditions (T6 and 6 hr/163°C) as shown in Figure 1.23. The data for the over-aged tempers (18 hr/163°C and 27 hr/163°C) indicate that in addition to exhibiting slower crack growth rates, they also exhibit relatively low hydrogen concentrations. The dotted lines in Figure 1.23 suggest that over-aged tempers may exhibit different hydrogen uptake vs. crack growth rate relationships than the one indicated by the data for the under-aged and peak-aged conditions.

In both the humid air study (G. Young)[1] and the aqueous EIC study (L.Young)[2] of AA7050, comparison of hydrogen concentration profiles of crack wakes and near crack tip region generated by Nuclear Reaction Analyses (NRA) with moving line source and semi-infinite source diffusion solutions showed poor agreement.[1,2] In both under-aged and over-aged AA7050 the kinetics of near surface hydrogen ingress do not appear to be controlled by lattice diffusion. Furthermore, comparison of hydrogen concentration profiles in the pre-crack and near crack-tip regions with those of unstressed coupons showed that hydrogen concentrations at distances greater than ~0.4 to 0.6μm were significantly lower on the unstressed coupons even though the unstressed coupons were exposed to the 90°C and 90% RH conditions for significantly longer times. These increased hydrogen concentrations would appear to be the result of stress enhanced uptake i.e. dislocation transport of hydrogen. This possibility is dismissed by G. Young on the basis that the pre-crack was produced under relatively dry laboratory air conditions (20°C, 22%RH) similar to the post-test fast fracture region where low hydrogen levels were observed. The underlying assumption is that the stresses on the pre-crack region during the test are negligible.
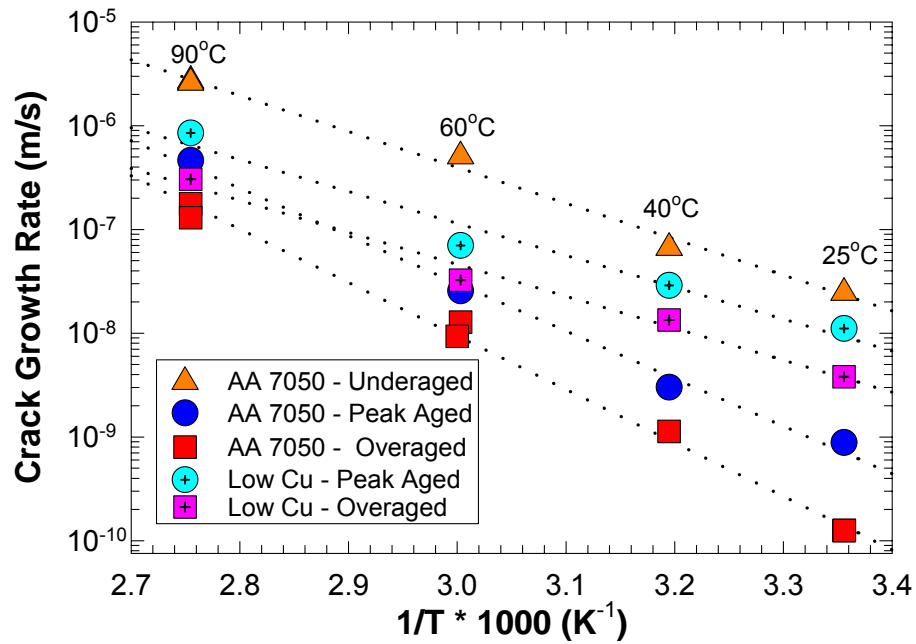
Figure 1.18 CGR as a function of temper and temperature (G. Young, 1999).[2]
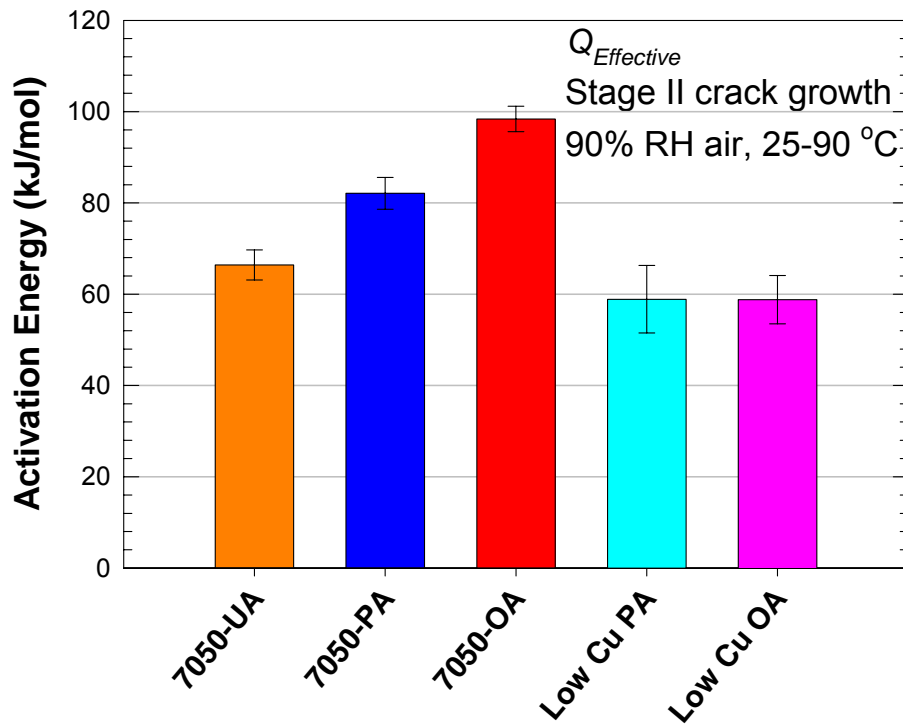
Figure 1.19 Effective activation energy for Stage II crack growth in AA 7050 and a low Cu variant of AA7050 (G. Young, 1999).[2]
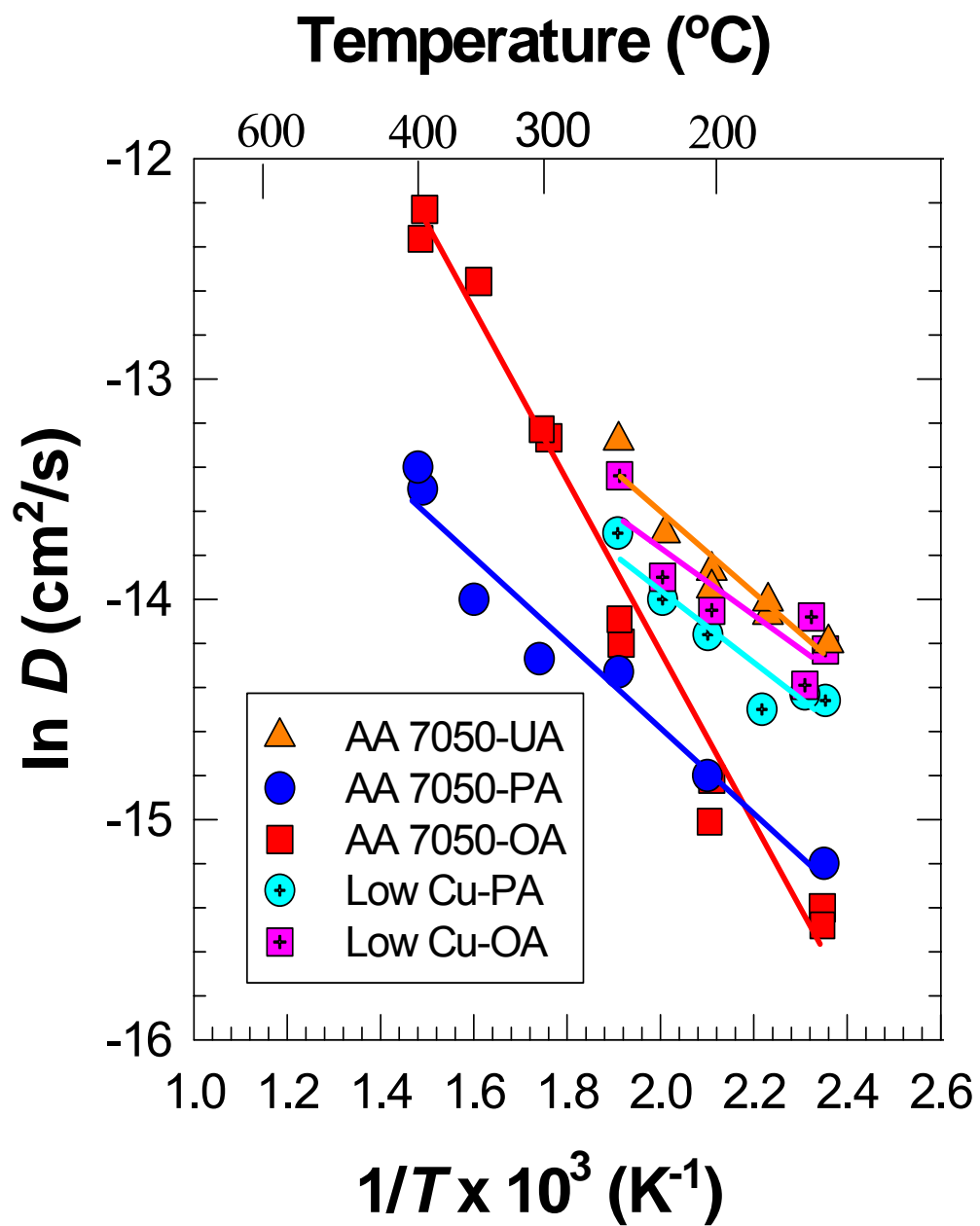
Figure 1.20   Temperature dependence of lattice diffusion of hydrogen (G. Young).[2]
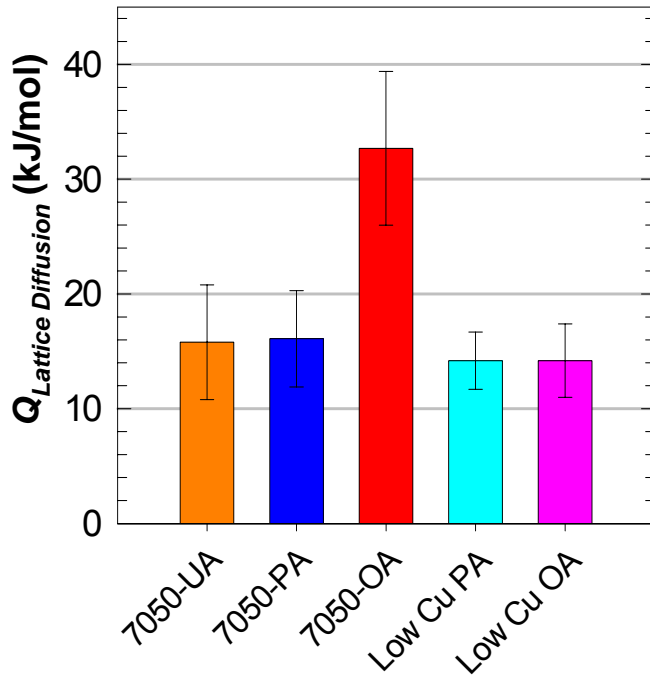
Figure 1.21 Activation energies for lattice diffusion of hydrogen (G. Young).[2]
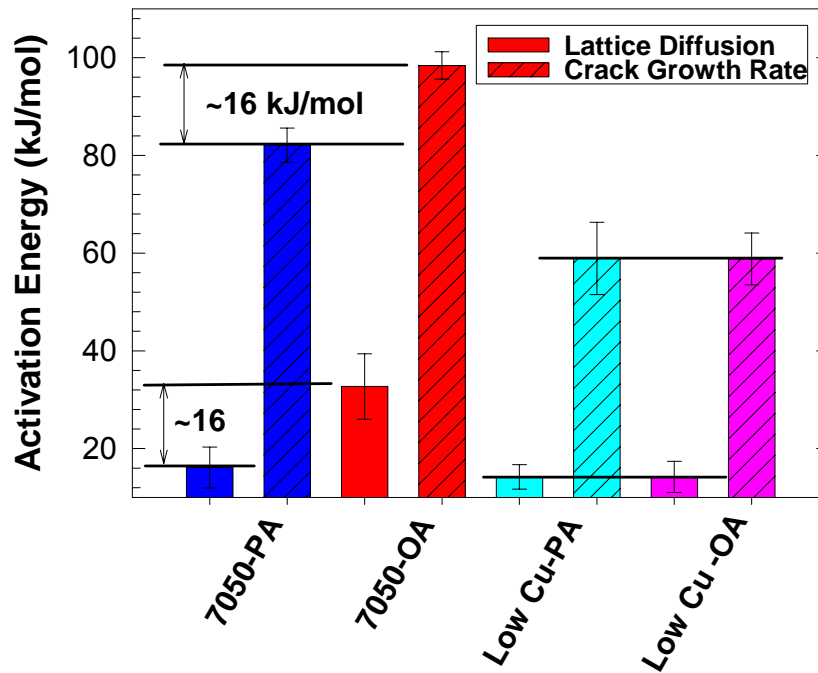
Figure 1.22 Correspondence of changes in activation energy for crack growth and activation energy for lattice diffusion of hydrogen between peak aged and overaged 7050. (G. Young)[2]
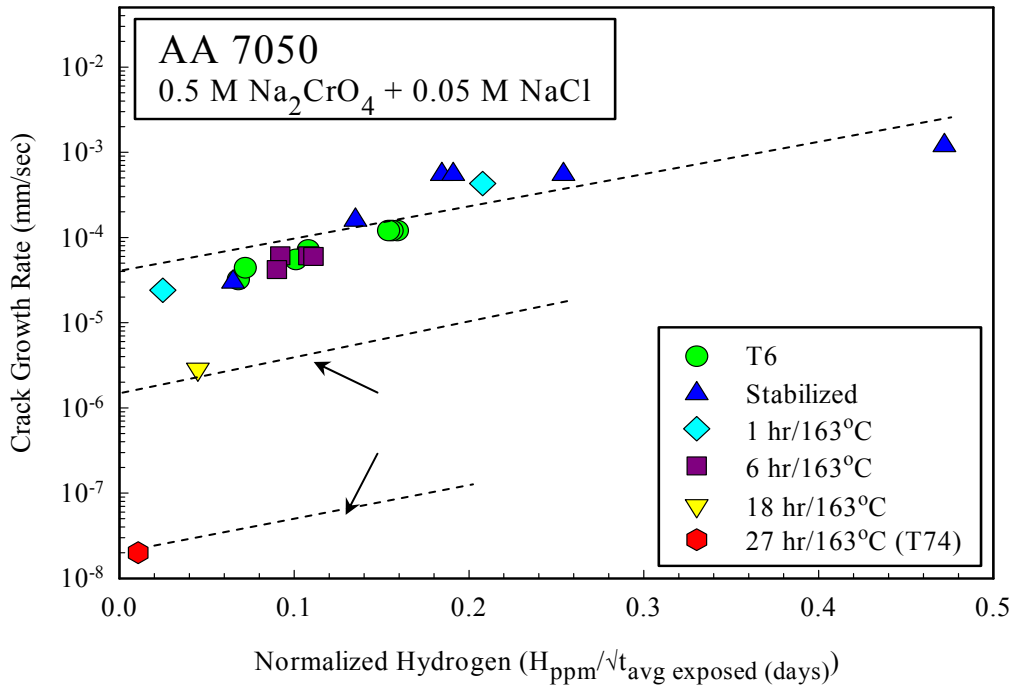
Figure 1.23 Stage II crack growth rate as a function of hydrogen uptake as measured by thermal desorption spectroscopy (TDS) and normalized by exposure time for the crack wake. (L.Young)[1]

2.0   EXPERIMENTAL APPROACH

Earlier it was noted that the Stage II crack growth rate vs. aging time data exhibited a significant change in slope after ~10 hours over-aging at 32°F (160°C) implying that there may be two different rate controlling processes involved. The results of Speidel and Hyatt[22] in Figure 1.3 and those of L. Young in Figure 1.23 appear to be consistent in that they both imply a significant change in the rate controlling mechanism for the over-aged conditions (i.e. aging times greater than ~ 10 hours at 160-163°C). This change is presumed to be related to differences in the local fracture criteria attributable to metallurgical factors. Moreover, it is hypothesized that the change in slope is related to the transition from strain localization due to precipitate shearing (planar slip) of under-aged microstructure to more homogeneous deformation (i.e. wavy slip) in the overaged condition. Speidel[6] and others[7-14] have observed that this transition occurs in 7xxx aluminum alloys and have pointed to a correspondence between slip mechanism and EIC susceptibility. None of these studies however have evaluated this correspondence systematically as a function of isothermal aging.

Speidel and Hyatt[22] showed that this change in slope in the crack growth rate vs. aging time data is coincident with significant changes in the fracture toughness (K_{IC}) as shown in Figure 1.24. For over-aging times less than ~10 hours the fracture toughness does not appear to be affected by aging but beyond ~10 hours over-aging the fracture toughness increases with aging time at 160°C. The data for 7075 in Figure 1.3 indicates that for extended over-aging (30-100 hours at 160°C) the crack growth rate reaches a minimum and remains constant. This minimum crack velocity appears to be coincident with a maximum in the fracture toughness providing at least additional circumstantial evidence that the changes in EIC crack growth rate and the changes in fracture toughness with aging are related to the same microstructural/metallurgical changes. Although Speidel and Hyatt[22] do not comment on the changes in slope or speculate on the coincidence of these changes, the increase in fracture toughness would also be consistent with microstructural or metallurgical changes promoting a

transition from particle shearing and planar slip localization to dislocation bypass and wavy homogeneous slip.[66]

To go a step further, G. Young's observations of increases in activation energy for lattice diffusion of hydrogen and for crack growth rate upon aging from a peak-aged to an over-aged condition may be related to the change in the rate limiting process for crack growth that results in changes in slope for both crack growth rate and fracture toughness at ~10 hours over-aging at 160°C. The lack of change in activation energy for lattice diffusion of hydrogen from under-aged to peak-aged condition is also consistent with the lack of change in the fracture toughness during early stages of the aging process. Figures 1.3,1.19, 1.23 and 1.24 all suggest that a different rate limiting process is controlling the crack growth for aging times of less than ~10 hours over-aging at 160°C. The crack growth rates continuously decrease with aging time from under-aged (Stabilized) to peak-aged to ~10 hours over-aging. There is an apparent increase in the activation energy for crack growth upon aging from the under-aged condition to the peak-aged condition but there is no corresponding increase in activation energy for hydrogen transport/diffusion. Figure 1.23 however, indicates that the crack growth rate is a regular function of the normalized hydrogen uptake for these aging conditions. If transport of hydrogen is not rate limiting for these aging conditions, this dependence of crack growth rates on normalized hydrogen uptake may be an indication that the crack growth rate is controlled by kinetic limitations of the surface reaction processes and/or mass transport processes within the localized crack chemistry that control hydrogen adsorption.

Therefore, the objective this study is to systematically evaluate EIC crack growth rates of AA 7050 as a function of isothermal aging time and to determine if there is a change in slope of the Ln-Ln CGR vs. aging time plots that is coincident with a transition from particle shearing and planar slip to particle looping and homogeneous slip. By evaluating crack growth rates of four aging times of less than 10 hours aging at 325°F and four aging times of more than 10 hours at 325°F changes in slope can be identified and quantified. Using a similar approach to that used by G. Young[2], crack growth rates were measured in humid air at varying exposure temperatures to provide data for analysis of activation energies. By evaluating multiple isothermal aging times it should be possible to elucidate whether the changes observed in activation energy for crack growth rate and hydrogen diffusion by G. Young[2] are related to the change in slope of the Ln-Ln plots of crack growth rate vs. aging time as observed by Speidel and Hyatt.[22] Crack

growth rates were also measured in the same humid air conditions but with the addition of 3.5%NaCl drop- wise three times per day to evaluate the effect the chloride enhanced anodic dissolution on crack propagation. Microstructural analyses (TEM) were also conducted on specimens plastically deformed (2% stretch) after the various aging conditions to examine the evidence of dislocation-particle interactions and identify when the transition from predominantly planar slip and particle shearing to particle looping and homogeneous slip occurs in the isothermal aging process.
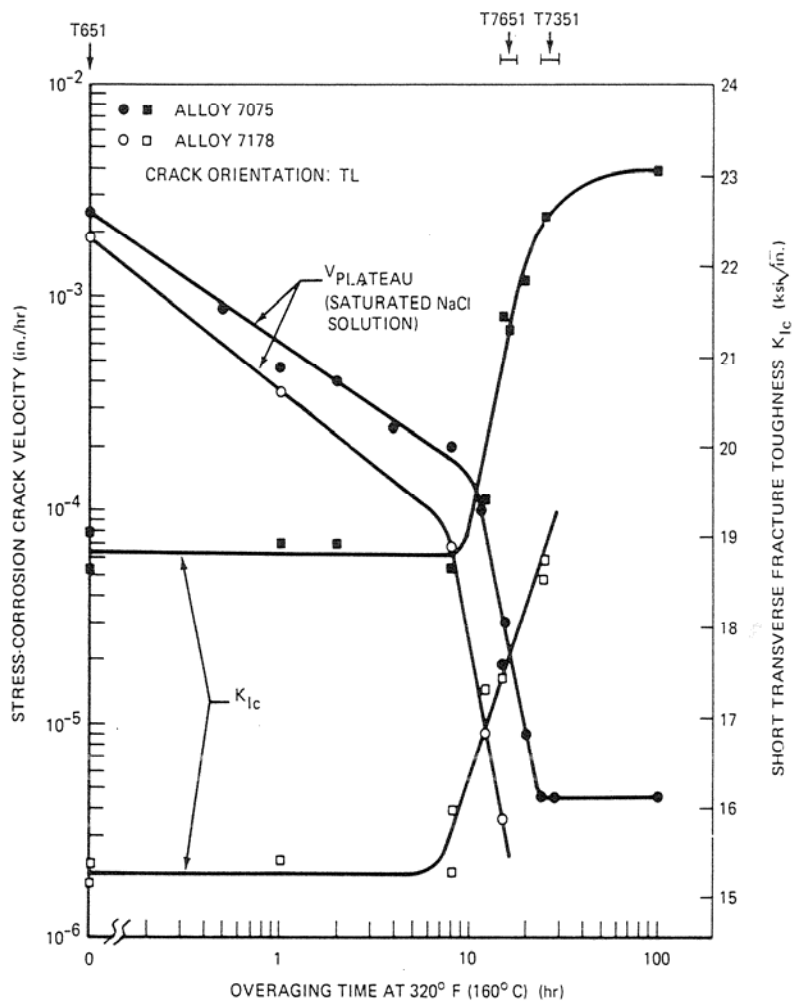
Figure 1.24 Effect of aging at 320F (160C) on the toughness and stress corrosion crack velocity of 7075-T651 and 7178-T651 plate. (Speidel and Hyatt)[22]

2.1   MATERIALS

All samples were taken from the T/4 plane of commercially produced 6" AA7050 plate that was supplied by ALCOA Technical Center. The nominal composition range for AA7050 and the actual composition of the material used in this study are given in Table 2.1. After the plate was solution heat treated and water quenched, it was stretched to 2% plastic strain and then aged for 4 hours at 250F (121˚C) to produce the "Stabilized W" temper. The 2% stretch flattens the plate, removing residual compressive stresses and distortion of the plate from the quench. It also enhances heterogeneous nucleation of precipitates during subsequent aging.[67] The thermal stabilization step is used commercially to mitigate the effects of subsequent natural aging on final properties.

In the "Stabilized W" condition the alloy is extremely susceptible to EIC. Separate pieces of the Stabilized W material were aged for 1, 3, 6, 9, 16, 18, 22, and 27 hours at 325˚F (163˚C) to systematically evaluate the effects of isothermal aging. Limited evaluations were also performed on materials aged for much longer times at 250˚F. By aging at this lower temperature for long periods of time it is possible to achieve mechanical properties and electrical conductivities approximately equivalent to those of the 3 and 18 hour aging times at 325˚F, but the SCC resistance generally is not improved as significantly by "overaging" at this temperature. Mechanical properties and electrical conductivities for all aging conditions in this study are given in Table 2.2 and are plotted in Figure 2.1. The maximum in the tensile yield strength (TYS) and ultimate tensile strength (UTS) occur after ~6 hours at 325˚F (163˚C).

Table 2.1 Chemical composition of AA 7050 in weight percent

ALLOY	Zn	Mg	Cu	Zr	Si	Fe	Al	Zn/Mg
AA7050 (nominal)	5.7-6.7	1.9-2.6	2.0-2.6	.08-.15	0.12*	0.15*	Bal.	2.2-3.6
AA 7050 (actual)	6.09	2.14	2.19	0.11	0.05	0.09	Bal.	2.86

*maximum limit

Table 2.2 Mechanical Properties and Electrical Conductivities

AGING TIME (HOURS)	AGING TEMP (F)	TYS (ksi)	UTS (ksi)	EC (%IACS)
1	325	73.5	84.0	33.6
3	325	75.6	85.2	35.0
6	325	78.4	86.9	37.7
9	325	76.5	85.4	38.1
16	325	73.1	81.8	39.6
18	325	72.5	81.7	40.7
22	325	69.9	80.0	41.0
27	325	66.4	77.7	41.3
750	250	74.5	83.4	36.3
2000	250	72.6	82.1	40.6
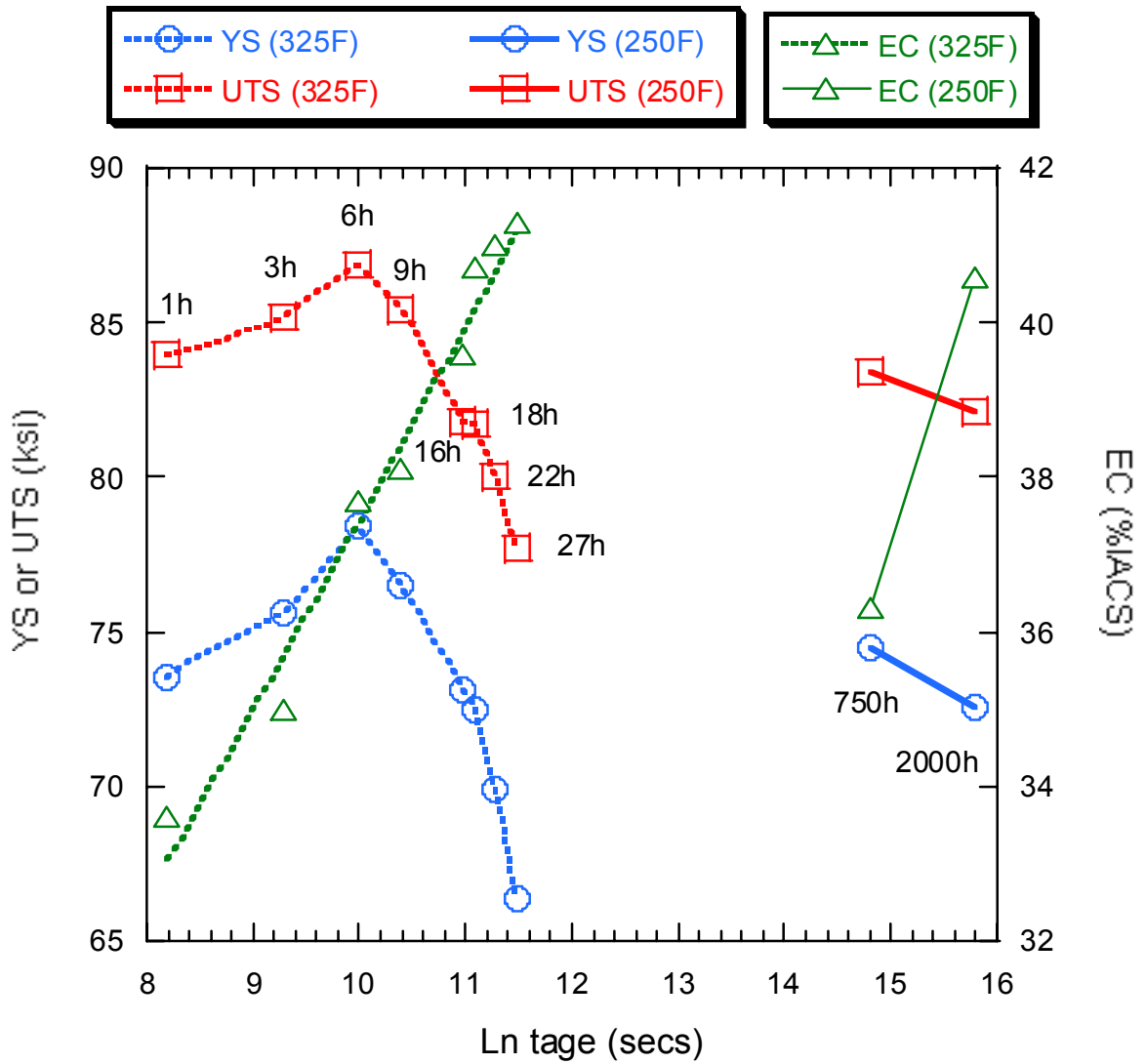
Figure 2.1 Tensile properties and electrical conductivities for 7050 isothermally aged at 325˚F and 250˚F.

2.2 CRACK GROWTH RATE MEASUREMENTS

Pre-cracked specimens use the principles of linear elastic fracture mechanics to evaluate crack propagation rates in the presence of a pre-existing crack.[68,69] This type of testing is particularly useful for wrought materials that display a strong dependence of SCC susceptibility on orientation for which the S-L orientation (S = direction of loading and L = direction of crack propagation) is generally the most susceptible. The standard DCB specimen, illustrated in Figure 2, is designed to provide linear-elastic stress intensity, K_I, at the crack tip under plane-strain conditions. With this specimen design, plane-strain conditions are satisfied if the specimen thickness meets the following criteria:

$$B > 2.5 \, [K_I / \sigma_{ys}]^2$$

where K_I is the applied stress intensity and σ_{ys} is the material yield strength.

Crack growth rate experiments in 90%RH air were conducted on double cantilever beam (DCB) fracture mechanics specimens (Figure 2.2) held at constant mouth opening displacement (CMOD) by stainless steel bolts. The DCB specimens were machined in the S-L orientation from the T/4 plane for all isothermal aging conditions. Tests were conducted in 90% RH air at 40°C, 50°C and 65°C with and without the application of 3.5%NaCl drops applied to the cracks three times per day. Fatigue pre-cracks were introduced in the specimens immediately prior to applying the static load and placing in the 90%RH air.

For these tests, the fatigue pre-cracked specimens were bolt loaded to apply a constant crack opening displacement per ASTM G168.[70] The static constant displacement load was applied by adjusting the load bolts to a specified crack opening displacement. For these constant crack opening displacement DCB specimens the plane-strain stress intensity is given by:

$$K_I = (GE)^{1/2} = \delta \, Eh[3h(a + 0.6h)^2 + h^3]^{1/2} / 4[(a + 0.6h)^3 + h^2a]$$

53

where G is the crack extension force, E is the material's modulus of elasticity, δ is the crack opening displacement, a is the crack length and h is the height dimension of the DCB specimen. For these specimens the stress intensity will decrease as the crack grows (as a increases). An initial stress intensity of ~15ksi(in)$^{1/2}$ was used for all of the crack growth rate testing in this study. This stress intensity has been shown to be well within the K-independent (Stage II) region for 7050 in similar aging conditions at temperatures up to 90˚C.[2] Crack length measurements were made periodically on both sides of the specimens in order to determine the crack growth rates. Duplicate specimens were evaluated for each material condition at all temperatures with and without the application of the 3.5% NaCl solution.

Table 2.3 Short transverse mechanical properties of AA7050 in the isothermal aging conditions evaluated in this study.

Aging Time (hours)	Aging Temp. (F)	Average Days to Failure ASTM G44 at 25ksi	TYS (ksi)	UTS (ksi)	EC (%IACS)
1	325	1	73.5	84	33.6
3	325		75.6	85.2	35
6	325	32	78.4	86.9	37.7
9	325		76.5	85.4	38.1
16	325		73.1	81.8	39.6
18	325	72	72.5	81.7	40.7
22	325		69.9	80	41
27	325	>90	66.4	77.7	41.3
750	250		74.5	83.4	36.3
2000	250	11	72.6	82.1	40.6

Figure 2.2. Detailed drawing of plane strain double cantilever beam specimen.[70]

2.3   MICROSTRUCTURAL CHARACTERIZATION

Material in all of the Stabilized W plus isothermally aged conditions described in the materials section were machined into 2 in. long by 0.020 in. thick dog-bone shaped tensile specimens with a 1 in. gage length. The specimens were sectioned with the 2 in. length in the short transverse orientation. The tensile specimens were then stretched to an additional 2% plastic strain. TEM foils were punched from the center of the specimens. The foils were mechanically thinned to ~0.008 in. using 1000 grit silicon carbide papers and then jet electropolished in a 3:1 mixture of methanol and nitric acid chilled to -30˚C±5˚C.

Foils of each isothermally aged and stretched condition were examined using a JEOL 200CX transmission electron microscope (TEM) at 200kV accelerating voltage and ~115 amp beam current. The foils were specifically examined for evidence of the slip mode during plastic straining. Metallographic cross-sections of selected DCB specimens were also examined for evidence of slip mode after environmental cracking in 90%RH air. Some fracture surfaces of DCB specimens were also characterized by conducting limited scanning electron microscopy (SEM) analyses. High resolution images of the fracture surface were obtained using a XL30 scanning electron microscope equipped with a field emission gun.

3.0   EXPERIMENTAL RESULTS

3.1   CRACK GROWTH RATE MEASUREMENTS

The crack growth rate measurements are summarized in Table 3.1.   Stage II or plateau crack growth rates (CGR) in humid air (90%RH) at 40˚C, 50˚C and 65˚C are plotted as a function of isothermal aging time in Figure 3.1.   At all three temperatures these ln-ln plots of CGR vs. aging time show linear relationships.   However, as has been observed in data from previous studies for 7xxx alloys,[1, 22] there is a distinct change in slope between 9 hours and 16 hours of aging at 325˚F.   Least squares analyses of the linear regions at short aging times (i.e. ≤ 9 hours at 325˚F) have slopes of approximately -1.   For longer aging times at 325˚F (≥ 16 hours at 325˚F) the ln-ln plots of CGR vs. aging time have slopes of ~-4.   In Figures 3.2 and 3.3 the CGR at short aging times (i.e. ≤ 9 hours at 325˚F) and those at longer aging times (≥ 16 hours at 325˚F) are plotted separately so that the CGR scale is expanded for each region.   From these plots it is clear that the CGR is also a function of the 90%RH exposure temperature.   The actual slope and intercept results of least squares analyses of the data in Figures 3.2 and 3.3 are summarized in Table 3.2.

In Figure 3.4 crack growth rates (CGR) in humid air (90%RH) with the addition of 3.5% NaCl applied drop-wise three times per day are added to the ln-ln plots of CGR vs. aging time.   Again, in Figures 3.5 and 3.6 the CGR at short aging times (i.e. ≤ 9 hours at 325˚F) and those at longer aging times (≥ 16 hours at 325˚F) are plotted separately so that the CGR scale is expanded for each region.   With the addition of NaCl it is clear that the CGR is still a function of the 90%RH exposure temperature.   For the short aging times the ln-ln plots of CGR vs. aging time appear to be linear but with slopes that are some fraction of the -1 slope observed without the NaCl as shown in Figure 3.7.   For the longer aging times in

Figure 3.6 the ln-ln plots of CGR vs. aging time do not appear to be linear, particularly at 50°C and 65°C exposure temperatures.

Limited cracking experiments on materials aged for much longer times at 250°F were conducted at 50°C and 90%RH. The crack growth rates for these low temperature aging conditions are also included in Table 3.1. The results show that although aging at this lower temperature for 2000 hours produces mechanical properties and electrical conductivities approximately equivalent to those of the 18 hours at 325°F aging condition, the SCC resistance is not improved significantly by "overaging" at this temperature as shown in Figure 3.8. The addition of NaCl drops does not appear to have a significant effect on the crack growth rates for the low temperature aging treatments. Compared to the 18 hours at 325°F aging condition, the crack growth rate of the 2000 hours at 250°F condition is approximately an order magnitude higher with NaCl drops and nearly two orders of magnitude higher without the NaCl.

Table 3.1. Crack growth rate data from DCB experiments at 90%RH with and without the addition of NaCl drops three times per day.

Aging Time at 325°F	Crack Growth Rates 90%RH No NaCl (m/s)			Crack Growth Rates 90%RH + 3.5% NaCl (m/s)		
(hours)	40°C	50°C	65°C	40°C	50°C	65°C
1	1.54E-08	2.19E-08	3.20E-08	1.76E-08	2.61E-08	3.67E-08
3	5.76E-09	8.82E-09	1.34E-08	1.40E-08	1.76E-08	2.47E-08
6	3.10E-09	3.95E-09	7.27E-09	1.05E-08	1.55E-08	1.76E-08
9	2.05E-09	2.88E-09	5.03E-09	9.53E-09	8.96E-09	1.04E-08
16	6.70E-11	2.15E-10	6.49E-10	7.69E-10	1.17E-09	2.51E-09
18	3.53E-11	1.29E-10	3.10E-10	4.54E-10	5.99E-10	1.46E-09
22		7.06E-11	1.62E-10	1.20E-10	2.77E-10	1.30E-09
27		2.82E-11	7.06E-11		2.82E-10	1.23E-09
Aging Time at 250°F (hours)	Crack Growth Rates 90%RH No NaCl (m/s)			Crack Growth Rates 90%RH + 3.5% NaCl (m/s)		
	40°C	50°C	65°C	40°C	50°C	65°C
750	8.62E-09	9.17E-09	1.69E-08	6.91E-09	6.31E-09	7.06E-09
2000	6.56E-09	7.34E-09	1.52E-08	9.24E-09	8.26E-09	8.82E-09

Table 3.2. Results of least squares fitting of linear data in Ln-Ln plots of CGR vs. aging time at 325˚F in Figures 3.1, 3.5 and 3.6.

Exposure Environment	Aging Time At 325˚F (hours)	Temperature of Exposure (˚C)	Slope	Intercept	Correlation Coefficient R
90%RH	≤ 9	40	-0.91	10.52	0.9997
		50	-0.94	9.89	0.9974
		65	-0.84	10.36	0.9995
	≥ 16	40*	-	-	-
		50	-3.78	19.18	0.9968
		65	-4.08	23.41	0.9935
90%RH + 3.5% NaCl	≤ 9	40	-0.29	-15.47	0.9885
		50	-0.43	-13.89	0.9347
		65	-0.53	-12.69	0.9603
	≥ 16	40	-5.92	43.97	0.9955
		50**	N/A	N/A	N/A
		65**	N/A	N/A	N/A

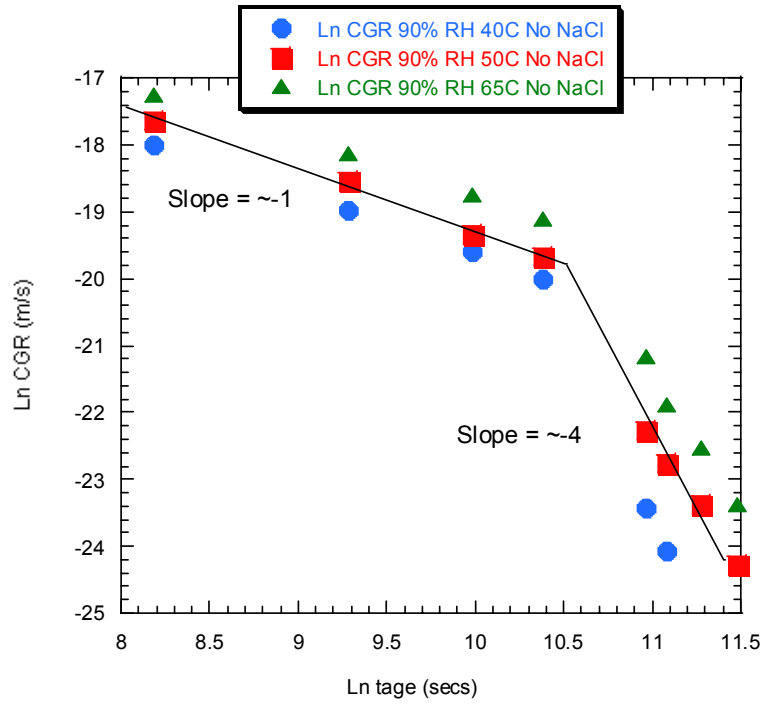*insufficient data for fit
**not linear

Figure 3.1. Ln-ln plot of crack growth rates (CGR) vs. isothermal aging time at 325˚F. (90%RH, No NaCl).
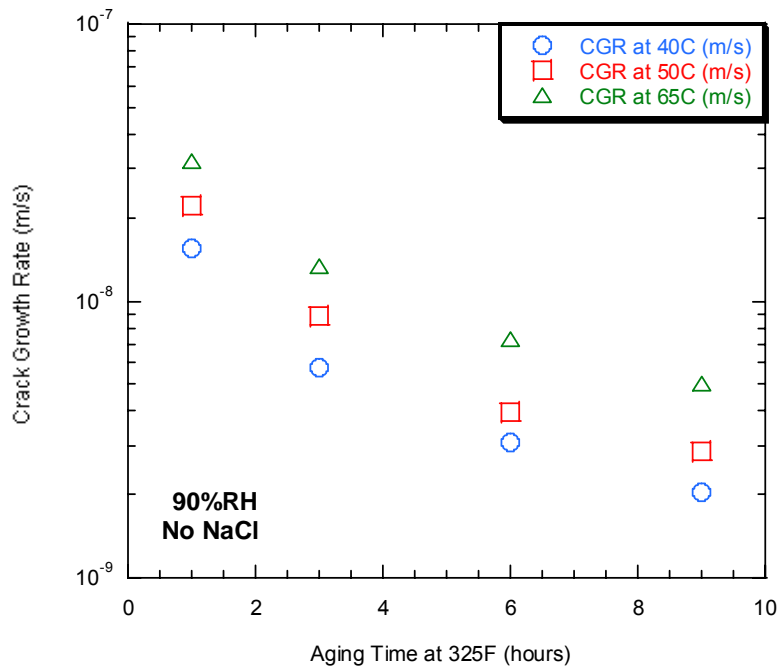

Figure 3.2. Crack growth rates in 90%RH exposure (No NaCl) vs. isothermal aging time at 325˚F for short aging times (i.e. ≤ 9 hours at 325˚F).
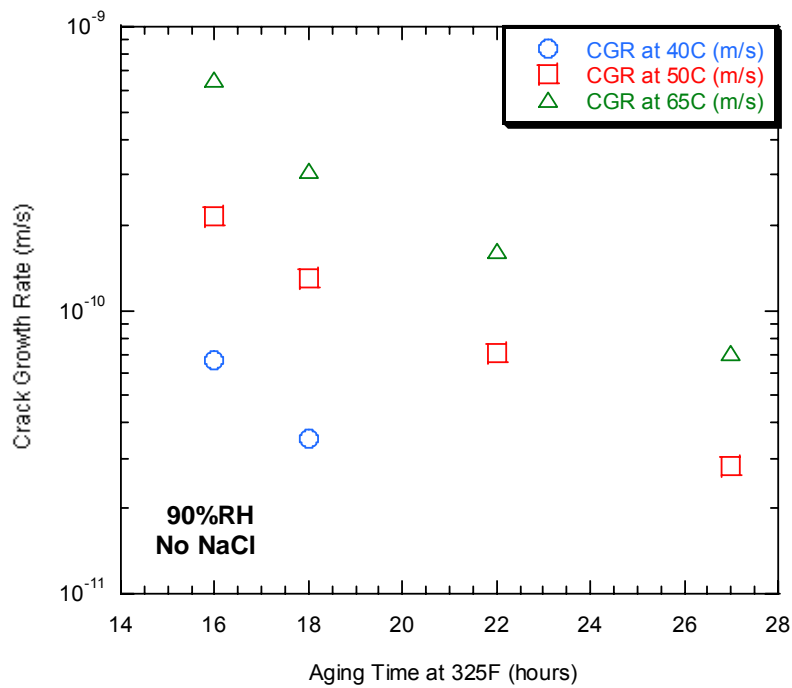
Figure 3.3. Crack growth rate in 90%RH exposure (No NaCl) vs. isothermal aging time at 325˚F for longer aging times (i.e. ≥ 16 hours at 325˚F).

Figure 3.4. Ln-ln plot of crack growth rates (CGR) vs. isothermal aging time at 325˚F, with and without the NaCl drops.
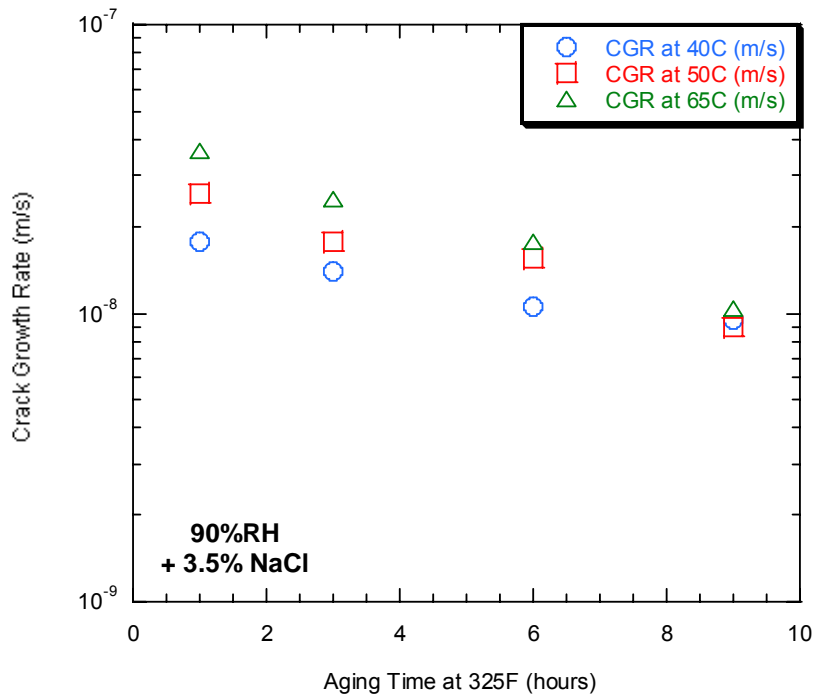
Figure 3.5. Crack growth rates in 90%RH exposure with NaCl drops vs. isothermal aging time at 325˚F for short aging times (i.e. ≤ 9 hours at 325˚F).
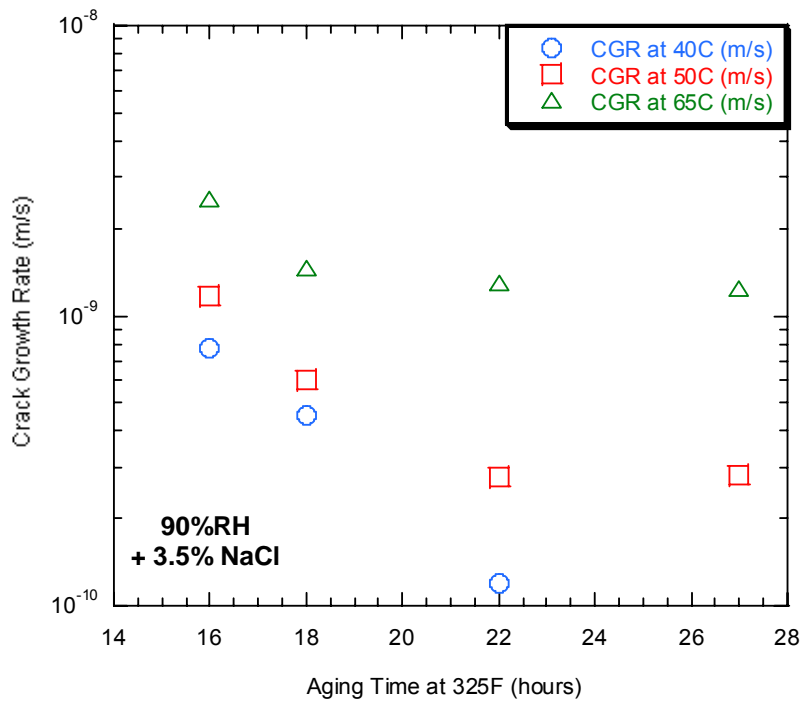
Figure 3.6. Crack growth rate in 90%RH exposure with NaCl drops vs. isothermal aging time at 325˚F for longer aging times (i.e. ≥ 16 hours at 325˚F).
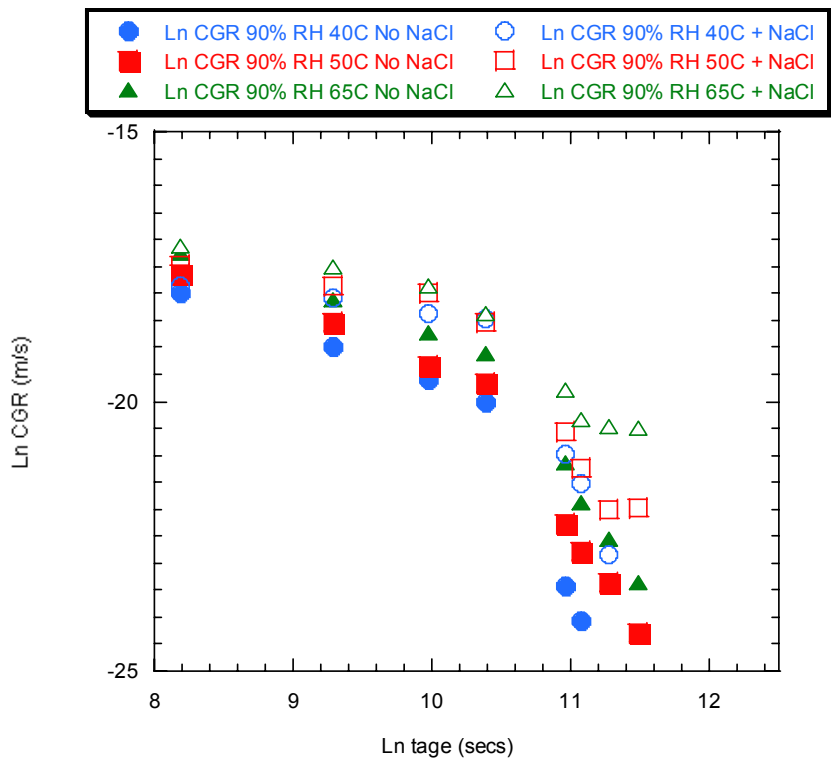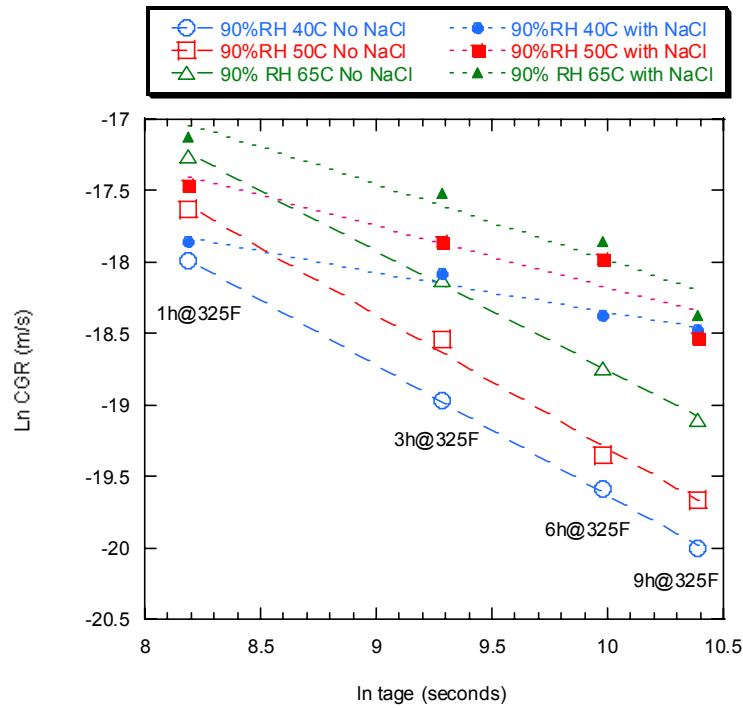
Figure 3.7. Ln-ln plot of crack growth rate in 90%RH exposure with and without NaCl drops vs. isothermal aging time at 325˚F for shorter aging times (i.e. ≤ 9 hours at 325˚F) illustrating slopes with NaCl that are fraction of the -1 slopes without the NaCl.
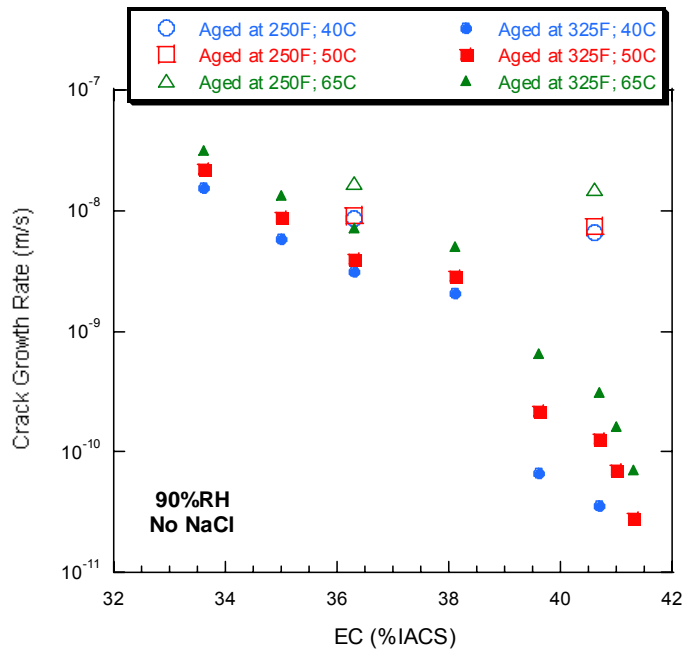
Figure 3.8. Crack growth rate (CGR) vs. electrical conductivity (EC) of AA7050 aged for 1 to 27 hours at 325˚F and for much longer times (750 and 2000 hours) at 250˚F when exposed to 90%RH at 40˚, 50˚ and 65˚C.

Figure 3.9 Crack growth rate (CGR) vs. electrical conductivity (EC) of AA7050 aged for 1 to 27 hours at 325˚F and for much longer times (750 and 2000 hours) at 250˚F when exposed to 90%RH and 3.5% NaCl drops at 40˚, 50˚ and 65˚C.

3.2   ACTIVATION ENERGY ANALYSIS

Previous investigations have shown that the temperature dependence of Stage II crack growth rate of 7xxx alloys is related to a thermally activated process or processes.[71,72] Therefore, the crack growth rate (CGR) or crack velocity is well fit by an Arrhenius-type equation (Equation 3.1) whe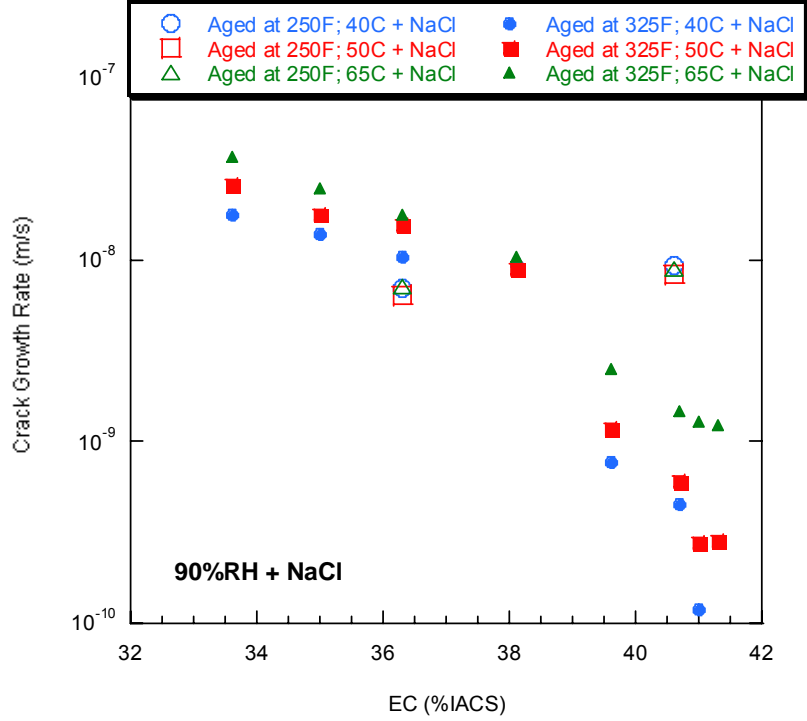re V_{II} is the crack velocity, V_o is a constant, Q is the activation energy for the thermally activated process(es), R is the gas constant and T is the temperature (in ˚K).

$$V_{II} = V_o \ \exp(-Q/RT) \qquad\qquad (3.1)$$

The temperature dependence of crack growth rates measured in this study also appears to indicate an Arrhenius-type temperature dependence as shown by the linearity of the semi-logarithmic plots of CGR vs. reciprocal temperature in Figures 3.10 and 3.11. The slopes of the lines in these semi-logarithmic plots are proportional to the activation energy (Q) for the thermally activated process(es) and the intercept is the pre-exponential constant (V_o). In Figures 3.12 and 3.13 the low temperature aging treatments are added to Figures 3.10 and 3.11. The results of activation energy analysis of the crack growth data in Figures 3.10, 3.11, 3.12, and 3.13 are summarized in Table 3.3.

Table 3.3. Calculated activation energies and pre-exponential values from least squares fitting of Arrhenius plots in Figures 3.10 and 3.11.

Aging Time (hours)	Aging Temp. (˚F)	$Q_{No\ NaCl}$ (KJ/mol)	$Q_{With\ NaCl}$ (KJ/mol)	$V_{o\ -No\ NaCl}$ (m/s)	$V_{o\ -\ With\ NaCl}$ (m/s)
1	325	25.5	25.4	2.88E-04	3.21E-04
3	325	28.4	19.9	3.71E-04	2.94E-05
6	325	30.4	17.5	3.46E-04	9.55E-06
9	325	31.8	3.6	4.07E-04	3.67E-08
16	325	79.1	41.9	8.76E-04	7.42E-03
18	325	75	41.9	7.30E-03	4.17E-03
22	325	50.4	84.4	9.99E-03	1.37E+04
27	325	55.5	89.3	2.61E-02	7.84E+04
750	250	25.5	1.1	1.40E-04	1.01E-08
2000	250	30.6	-1.3	7.53E-04	5.60E-09

Figure 3.10.   Semi-logarithmic plot of crack growth rate vs. reciprocal temperature illustrating the Arrhenius-type temperature dependence of the Stage II crack growth rates for 90% RH exposure (No NaCl). Numbers in legend are aging times at 325˚F in hours.

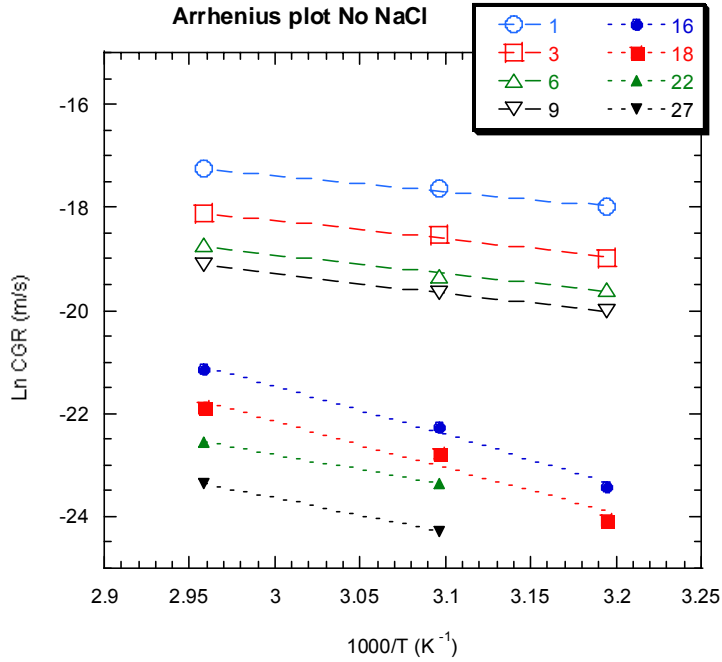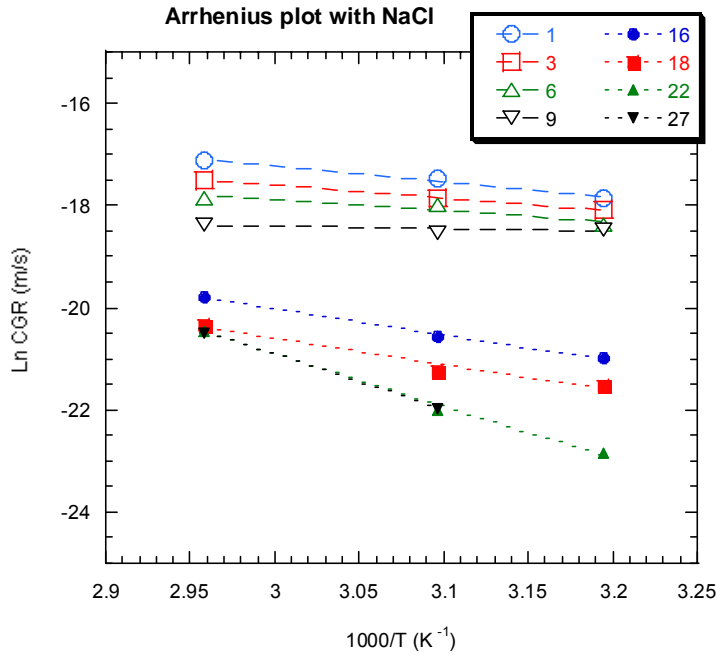Figure 3.11. Semi-logarithmic plot of crack growth rate vs. reciprocal temperature illustrating the Arrhenius-type temperature dependence of the Stage II crack growth rates for 90%RH exposure with the addition of 3.5%NaCl dropwise 3 times per day. Numbers in legend are aging times at 325°F in hours.
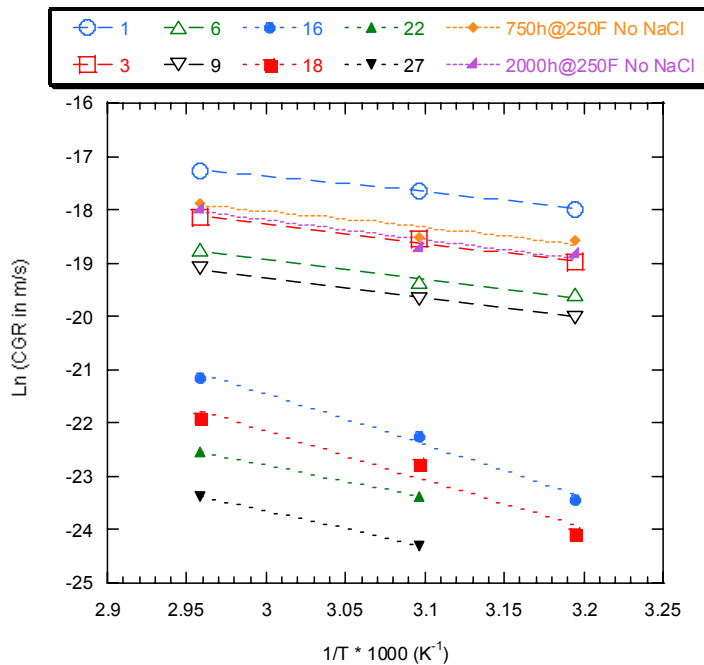

Figure 3.12. Results for low temperature aging treatments (250°F) added to results for aging at 325°F from Figure 3.10.

67
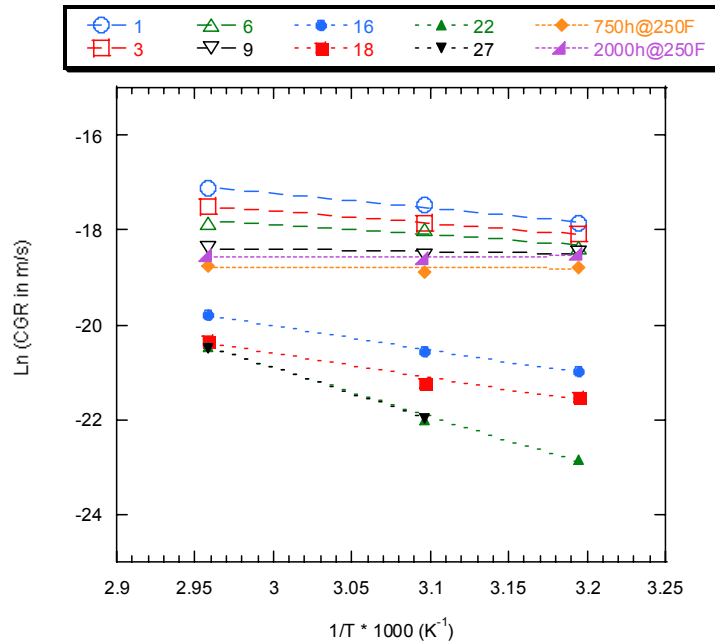
Figure 3.13 Results for low temperature aging treatments (250˚F) added to results for aging at 325˚F from Figure 3.11.

3.3   MICROSTRUCTURAL CHARACTERIZATION

TEM foils of the various isothermally aged and stretched conditions were specifically examined for evidence of the slip mode during plastic straining. Representative bright field images of the 1, 3, 6 and 9 hour aging conditions (325˚F) are shown in Figures 3.14 through 3.17. All of these micrographs show clear evidence of localized bands of planar slip. The spacing between slip bands appears to decrease with increased length of aging from 1 to 9 hours but the banded appearance reflecting the prevalence of predominantly planar slip character persists. The appearance of the bands also varies with the orientation of the imaged grain(s). In Figures 3.14d, 3.15d and 3.17d the selected area diffraction (SAD) pattern indicates that the orientation of the imaged grain was [112] and planar slip is observed on a single orientation of {111} glide planes. In Figure 3.16d the SAD pattern indicates that the

68

imaged grain was oriented in a [110] plane and two sets of {111} glide planes are clearly evident. This is consistent with the respective {111} planes being oriented approximately edge-on with respect to the viewing direction.

Representative images of the 16, 18, and 27 hour aging conditions (325°F) are shown in Figures 3.18 through 3.20. For these longer aging times the banded appearance is not prevalent as it was for aging times of 9 hours or less. At 16 hours of aging careful examination revealed some limited evidence of planar slip as illustrated in 3.18a. However, a significant difference in slip character between 9 hours and 16 hours at 325°F was apparent. For the shorter aging times any non-shearable obstacles (η or η' precipitates) that have formed are relatively small and the glide dislocations can likely overcome them by short distance of cross-glide slip or local climb between sets of parallel glide planes within the narrow glide bands. For the longer aging times however extensive cross-slip and/or particle looping or by-pass become necessary for dislocation movement.

Metallographic cross-sections of DCB specimens for the 9 and 16 hour at 325°F aging conditions examined for evidence of slip mode also appear to indicate a transition from predominantly planar slip for the 9 hour aging condition (Figure 3.21) to predominantly homogeneous slip in the 16 hour aging condition (Figure 3.22). The linear pattern in Figure 3.21 indicates that in the 9 hour aging condition planar slip is prevalent and traverses multiple sub-grains. In Figure 3.22 planar slip character is evident only in the larger recrystallized grains and does not appear to traverse the grain boundaries. The metallographic cross-sections also show the nature of the crack path relative to the grain structure. The images in Figure 3.22 show that although the crack path is predominantly intergranular and/or inter sub-granular, transgranular cracking of the larger recrystallized grains does occur. A metallographic cross-section of a DCB specimen with the 2000 hours at 250°F aging condition was also examined for evidence of slip mode. In this cross-section strain localization and planar slip are prevalent, traversing multiple sub-grains (Figure 3.23). The linear patterns in the 2000 hour at 250°F aging condition in Figure 3.23 appear to indicate a deformation mode of predominantly planar slip. In both Figures 3.21 and 3.23 the evidence of planar slip is found within approximately 50μm of the environmentally induced

crack front which is in good agreement with the size of the plastic zone in these DCB experiments.

The fracture surface of a DCB specimen of the 9 hour aging condition that was tested in the 90%RH environment (No NaCl) was examined by scanning electron microscopy (SEM). The SEM images in Figure 3.24 show regions of transgranular fracture, intergranular fracture as well as some ductile tearing (Figure 3.24). The transgranular regions show parallel markings reminiscent of fatigue striations (Figure 3.24 b. and c.). These striations are often observed with TGSCC of aluminum and are generally interpreted as an indication that the cracking occurs in a discontinuous or incremental fashion. The intergranular regions (Figure 3.24 d-f) also appear to show signs of striations on some facets of the fracture surface (Figure 3.24f.) but these striations are straighter in appearance than those on the transgranular facets.
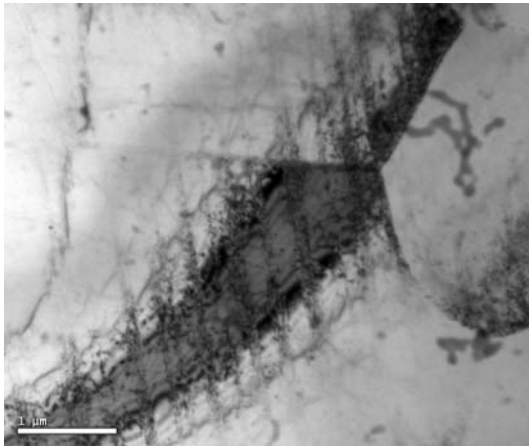
a.
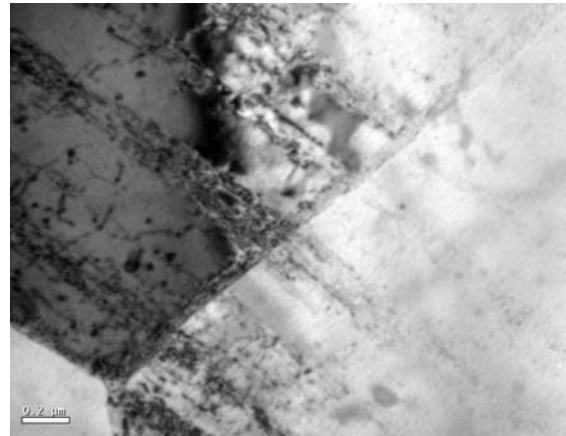
b.
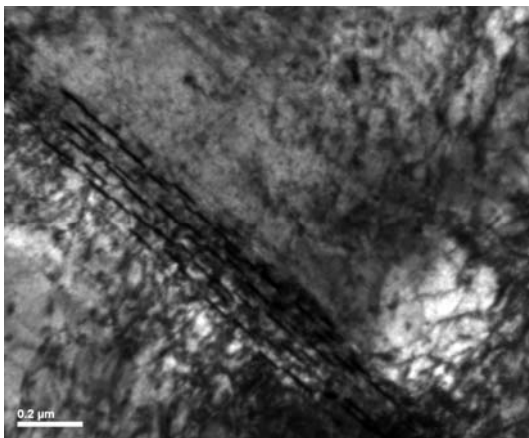
c.

d.

Figure 3.14 TEM images and the corresponding SAD pattern for AA7050 in the Stabilized W plus 1 hour at 325˚F aging condition.

a.

b.
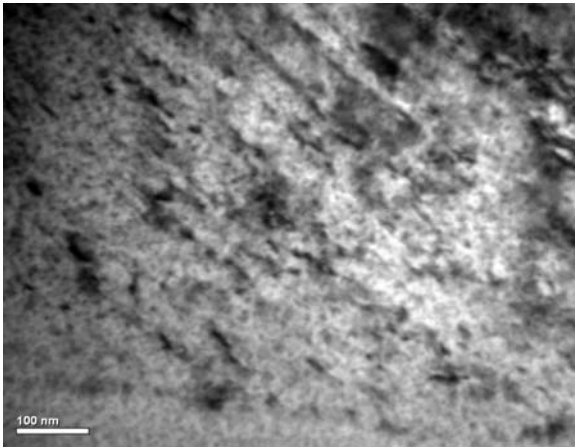
c.
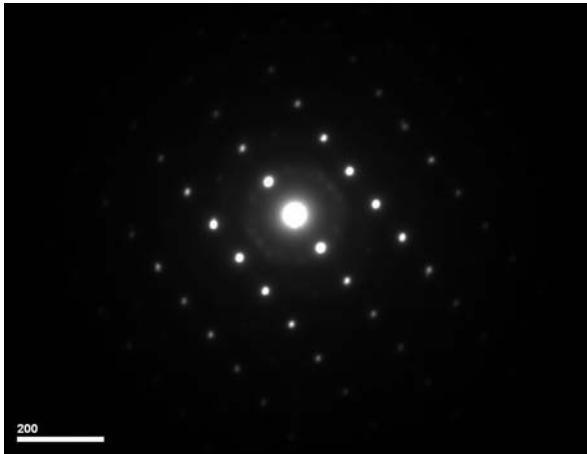
d.

Figure 3.15 TEM images and the corresponding SAD pattern for AA7050 in the Stabilized W plus 3 hours at 325˚F aging condition.
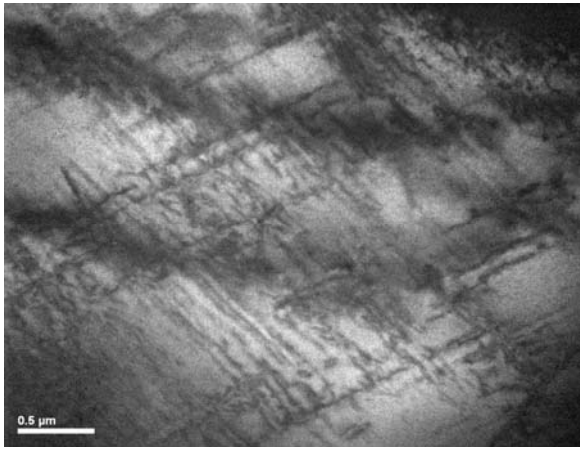
a.
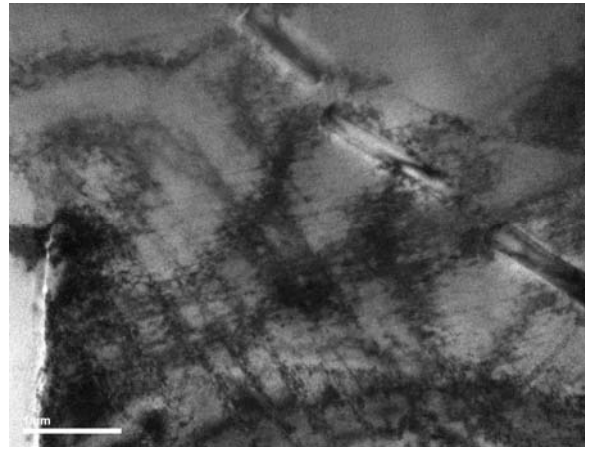
b.
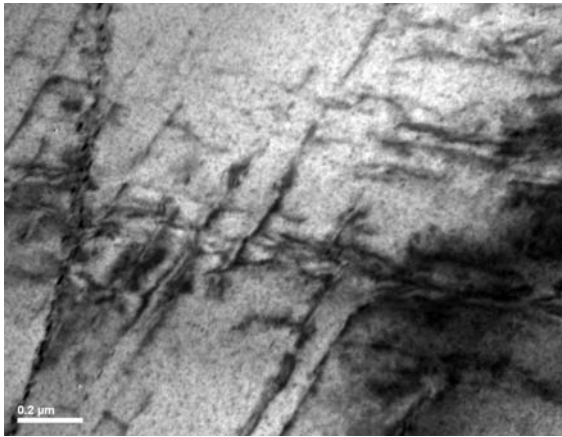
c.
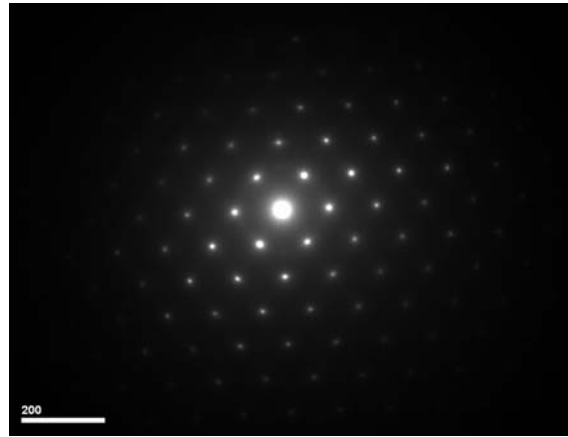
d.

Figure 3.16 TEM images and the corresponding SAD pattern for AA7050 in the Stabilized W plus 6 hours at 325˚F aging condition.
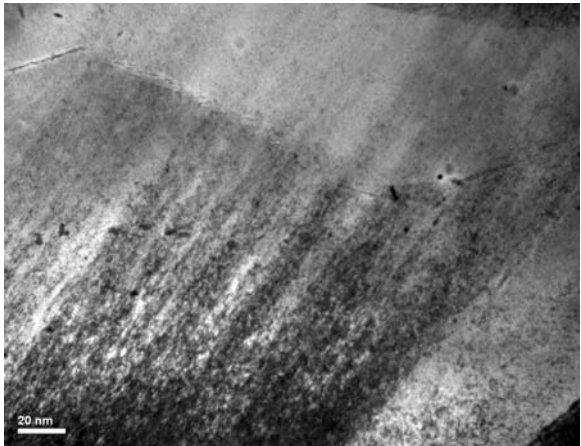
a.
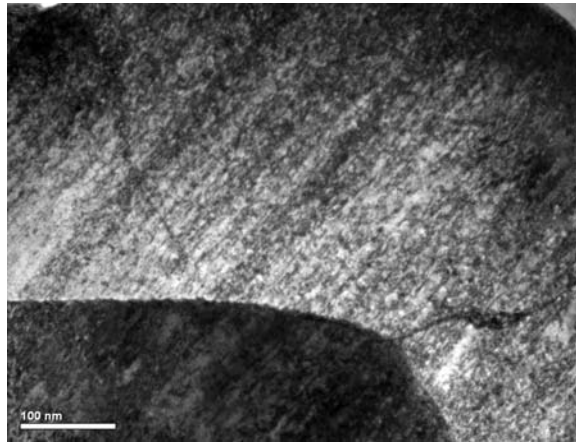
b.
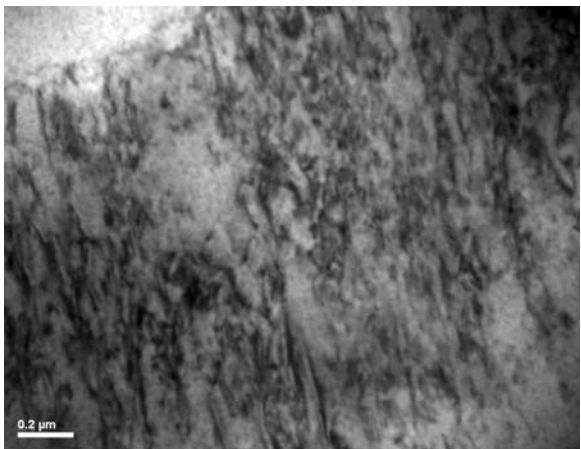
c.
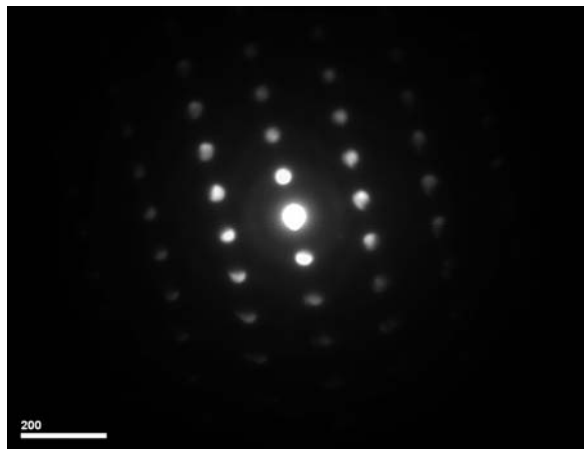
d.

Figure 3.17 TEM images and the corresponding SAD pattern for AA7050 in the Stabilized W plus 9 hours at 325˚F aging condition.
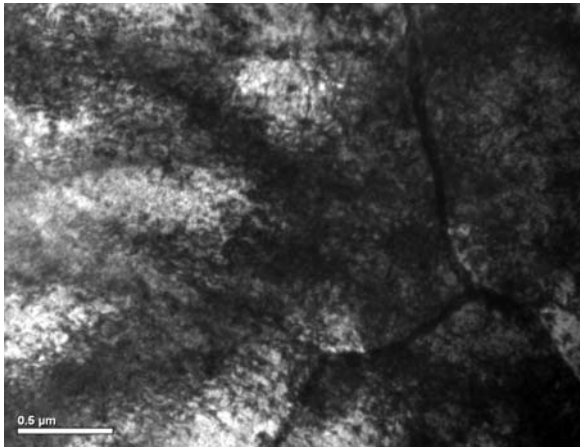
a.
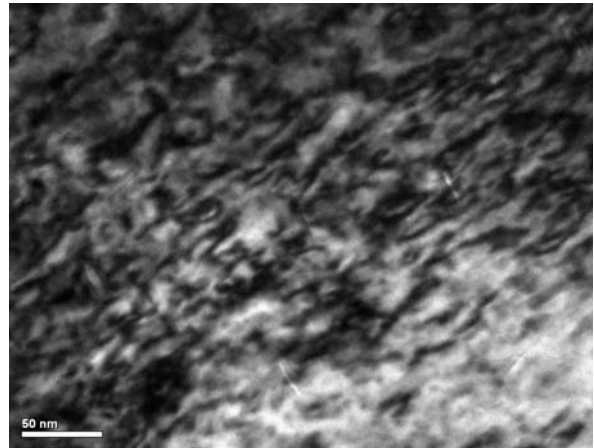
b.
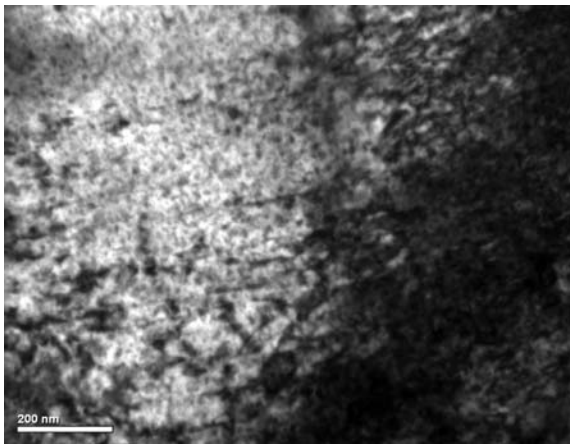
c.
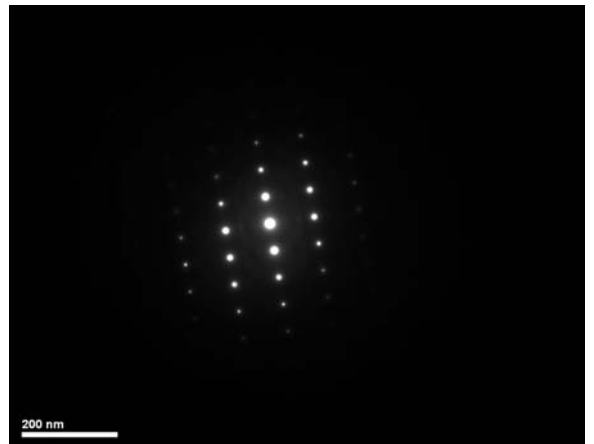
d.

Figure 3.18 TEM images and the corresponding SAD pattern for AA7050 in the Stabilized W plus 16 hours at 325˚F aging condition.
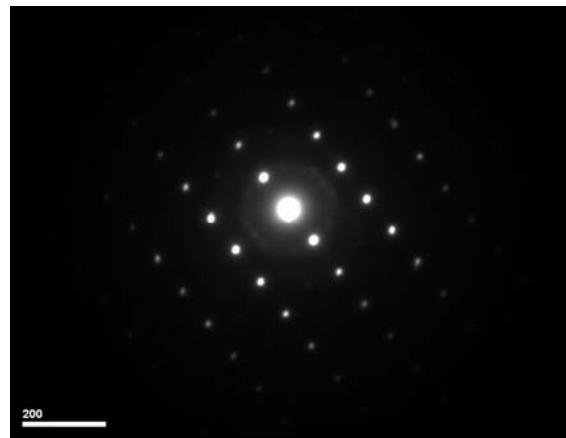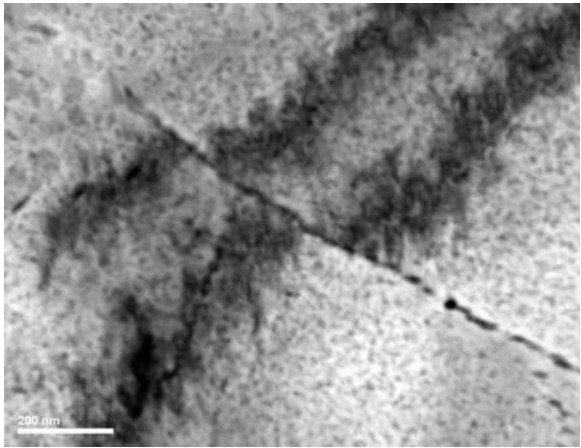
a.
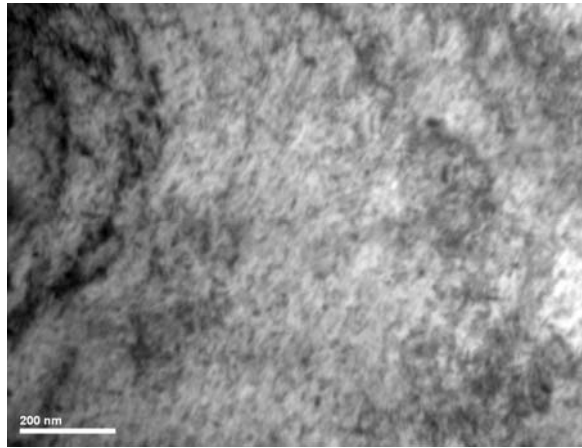
b.
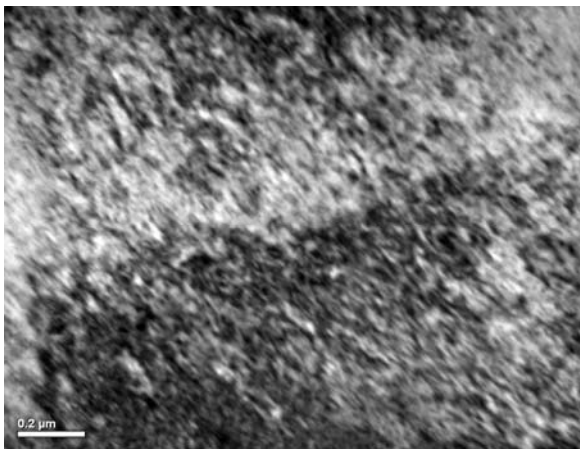
c.
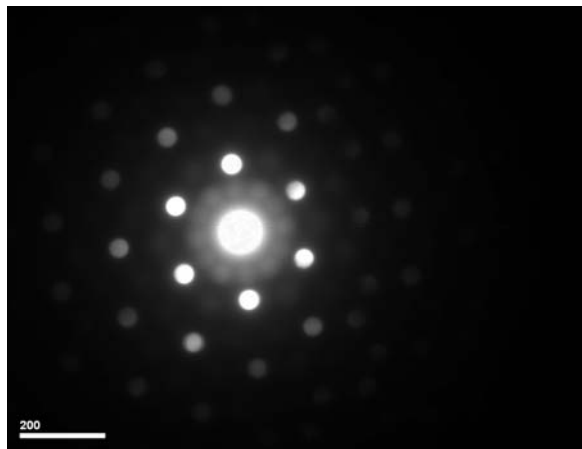
d.

Figure 3.19 TEM images and the corresponding SAD pattern for AA7050 in the Stabilized W plus 18 hours at 325˚F aging condition.
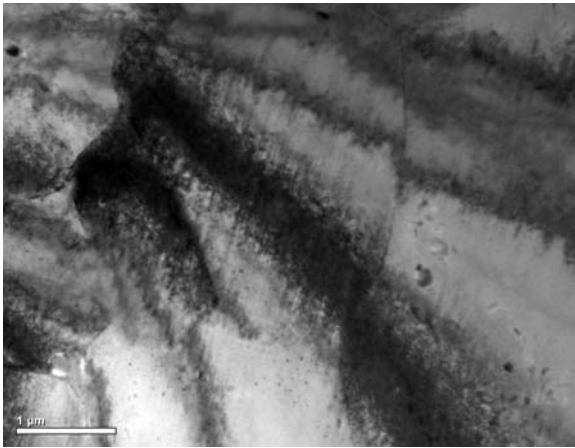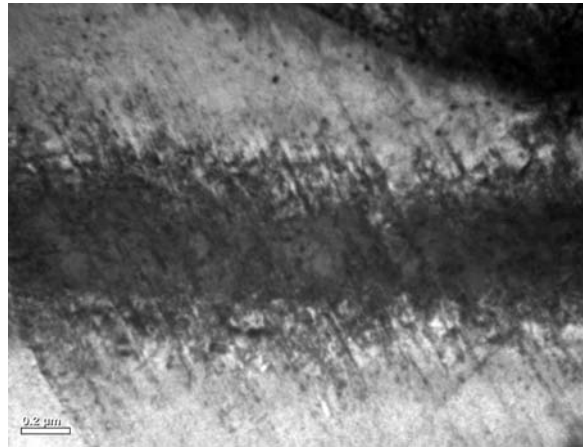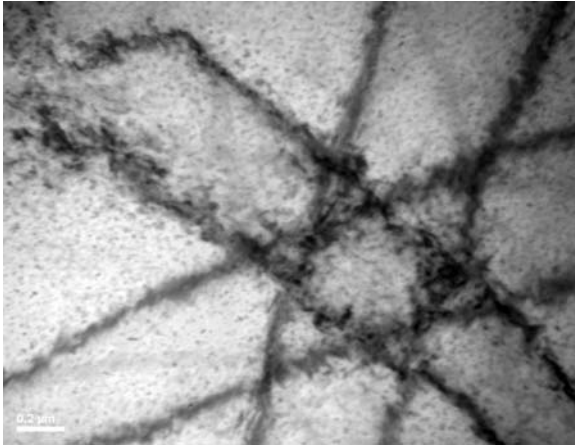
a.
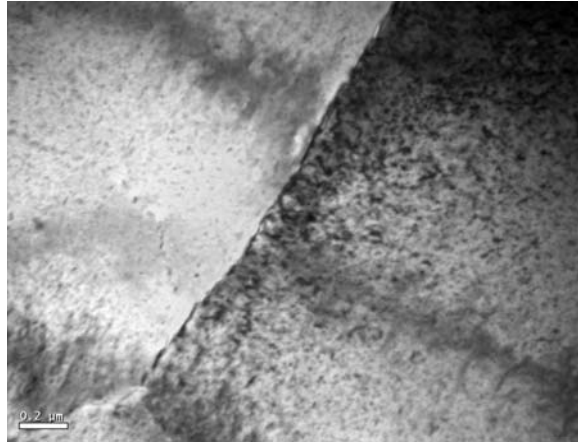
b.
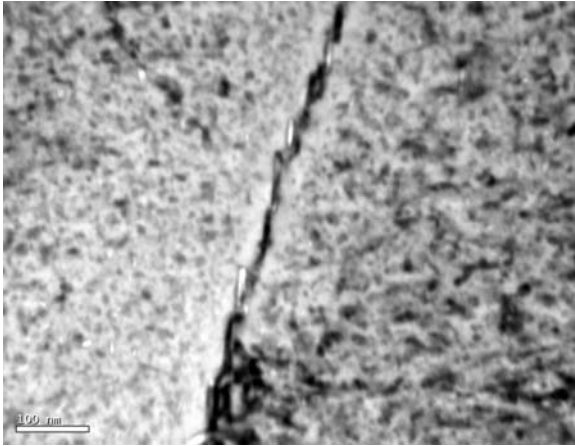
c.

d.

Figure 3.20. TEM images and the corresponding SAD pattern for AA7050 in the Stabilized W plus 27 hours at 325˚F aging condition.
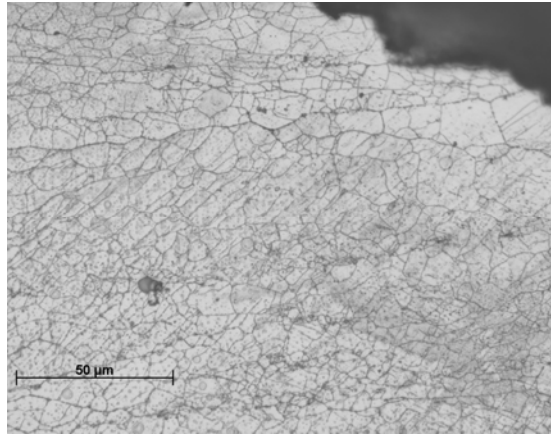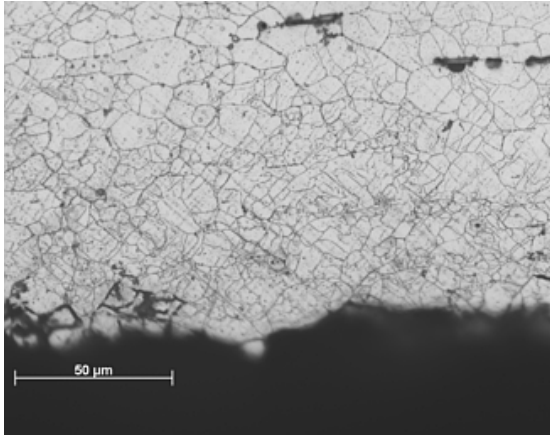
Figure 3.21. Longitudinal metallographic cross-sections of AA7050 in the Stabilized W plus 9 hours at 325˚F aging condition (Etched with Graff/Sargent's Reagent).
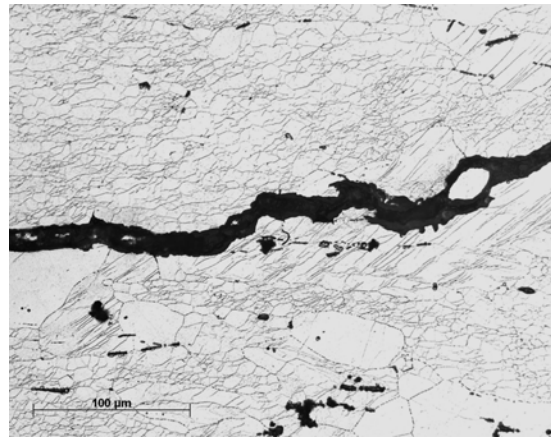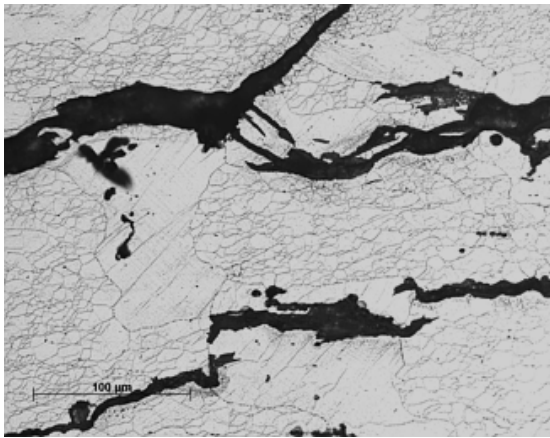
Figure 3.22. Longitudinal metallographic cross-sections of AA7050 in the Stabilized W plus 16 hours at 325˚F aging condition (Etched with Graff/Sargent's Reagent).
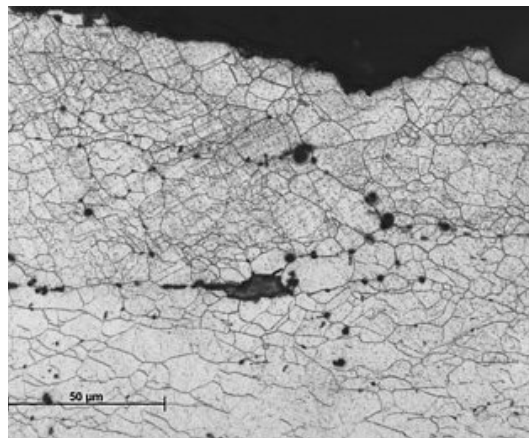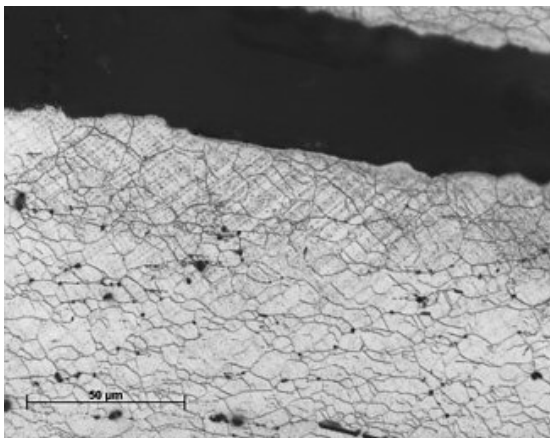
HFigure 3.23 Longitudinal metallographic cross-sections of AA7050 in the Stabilized W plus 2000 hours at 250˚F aging condition (Etched with Graff/Sargent's Reagent).
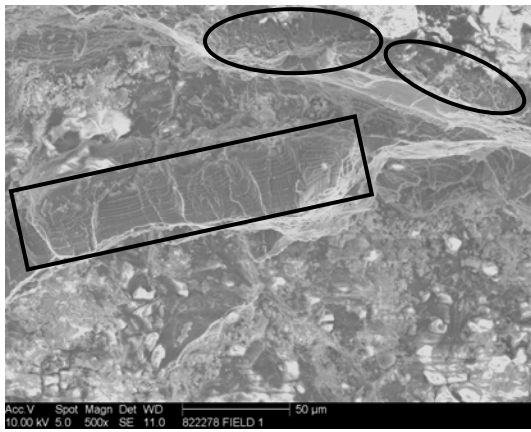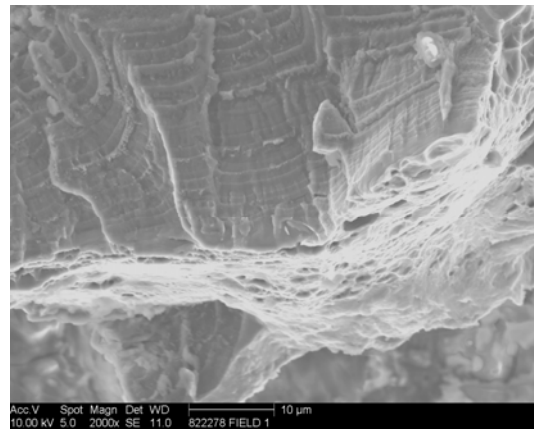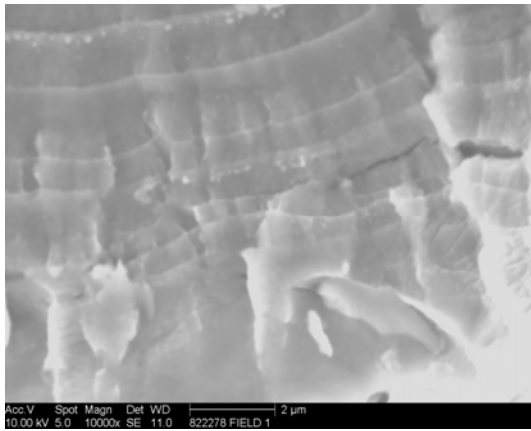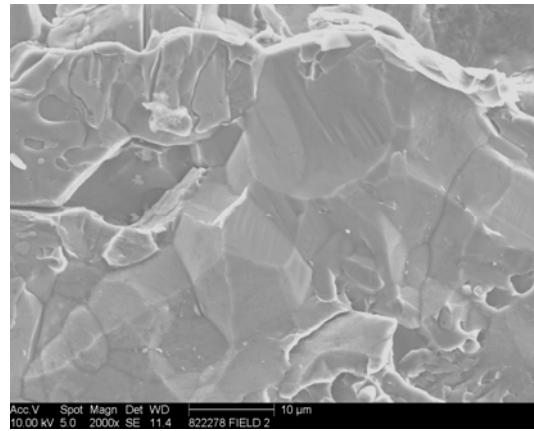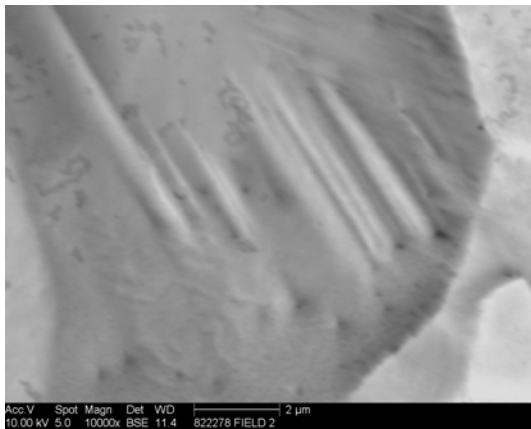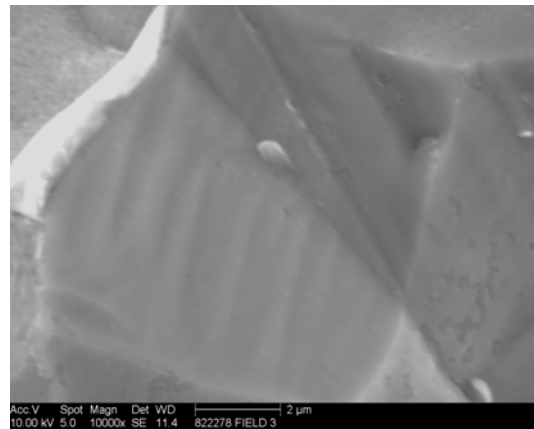
Figure 3.24. SEM fractography of EIC fracture region of DCB specimen aged 9 hours at 325˚F. In 3.24 a. the region within the rectangle is a transgranular region while the regions inside the ovals are in intergranular.

4.0   DISCUSSION

All of the specimens in this study were given the same stabilization treatment, i.e., 4 hours at 250˚F (Stabilized W) prior to the isothermal aging at 325˚F. According to Speidel's description of Regions I, II, and III of the generalized strength/SCC resistance vs. aging time behavior illustrated in Figure 1.5 the transition from Region I to Region II is marked by a minimum in SCC resistance (time to failure). The time to failure results in Table 2.2 indicate that the Stabilized W + 1 hour at 325˚F condition has the minimum SCC resistance of the materials tested in this study. This implies that the conditions of 1-9 hours of isothermal aging are in Region II where SCC resistance is increasing which is also consistent with decreasing crack growth rates measured for the conditions in this study.

According to Speidel's generalized SCC behavior in Figure 1.5, Region III appears to exhibit more rapid changes in SCC resistance with continued aging than in Region II. The crack growth rate measurements in humid air (Figure 3.1) show a distinct change in slope between 9 and 16 hours aging which presumably is associated with the transition from Region II to Region III in this generalized description. The microstructural analyses clearly show that the transition from predominantly planar slip character to predominantly homogeneous slip character is also concomitant with this transition from Region II to Region III. It is also clear that the peak strength, which occurs after approximately 6 hours of aging at 325°F, precedes the transition from planar to wavy slip and therefore does not fit the classical explanation for precipitation strengthening where the peak strength is defined by the transition from particle shearing to particle by-pass. Other studies have indicated that the peak strength in these alloy systems is associated with maximization of the number density and/or volume fraction of shearable GP zones and η' precipitates and hence the onset of coarsening.[18, 73]

An in-depth analysis of the crack growth rate, activation energy and slip character results are presented in the following discussion. The implication of these results on the mechanistic understanding of EIC of 7xxx alloys is also discussed.

4.1   CRACK GROWTH RATE AND ISOTHERMAL TRANSFORMATION

The distinct change in slope in Figure 3.1 implies a change in the rate controlling process for EIC in humid air that is quantitatively related to the progress of the isothermal phase transformation as follows:

$$\ln (CGR) = \ln A - n \operatorname{Ln} t \qquad \text{or} \qquad CGR = A/t^n \qquad [4.1]$$

where t is the isothermal aging time in seconds and CGR is the plateau crack growth rate in meters per second. It has also been observed that the crack growth rates measured in this study indicate Arrhenius-type temperature dependence as shown by the linearity of the semi-logarithmic plots of CGR vs. reciprocal temperature in Figures 3.10 and 3.11 which means that:

$$A = Ao \exp(-Q/KT) \qquad [4.2]$$

For each temperature in Figure 3.1 (40°C, 50°C, and 65°C), i.e. at constant temperature (T) and assuming that A is not a function of aging time (t) the slope is therefore given by Equation 4.3:

$$d[\ln (CGR)] / d [\ln t] = - n \qquad [4.3]$$

In Figure 3.1 the slope is ~-1 (n = ~1) for aging times ≤ 9 hours at 325°F and for aging times ≥ 16 hours at 325°F the slope is ~ -4 (n ≈ -4).

Avrami's general relationship[74] for isothermal transformation kinetics empirically relates the volume fraction transformed to time at constant temperature (i.e. isothermal aging temperature) as:

$$\zeta = V_\beta/V = 1 - \exp(-kt^n) \qquad [4.4]$$

Homogenous transformation such as the formation of GP zones is a first order rate process with n = 1. For nucleation and growth processes the situation is more complex. The exponential rate law summarized in equation 4.4 is valid for linear growth under most circumstances and for early Stages of diffusion controlled growth. The order of polymorphic changes such as η to η' depends on the whether the nucleation rate is increasing, constant or decreasing; with continually decreasing nucleation rates $3 \leq n < 4$, with constant nucleation rates $n = 4$, and with increasing nucleation rate $n > 4$. For diffusion controlled growth the exponent n depends on the size, shape and distribution of the phase and can vary from ~0.5 to ~2.5. [74]

The data clearly indicate that crack growth rates in 90%RH are inversely related to isothermal aging time to some order, n, as in equation 4.1. If Avrami's equation is rewritten as in equation 4.5 it is also clear that the progress of phase transformations are generally related to isothermal aging time to some order, n, where n depends on the type of transformation process.

$$Ln\,(1\text{-}\zeta) = \text{-}kt^n \qquad\qquad [4.5]$$

It is therefore apparent that the CGR is inversely related to Ln (1-ζ), or that is to say, to the progress of the transformation or growth processes. Hence, it is possible to infer that the changes in CGR for aging conditions of 1 to 9 hours at 325°F are related to the progress in or rate of the homogeneous formation of GP zones where n = ~1. For CGR of aging conditions ≥ 16 hours at 325°F n is ~4, which would infer that the CGR is inversely related to the progress of a polymorphic reaction, presumed to be η' to η based on general knowledge of the precipitation sequence in the Al-Mg-Zn-Cu system.

Since the microstructural analyses indicate that the transition from strain localization and predominantly planar slip (particle shearing) to homogenous slip (particle bypass) occurs between 9 and 16 hours of aging at 325°F, the association of CGR with progress of GP zone formation for shorter aging times (≤ 9 hours at 325°F) and with transformation of η' to η for longer aging times (≥ 16 hours at 325°F) would support the supposition of Speidel that EIC susceptibility is influenced by the nature of the particle-dislocation interactions. Speidel's work showed that materials with shearable precipitates were more susceptible to EIC than materials with particles that are by-passed, but the aging conditions Speidel chose to produce

the susceptible materials consisted of low temperatures for short times while those with high SCC resistance were aged at higher temperatures for relatively long times. These aging conditions would be expected to produce considerable differences in precipitate size and distribution that would represent extreme differences in slip character. By evaluating crack growth rates as a function of isothermal aging time, the results of this study show that the systematic changes in crack growth rate with aging can quantitatively be linked to the progress of the precipitation reactions that determine the slip character.

4.2   ACTIVATION ENERGY FOR CRACK GROWTH

The calculated activation energies and pre-exponentials for crack growth of all aging conditions and environmental exposure conditions in this study are summarized in Table 3.3. In this table it is apparent that there are some systematic changes in activation energy (Q) and the pre-exponential (V_0) with aging time at 325˚F. However, the systematic changes in Q and V_0 with aging are significantly affected by the addition of the NaCl drops. It is also apparent that although long aging times at 250˚F can produce strength and conductivities similar to those of shorter times at 325˚F, "overaging" at this temperature does not have the same effect on Q and V_0 as aging at 325˚F. In this section the systematic changes in the activation energy data as a function of isothermal aging time and temperature is empirically analyzed. In Section 4.3 relevant thermally activated processes are discussed.

4.2.1   Cracking in Humid Air (90%RH No NaCl)

The activation energy results for cracking in humid air are plotted as a function of aging time at 325˚F in Figure 4.1. The plot shows that for aging times of ≤ 9 hours the activation energy is fit by a log function of aging time:

$$Q_{fit} (\text{No NaCl} \leq 9 \text{ hours at } 325˚F) = 25.5 + 6.45 \log t \quad [4.6]$$

where t is aging time at 325°F in hours. Although the activation energy for crack growth increases gradually as a log function of aging time for the shorter aging times, there is a large jump in the activation energy for crack growth between 9 and 16 hours of aging at 325°F of approximately 45 kJ/mol. As overaging continues there appears to be a significant drop in activation energy for crack growth between 18 and 22 hours aging at 325°F from ~77 kJ/mol to ~52 kJ /mol. The differences in activation energy for crack growth between 16 and 18 hours and between 22 and 27 hours are negligible within the error of these types of measurements. The dramatic changes in activation energy between 9 and 16 hours and between 18 and 22 hours aging imply that there may be more than one activated process involved in the crack growth as aging progresses. If multiple processes act in series the crack velocity would be given as:

$$V_{II} = V_o \exp(-Q_{total}/RT) = [V1_o \exp(-Q_1/RT)] * [V2_o \exp(-Q_2/RT)]*\ldots[Vn_o \exp(-Q_n/RT)] \quad [4.7]$$

The number of terms in the velocity equation presumably could vary as aging progresses depending on whether there is a single process dominating the rate or two or more processes are involved. If two or more processes combine in series to control the rate the total activation energy would be the sum of the activation energies of the individual processes. If it is assumed that for aging times $\leq$ 9 hours at 325°F there is a single activated process controlling crack growth rate, the rate can be expressed as:

$$V_{II} = V1_0 \exp(-Q_1)/RT) \quad [4.8]$$

and Q_1 would be equal to Q_{fit} in equation 4.6. For aging times of 16 and 18 hours at 325°F crack growth rate, the rate can be expressed as:

$$V_{II} = V_0 \exp(-Q_{total}/RT) = [V1_0 \exp(-Q_1)/RT)] * [V2_o \exp(Q_2)/RT)] \quad [4.9]$$

with Q_2 equal to the ~45kJ/mol increase in Q that was observed between 9 and 16 hours of aging at 325°F. For 22 and 27 hours at 325°F, the lower activation energy for crack growth could be due to a decrease in Q_2 or it could indicate that an additional process with a negative activation energy ($Q_3 = -25$kJ/mol) is also influencing the crack growth at these long aging times. It should be noted that the crack growth measurements for these long aging times tend

to be less accurate than for shorter aging times because of difficulties encountered in measuring crack lengths on these more severely over-aged conditions where there is an increased tendency for pitting corrosion to mask the crack fronts.

4.2.2 Cracking in Humid Air with NaCl Drops (90%RH + 3.5% NaCl)

The activation energy results for cracking in humid air with the addition of NaCl drops are plotted as a function of aging time at 325°F in Figure 4.2. The plot shows that for aging times of ≤ 9 hours the activation energy is fit by a linear function of aging time:

$$Q_{fit} \text{ (with NaCl} \leq 9 \text{ hours at } 325°F) = 28.6 - 2.53t \quad [4.10]$$

with t in hours. In this case however, the activation energy for crack growth decreases gradually as a linear function of aging time for the shorter aging times. But similar to the case without the NaCl drops there is a large jump in the activation energy for crack growth between 9 and 16 hours of aging at 325°F of approximately 42 kJ/mol. As overaging continues there is an additional jump in the activation energy for crack growth between 18 and 22 hours aging at 325°F from ~42 kJ/mol to ~87 kJ /mol. Again the dramatic changes in activation energy between 9 and 16 hours and between 18 and 22 hours aging imply that there may be more than one activated process involved in the crack growth as aging progresses.

$$V_{II} = V_o exp(-Q_{total} /RT) = [V1_o \exp(-Q_1'/RT)] * [V2_o \exp(-Q_2/RT)] +...[Vn_o \exp(-Q_n/RT)] \quad [4.7]$$

If it is again assumed that for aging times ≤ 9 hours at 325F there is a single activated process controlling crack growth rate, Q_1' would in this case be equal to Q_{fit} in equation 4.10. For aging times of 16 and 18 hours at 325°F crack growth rate, the rate can be expressed as:

$$V_{II} = V_o \exp(-Q_{total} /RT) = V1_o' \exp(-Q_1'/RT) + V2_o \exp(-Q_2/RT) \quad [4.8]$$

with Q_2 equal to the ~42kJ/mol increase in Q that was observed between 9 and 16 hours of aging at 325°F. For 22 and 27 hours at 325°F crack growth rate the additional increase in activation energy could be due to an increase in Q_2 or it could indicate that an additional

process with an activation energy ($Q_5 = \sim43$kJ/mol) is also influencing the crack growth at these long aging times. For example the increased pitting susceptibility in these more severely overaged conditions could cause crack tip blunting that could increase the activation energy for cracking.

Alternatively, it may be that Q_1 is the same activation energy for the activated process that controls crack growth rate for the no NaCl exposure conditions of the materials with ≤ 9 hours at 325°F given in Equation 4.6 and the decrease in activation energy with the addition of NaCl for the materials with ≤ 9 hours at 325°F is related to an additional activated process (Q_4) with a negative activation energy that presumably would be associated with the effects of the Cl$^-$ ions. If so, then Q_4 would be equal to the difference between Q_1 and Q_1' which is approximately fit as:

$$Q_4 = Q_{diff} = 0.3 - 3.12t \qquad [4.9]$$
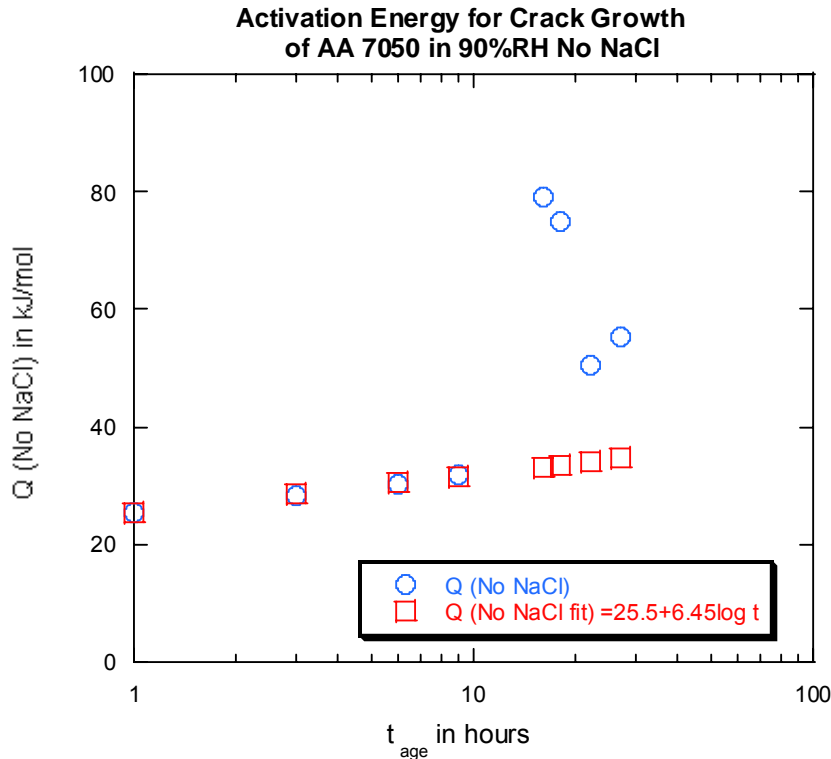
Figure 4.1 Activation energy for crack growth in 90%RH humid air as a function of aging time at 325°F.
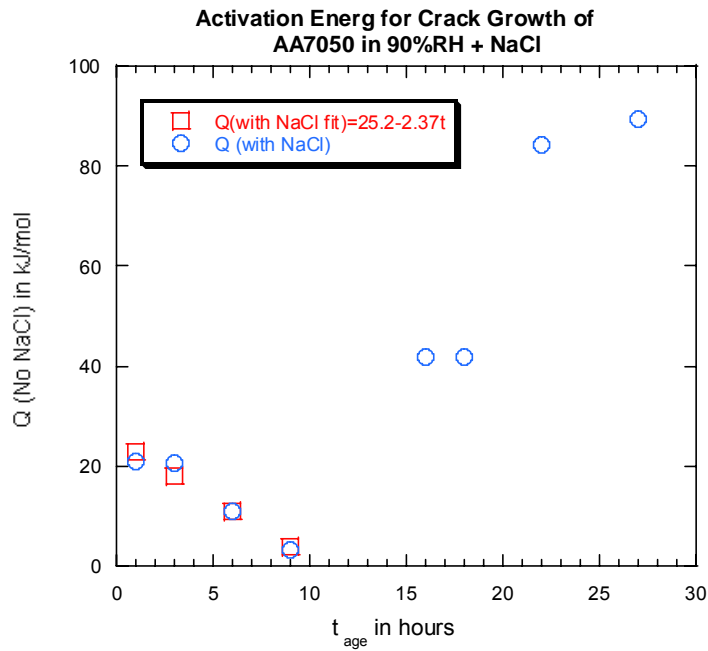
Figure 4.2 Activation energy for crack growth in 90%RH humid air with the addition of NaCl drops as a function of aging time at 325˚F.
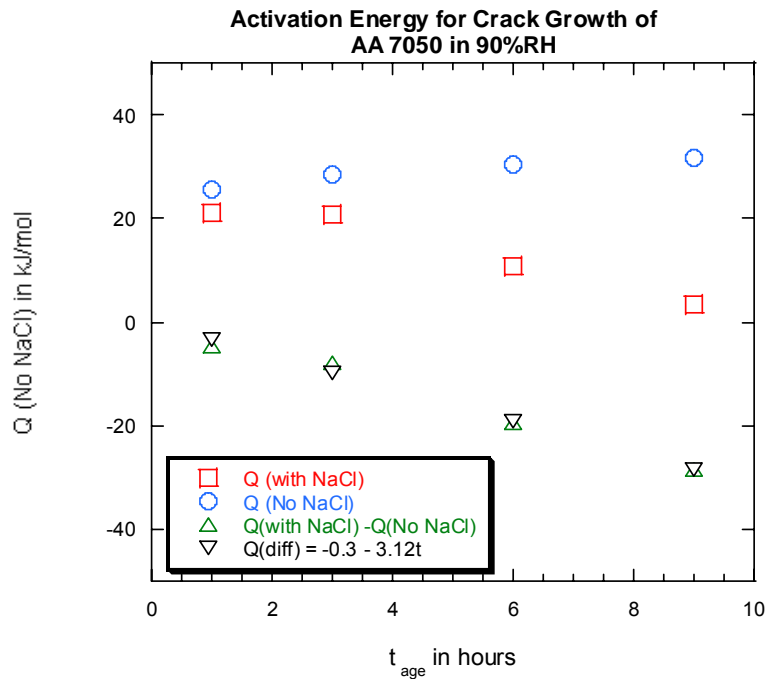
Figure 4.3 Difference in activation energy for crack growth in 90%RH humid air with and without the addition of NaCl drops as a function of aging time at 325˚F.

4.3 THERMALLY ACTIVATED PROCESSES

Crack velocity for the Stage II cracking of the DCB specimens is apparently related to temperature by the general equation 4.7:

$$V_{II} = V_o \exp(-Q_{total}/RT) = [V1_o \exp(-Q_1/RT)] + [V2_o \exp(-Q_2/RT)]* \ldots [Vn_o \exp(-Q_n/RT)] \quad [4.7]$$

where Q_{total} is the apparent activation energy for crack growth. The value of Q_{total} appears to vary in significant ways depending on both the isothermal aging condition of the material and the presence of chloride in the environment. Correlation of the systematic variations in the effective activation energy with systematic changes in crack growth rates would help to identify the rate controlling process or processes involved. It is also apparent that the large change in activation energy between 9 and 16 hours of aging at 325°F indicates a change in the rate limiting process that is controlling cracking and that, based on the microstructural characterizations, this change is associated with a change in the slip mode or slip character. If the activated process or processes associated with the various aging conditions and important environmental aspects can be identified a more comprehensive explanation of the EIC mechanism will emerge. In the following sections various potentially relevant thermally activated processes and their possible contribution to the cracking process are discussed.

4.3.1 Anodic Dissolution and Proton Discharge

Using mixed potential theory and assuming that the over-potentials at the corrosion potential are sufficiently large that the high field approximation of the Butler-Volmer expression can be used, the corrosion current is given in equation 4.10:

$$I_{corr} = (I_{0, M}) \exp[(\alpha)F(E_{corr} - E^o_{M/Mn+})/RT] = (I_{0, C}) \exp[\beta F(E_{corr} - E^o_C)/RT] \quad [4.10]$$

where I_{corr} is the corrosion current (rate), $I_{0, M}$ and $I_{0, C}$ are the equilibrium exchange currents for the anodic metal dissolution (electronation) and cathodic (de-electronation) reactions. $E_{M/Mn+}$ and E_C are the standard electrode potentials and α and β are the respective transfer coefficients and E_{corr} is the corrosion potential. The high field approximation is a reasonable

assumption for over potentials greater than ~0.100V which is the case for aluminum corrosion potentials under mixed potential control. According to equation 4.16 the rate of anodic dissolution is thereby dependent on the exchange currents, Tafel slopes and equilibrium potentials of the metal dissolution and de-electronation reactions with an Arrhenius type dependence on the temperature.

The repassivation potential was shown to correlate with the time to failure of these materials (Figure 1.17).[65] The repassivation potential (E_{rp}) is the equilibrium potential after some corrosion has occurred on the surface. If the E_{rp} values in Table 1.3 are substituted for E_{corr} in equation 4.10, activation energies for the anodic dissolution reaction can be estimated. Representative calculations of this type are given in Table 4.1 for the anodic dissolution reaction in equation 1.13.

$$Al + 3H_2O \leftrightarrow Al_2O_3 + 6H^+ + 6e^- \quad [1.13]$$
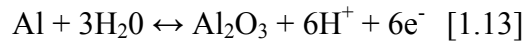
The activation energy estimates are of the form $Q = b + m\log t$ similar to Q_1 or Q_{fit} (Equation 4.6 in section 4.2.1). Values of α for curves in Figure 1.17 are estimated to be in the 0.3 to 0.5 range. The activation energy estimates are calculated first with α fixed at 0.35 and also with α varying slightly to demonstrate an improved fit to Equation 4.6. These estimates of activation energy appear to be consistent with those calculated for crack growth of specimens aged 1 to 9 hours at 325°F as illustrated in Figure 4.4. This would imply that the activation energy for crack growth of the shorter aging times (≤9hours at 325°F) are associated with those for the rate of H^+ and/or Al_2O_3 production in equation 1.13. That is to say the rate limiting step in the cracking process of these materials (≤9hours at 325°F) in 90%RH (no NaCl) appears to be the reaction of the aluminum with water to produce H^+ (proton discharge) and Al_2O_3. It is at least intuitively possible for these relatively susceptible tempers (high crack growth rates) in a moist air environment (less aggressive environment than with Cl⁻) that the rate limiting step would be the rate at which the hydrogen is made available.

The exchange currents also have Arrhenius type dependence on the temperature:

$I_o = Fc_D \, kT/h \, \exp(-\Delta G^o/RT) \, \exp[(1-\beta)F\Delta\phi_e] = Fc_A \, kT/h \, \exp(-\Delta G^o/RT) \, \exp(\beta F\Delta\phi_e)$

where $\Delta\phi_e$ is the potential change at the electrode interface. Exchange currents reflect the kinetic properties of the particular interfacial systems and can vary by many orders of magnitude from one electrode material to another. The exchange current density for the hydrogen-evolution reaction provides a relative measure of the reaction rate on a metal electrode.[46,47] Aluminum is a relatively poor catalyst for the hydrogen evolution reaction with an exchange current density on the order of 10^{-9} A/cm^2. For 7xxx series alloys the electronic nature of the various alloying elements in solid solution may significantly influence the exchange current density for the hydrogen evolution reaction. Zinc is a poorer catalyst than aluminum with an exchange current density on the order of 10^{-10} A/cm^2, which is consistent with the lack of unpaired d band electrons in zinc. Copper on the other hand is a relatively good catalyst for the hydrogen evolution reaction with an exchange current density on the order of 10^{-6} A/cm^2. Therefore, zinc in solid solution could enhance the adsorption of hydrogen while copper in solid solution could significantly reduce the hydrogen absorption of the alloys.

Table 4.1 Activation energies calculated for Equation 1.13 from E^o and E_{rp} from previous study.[65]

E_0 (V vs SCE)*	Aging Time at 325°F	E_{rp} (V vs SCE)	$\Delta E = E_{rp} - E^o$ (V)	$Q = \Delta E\alpha F$ (kJ/mol) $\alpha = 0.35$	$Q = \Delta E\alpha F$ (kJ/mol)	
					α	Q_{adj}
-1.31-0.059pH	1h	-0.845	0.672	22.6	0.39	25.4
	6h	-0.779	0.738	24.9	0.42	29.7
	18h	-0.742	0.775	26.2	0.44	32.6
	27h	-0.735	0.782	26.4	0.46	34.7
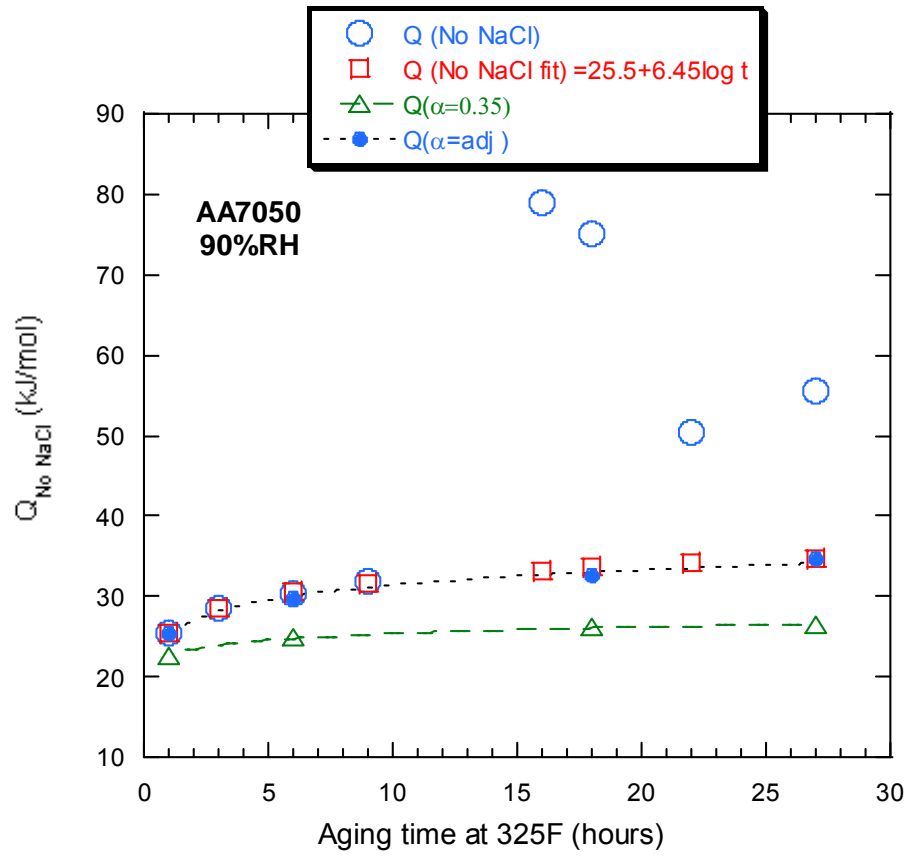
Figure 4.4 Activation energies for Equation 1.13 are plotted with those for crack growth in 90%RH (no NaCl).

4.3.2 Hydrogen Adsorption Kinetics

The kinetics of the hydrogen adsorption are influenced by the relationship between the concentration of hydrogen atoms formed as a result of electron transfer (c) and the coverage (θ) of the surface by hydrogen atoms, i.e. by the actual form of the adsorption isotherm. Various relationships have been derived to describe adsorption on metal surfaces in contact with solutions but the Langmuir and Temkin type adsorption isotherms are most suitable for adsorption of intermediate species in electrode processes.[46]

The Langmuir adsorption isotherm can be written as:

$$\theta/(1-\theta) = \exp\left[-\Delta G^o_{ads}/(RT)\right]c \qquad [4.11]$$

The Langmuir isotherm is valid if:

1. adsorption occurs on discrete sites, i.e. adsorbed species are immobile on the surface
2. the surface is not heterogeneous and there is no lateral interaction, i.e. the adsorption energy is independent of the coverage (θ)
3. equilibrium is reached between the surface and the bulk phase up to the formation of a monolayer (up to $\theta = 1$)

The Temkin adsorption isotherm takes into account that real surfaces are usually inhomogeneous, i.e. there is interaction between adsorbed species and therefore the adsorption energy depends on the coverage. That is to say, Temkin assumed that a Langmuir isotherm applied to each of the sites of differing ΔG^o_{ads} on a heterogeneous surface and the total coverage was the sum of the various sites:

$$\theta = \sum \theta_j \, L_i/L_0 \qquad [4.12]$$

Where L_i is the number of sites of type j and L_0 is the total number of sites of all types per unit area. This type of treatment for heterogeneous surfaces could be useful for correlating systematic changes in activation energy with systematic changes in the matrix and/or particle compositions with aging time. Although it can be difficult to determine the total coverage of

a surface with hydrogen it can be determined by carefully performed electrochemical transient or sweep techniques.[46]

Vehoff[75]developed an adsorption controlled model for Stage II crack propagation (Equation 4.13) based on dissociative adsorption of hydrogen gas:

$$v_{II} = (da/dt)_{II} = [(1- \theta)/\theta] [s_o \, A_a \, Z \, exp \, (-E_a/RT)] \, x_o \qquad [4.13]$$

where s_o is the sticking probability of a hydrogen gas molecule, A_a is the area of an adsorption site, Z is the collision rate, x_o is the incremental crack advance distance, and E_a is the activation energy for adsorption. The activation energy for adsorption of hydrogen is the heat of adsorption. For gas phase adsorption of atomic hydrogen the heat of adsorption is approximately equal to the M-H bond energy. Although it is not necessarily reasonable to assume that the gas phase heat of adsorption is applicable to a situation in which the metal is an electrode in an electrolytic solution, it is likely that the relative order of aqueous adsorption energies for various metals is consistent with the gas phase adsorption energies.[46]

The recombination of adsorbed hydrogen, can occur by two possible types of paths. It can occur without charge transfer by chemical desorption (a.k.a. catalytic recombination) or by means of an electrodic desorption step such as:

Chemical Desorption: $\qquad 2MH(ads) \rightarrow 2M + H_2 (g) \qquad$ [1.8]

Electrodic Desorption: $\qquad MH + H_3O^+ + M(e^-) \rightarrow 2M + H_2O + H_2 (g) \quad$ [1.9]
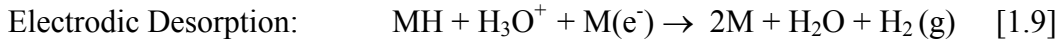
If the actual reaction path on a particular metal electrode involves a fast proton discharge reaction step followed by a slow (rate-determining) desorption step, adsorbed hydrogen atoms will accumulate on the metal surface and a high surface coverage of adsorbed hydrogen atoms will exist at steady state conditions. On the other hand, if proton discharge is slow then the formation of adsorbed hydrogen is difficult and the hydrogen atoms that do arrive on the surface rapidly form hydrogen gas so the surface coverage remains low. The rate of an electrodic desorption step is dependent on the surface concentration of adsorbed hydrogen and the concentration of protons:

$$v_{ED} = k\theta c_{H+} exp[(\beta F\Delta\phi)/RT] \qquad [4.14]$$

93

Therefore, at low concentrations of either adsorbed hydrogen or protons the rate of electrodic desorption approaches zero.[46]

4.3.3 Mass Transport Kinetics

In the introductory discussion of anodic dissolution mechanisms in section 1.1.2.1 it was shown that the Mass Transport Kinetics (MTK) model[22] predicts that crack velocity may be limited by the rate of transport of a species such as chloride to the crack tip. The expression developed was given in Equation 1.18.

$$V = \{D[-zFA(dC/dy) - zFA(zF/RT)C(d\phi dy)]\}/2nq_x \quad [1.18]$$

The first term is a diffusion term and the second term is an electro-migration term. The crack growth velocity is proportional to the concentration (C) of the species (chloride). The diffusivity (D) has an exponential dependence on reciprocal temperature (1/T) and is the dominant temperature dependence. For an established crack where the tip is saturated with $AlCl_3$ the migration term is dominant and the diffusion term can be neglected.[64] The addition of NaCl to the exposure catalyzes the anodic dissolution and proton discharge. Therefore, as the crack growth rates decrease with aging from 1 to 9 hours the electro-migration term becomes important. The electro-migration term is not thermally activated. The decrease in activation energy for crack growth from 1 to 9 hours with NaCl may therefore be related to a transition from proton discharge control to electro-migration control of the cracking process.

4.3.4 Hydrogen Transport

4.3.4.1 Diffusion Transport of Hydrogen
Fickian diffusion of interstitial hydrogen also follows an Arrhenius rate law as described in Equation 4.14:

$$D = D_o \exp(-Q/RT) \quad [4.15]$$

Where D is the diffusivity and D_o is the frequency factor. The thermal desorption tests conducted by G. Young[2] on 99.999% aluminum indicated that the activation energy for diffusion of hydrogen in aluminum is ~16 kJ/mol with a frequency factor of 1.8×10^{-8} m^2/s. Similar tests on under aged and peak aged AA7050 also indicated that the activation energy for interstitial diffusion of hydrogen was ~16kJ/mol but with frequency factors of 5.5×10^{-9} and 2.2×10^{-9}, respectively. For the over aged condition however, the activation energy for interstitial diffusion of hydrogen increased to ~33 kJ/mol. By comparing thermal desorption spectra from annealed and cold worked 99.999% aluminum the desorption energy for hydrogen "trapped" at dislocations was estimated to be 43.5 ± 17.5kJ/mol.[2] This value for the desorption energy for hydrogen is consistent with the ~45kJ/mol increase in activation energy for crack growth between the 9 and 16 hour aging conditions in this study. The consistency of the dislocation desorption energy and the change in activation energy for crack growth along with the coincident change in slip character imply that for longer aging times the rate determining step in the cracking process is likely related to dislocation transport of hydrogen.

By comparing thermal desorption spectra from 99.999% aluminum annealed at different temperatures, the desorption energy for hydrogen "trapped" at vacancies was estimated by Young[2] to be 84.8 ± 32.2kJ/mol. This value for the desorption energy for hydrogen from vacancies appears to be consistent with the ~85kJ/mol activation energy for crack growth for the 22 and 27 hour aging conditions in 90%RH with NaCl additions in this study.

4.3.4.2 Dislocation Transport of Hydrogen

Interaction of dislocations with solute hydrogen atoms results in a region of increased hydrogen concentration in the vicinity of the dislocation line referred to as a Cottrell atmosphere.[74] For an edge dislocation the distribution of solute atoms in a Cottrell atmosphere is given by the relationship in Equation 4.16:

$$C = C_o \exp \left(-\beta \sin \theta / rkT \right) \qquad [4.16]$$

where is the C_o concentration at $r = \infty$, θ and r are the coordinates for locations relative to the dislocation core and β is the hydrostatic stress component of the internal stress field at the dislocation given by Equation 4.17:

$$\beta = [(\mu b_e)/(3\pi)][(1 + v)/1\text{-}v] \qquad [4.17]$$

The implication of Equation 4.16 is that compression on one side of the dislocation leads to depletion of solute atoms and accumulation of vacancies and tension on the other side results in accumulation of solute and depletion of vacancies. At small stresses and/or low temperatures the dislocation can move only by dragging the solute atmosphere so that dislocation motion is controlled by diffusion of the solute atoms.

When a small constant force (F) is applied the motion of the diffusing defect is biased and the drift velocity (v_D) is related to the mobility (D/kT) by the Einstein mobility relation (Equation 4.17):

$$v_D = (D/kT)\ F \qquad [4.18]$$

The force need not be a mechanical force. It can be a general thermodynamic force such as a chemical potential difference or an electric field.[74]

At higher applied stresses or temperatures (i.e higher velocities) the dislocation motion is limited by solute drag. The velocity is expressed in terms of the creep velocity (v):

$$v = [(F/L)\ DkT]\ /\ c_o\ \beta^2 \ln(R/r) \qquad [4.19]$$

where R is the distance between dislocations r, is the effective radius of the Cottrell atmosphere, F/L is the unit force on the dislocation line.[74]

For both the drift velocity and the solute drag velocity the activation energy associated with the dislocation motion is that for bulk diffusion of the solute.[74] Therefore all of the activation energy information in the previous section for diffusion of hydrogen would also apply to solute (interstitial hydrogen) drift and drag motion.

4.4   IMPLICATIONS ON CRACK GROWTH MECHANISM

For the more EIC susceptible conditions, aging times $\leq$ 9 hours at 325˚F, slip occurs by strain localization in narrow bands of predominantly planar slip. The localization of the plastic deformation may facilitate the mobility of the hydrogen enriched dislocations within the plastic zone at the crack tip and results in stress concentrations and dislocation pile-ups at the grain boundaries. For these conditions the rate of hydrogen transport to the crack tip would be fast relative to the rate of the surface (anodic dissolution, proton discharge, and hydrogen recombination) and mass transport (diffusion and electro-migration of ionic species) processes and crack growth rates would likely be controlled by the kinetics of the surface and/or mass transport processes.

The transition from strain localization and predominantly planar slip to predominantly homogeneous slip between 9 and 16 hours of aging at 325˚F reduces the mobility of dislocations and cracking becomes hydrogen transport limited. There appear to be additional changes in the activation energy between 18 and 22 hours of aging at 325˚F but the accuracy and completeness of the data for these tempers was hampered due to the extremely slow crack rates and enhanced pitting corrosion in these tempers. Changes in activation energy for these over-aged conditions are likely due to effects of continued coarsening of precipitates and enhanced pitting corrosion on the relevant processes but it is not apparent how from the information presently available. Enhanced pitting corrosion susceptibility could contribute to the increase in activation energy between 18 and 22 hours of aging at 325˚F at 90%RH with NaCl due to crack tip blunting. Without NaCl, the decrease in activation energy between 18 and 22 hours of aging at 325˚F could possibly be related to enhanced dislocation mobility due to increased spacing of the precipitates.

5.0   CONCLUSIONS

■ Although peak strength is observed at ~6 hours of isothermal aging at 325˚F, slip occurs primarily within narrow glide bands of predominantly planar slip for specimens with 1, 3, 6, and 9 hours of isothermal aging at 325˚F.

   • Peak strength is presumably related to maximum volume fraction of GP zones while transition from planar slip to wavy slip is likely associated with coarsening of η' or η precipitates to a critical size.

   • For the shorter aging times strong obstacles (non shearable) are small and the glide dislocations can likely overcome them by short distance of cross-glide (cross-slip) or local climb between sets of parallel glide plane within the narrow glide bands.

■ The change in slope of Ln CGR vs. Ln t_{age} between 9 and 16 hours of aging at 325˚F appears to correspond with a change in the predominant slip mechanism. These changes are also associated with a large shift in activation energy for crack growth.

■ Susceptibility of AA 7050 aged at 250˚F for long times still exhibit strain localization and predominantly planar slip in glide bands and are therefore more susceptible to EIC than materials aged at 325˚F to the same apparent electrical conductivity and yield strength.

■ In 90%RH without NaCl the slopes of Ln CGR vs Ln t_{age} imply a change from dependence on progression of homogenous precipitation (GP zone formation) at shorter aging times to progress of a polymorphic reaction (presumed to be η' to η) for longer aging times.

- Activation Energy (Q)
  - Region II: Q increases slightly with increasing t_{age} from 1 hour to 9 hours due to enhanced repassivation kinetics and/or proton discharge limitations (Q1)
  - Region IIIa: Large increase in Q between t_{age} = 9 hours and t_{age} = 16 hours due to transition from strain localization and predominantly planar slip to homogeneous wavy slip, proton discharge and diffusion and/or dislocation transport limited (Q1 + Q2)
  - Region IIIb: Decrease in Q between t_{age} = 18 hours and t_{age} = 22 hours (possibly related to enhanced dislocation mobility due to increasing spacing of precipitates with coarsening)

- In 90%RH with NaCl the Ln CGR vs Ln t_{age} plot is influenced by a thermally activated chemical or electrochemical process that is a f{t_{age})
  - Activation Energy (Q)
    - Region II: Q decreases slightly with increasing t_{age} from 1 to 9 hours aging at 325˚F (apparently related to a transition from proton discharge controlled to electro-migration or adsorption controlled cracking (Q1 + Q3)
    - Region IIIa: Large increase in Q between t_{age} = 9 hours and t_{age} = 16 hours due to transition from strain localization and predominantly planar slip to homogeneous wavy slip, diffusion and/or dislocation transport limited (Q2)
    - Region IIIb: Increase in Q between t_{age} = 18 hours and t_{age} = 22 hours, possibly crack tip blunting or additional H transport limitations (Q5)

99

BIBLIOGRAPHY

1.   L.M. Young, "Microstructural Dependence of Aqueous-Environment Assisted Crack Growth and Hydrogen Uptake in AA7050", Ph.D. Dissertation, University of Virginia, Charlottesville, VA, August 1999.

2.   G.A. Young, Jr., "Hydrogen Assisted Cracking of an Al-Zn-Mg (Cu) Alloy", Ph.D. Dissertation, University of Virginia, Charlottesville, VA, August 1999.

3.   K.R. Cooper, "Chemistry and Electrochemistry of Environment Assisted Cracking of an Al-Zn-Mg (Cu) Alloy", Ph.D. Dissertation, University of Virginia, Charlottesville, VA, August 1999.

4.   J.M. Howe, "Update on Alcoa 7050 Microstructural Work at UVa" by Jim M. Howe, February 22, 1999.

5.   D. Williams, Unpublished Results, 1998.

6.   M.O. Speidel, "Interaction of Dislocations with Precipitates in High Strength Aluminum Alloys and Susceptibility to Stress Corrosion Cracking", Proc. Conf. Fundamental Aspects of SCC, Ohio State Univ. 1969, pp. 561-580.

7.   F.S. Lin and E.A. Starke, "The Effect of Copper Content and Degree of Recrystallization on the Fatigue Resistance of 7xxx type Aluminum Alloys; I. Low Cycle Corrosion Fatigue", Materials Science and Engineering, Vol. 39, No. 1, July, 1979, pp. 27-42.

8.   E.A. Starke and J.C. Williams, "Microstructure and the Fracture Mechanics of Fatigue Crack Propagation", *Fracture Mechanics: Perspectives and Directions*, ASTM STP 1020, edited by R.P. Wei and R.P. Gangloff, Philadelphia, PA,1989, pp. 184-205.

9.   B. Sarkar, M. Marek, and E. Starke, Jr., "The Effect of Copper Content and Heat Treatment on the Stress Corrosion Characteristics of Al-6Zn-2Mg-X Cu Alloys," Metall. Trans. 12A, 1981, pp. 1939-1943

10.   R.D. Carter, E.W. Lee, E.A. Starke, Jr., and C.J. Beevers, "The Effect of Microstructure and Environment on Fatigue Crack Closure of 7475 Aluminum Alloy", Met. Trans. A, Vol. 15A, March 1984, pp. 555-563.

11.   P.J. Ferreira, I.M. Robertson, and H.K. Birnbaum, "Hydrogen Effects on the Interaction Between Dislocations", Acta. Mater., Vol. 46, No. 5, pp1749-1757, 1998.

12.   J. Albrecht, A.W. Thompson, and I.M. Bernstein, "The Role of Microstructure in Hydrogen Assisted Fracture of 7075 Aluminum", Met. Trans. A, Vol. 10A, Nov. 1979, pp. 1759-1766.

13.   J. Albrecht, I.M. Bernstein, and A.W. Thompson, "Evidence for Dislocation Transport of Hydrogen in Aluminum", Met. Trans. A, Vol. 13A, May 1982, pp. 811-820.

14.   D.A. Hardwick, A.W. Thompson, and I.M. Bernstein, "Effect of Copper Content and Microstructure on the Hydrogen Embrittlement of Al-6Zn-2Mg Alloys", Met. Trans. A, Vol. 14A, Dec. 1983, pp. 2517-2526.

15.   T.C. Lee, I.M. Robertson, and H.K. Birnbaum, "An In-situ Transmission Electron Microscopy Deformation Study of Slip Transfer Mechanisms in Metals", Met Trans. A, Vol. 21A, Sept. 1990, pp. 2437-2447.

16.   G. Lu, et.al. "Hydrogen Enhanced Local Plasticity in Aluminum: An Ab Initio Study", 2002.

17.   H.K. Birnbaum, "Mechanisms of Hydrogen-Related Fracture of Metals", EICM Proceedings, pp. 21-29.

18.   A.J. Jacobs, "The Role of Dislocations in the Stress Corrosion Cracking of 7075 Aluminum Alloy", Trans. of the ASM, Vol. 58, 1965.

19.   W. Gruhl, "The Stress Corrosion Behavior of High Strength AlZnMg Alloys," Aluminum Vol. 54, 1978, pp. 323-325.

20.   W. Gruhl, "The Stress Corrosion Cracking of High Strength Aluminum Alloys," Zeit. Metallkunde, Vol. 75, 1984, pp. 819-826.

21.   F. Bovard and J. Kearns, "Status of Corrosion Testing of New High Strength 7xx Casting Alloys," Alcoa Report No. 471-LC-11, June 21, 1996.

22.   M.O. Speidel and M.V. Hyatt, "Stress-Corrosion Cracking of High-Strength Aluminum Alloys", *in Advances in Corrosion Science and Technology*, Vol. 2, edited by M.G. Fontana and R.W. Staehle, 1972.

23.   P.N. Adler, R.DeIasi, and G. Geschwind, "Influence of Microstructure on the Mechanical Properties and Stress Corrosion Susceptibility of 7075 Aluminum Alloy," Met. Trans. Vol 3, December 1972, pp. 3191-3200.

24. I.J. Polmear, "The Properties of Commercial Al-Zn-Mg Alloys," J. Australian Inst. Metals, Vol. 89, 1960, p. 193.

25. A.J. Sedriks, P.W. Slattery, and E.N. Pugh, "Precipitate Free Zones and Stress Corrosion Cracking in a Ternary Al-Zn-Mg Alloy," Trans. ASM, Vol. 62, 1969, p. 238.

26. I. T. Taylor and R.L. Edgar, "A Study of Stress-Corrosion in Al-Zn-Mg Alloys, Met.Trans., Vol. 2. March 1971, pp. 833-839.

27. S. Maitra and G.C. English, Met. Trans., Vol. 12A, 1981, pp. 535-541.

28. G. Thomas and J. Nutting, "The Aging Characteristics of Aluminum Alloys – Electron Microscopic Studies of Alloys Based on the Aluminum-Zinc-Magnesium System," J. Inst. of Metals, Vol. 88, 1959, p.81.

29. A.J. McEvily Jr., et.al., "Effect of Thermal-Mechanical Processing on the Fatigue and Stress Corrosion Properties of an Al-Zn-Mg Alloy", Trans. of ASM, Vol. 60, 1967, pp. 661-671.

30. L.M. Angers and S. Lee, "Characterization of the Response of 7150 and C151 Plate", Alcoa Internal Report No. 56-AH444, May 1, 1990.

31. A.J. Deardo, PhD Thesis, Carnegie Mellon University, 1969.

32. M. Tanaka, R. Dif, and T. Warner, "Chemical Composition Profiles Across Grain Boundaries in T6, T79 and T76 Tempered AA7449 Alloy," 2003.

33. I.J. Polmear, "Light Alloys: Metallurgy of the Light Metals", 3rd edition, 1995.

34. L.F. Mondolfo, "Aluminum Alloys: Structure and Properties," Butterworths, London 1979, pp. 577-587 and 652-654.

35. J. M. Howe, "Update on Alcoa 7050 Microstructural Work at UVa by Jim M. Howe, February 22, 1999.

36. G. Thomas, et.al., JIMMA 27, p. 429.

37. A. Bigot et al., "Tomographic Atom Probe Study of Age Hardening Precipitation in Industrial AlZnMgCu (7050) Alloy," Fifth Int. Conf. On Aluminum Alloys, Vols. 217-222, 1996, pp. 695-700.

38. D.O. Sprowls and R.H. Brown, "Stress Corrosion Mechanisms for Aluminum Alloys," Int. Conf. on Fundamental Aspects of Stress Corrosion Cracking, Ohio State University September 11-15, 1969, pp. 466-512.

39. B.W. Lifka, D.O. Sprowls, and R.A. Kelsey, "Investigation of Smooth Specimen SCC Test Procedures. Variations in Environment, Specimen Size, Stressing Frame

and Stress State", Prepared for George C. Marshall Space Flight Center Contract No. NAS 8-21487, July, 1969.

40. Luetjering and A. Gysler, "Mechanical Behavior of Aluminum Alloys" in *Aluminum Alloys – Physical and Mechanical Properties*, edited by E.A. Starke Jr. and T.H. Sanders, E.M.A.S., 1986, pp. 1547-1573.

41. A.R. Troiano, Trans., ASM, Vol. 52, 1960, pp. 54-80.

42. T. Magnin, "Recent Advances in the Environment Sensitive Fracture Mechanisms of Aluminum Alloys", Mat. Sci. Forum, Vols. 217-222, 1996, pp. 83-94.

43. R.J. Selines and R.M. Pelloux, "Effect of Cyclic Stress Wave Form on Corrosion Fatigue Crack Propagation in Al-Zn-Mg Alloys," Met. Trans. Vol. 3, Sept. 1972, pp. 2525-2531.

44. M. Taheri, J. Albrecht, I.M. Berstein, and A.W. Thompson, "Strain Rate Effects on Hydrogen Embrittlement of 7075 Aluminum," Scripta Met., Vol. 13, 1979, pp. 871-875.

45. J.K. Tien, S. V. Nair, and R.R. Jensen, "Dislocation Sweeping of Hydrogen and Hydrogen Embrittlement," *Hydrogen Effects in Metals*, Proc. of the 3rd International Conference on Effect of Hydrogen on Behavior of Materials, ed. by I.M. Bernstein and A.W. Thompson, AIME, 1980, pp. 37-53.

46. J.O. Bockris and A.K. Reddy, Modern Electrochemistry, Vol.2, 1970.

47. H. Kita, "Periodic Variation of Exchange Current Density of Hydrogen Electrode Reaction with Atomic Number and Reaction Mechanism," J. Electrochem. Soc., Vol. 113, No. 11, pp. 1095-1111, 1966.

48. N. Pentland, J.O. Bockris, and E. Sheldon, "Hydrogen Evolution Reaction on Copper, Gold, Molybdenum, Palladium, Rhodium, and Iron; Mechanism and Measurement Technique under High Purity Conditions," J. Electrochem. Soc., Vol. 104, p. 182, 1957.

49. W. Eichenauer et al., "Die Loslicheit von Wasserstoff in festim und flussigem Aluminum", Z. Metallkde, Vol. 52 (10), p. 682-684, 1961.

50. S. Matsuo, and T. Hirata, "Diffusion of Hydrogen in Aluminum", J. Japan Inst. Metals, Vol. 31, pp. 590-593, 1967.

51. M. Ichimura and M. Imabayashi, "Measurement of the Diffusion Coefficient and Solubility of Hydrogen in Solid Aluminum", J. Japan Inst. Metals, Vol. 43, pp. 876-883, 1979.

52. K. Papp and E. Kovacs-Csetenyi, "Diffusion of Hydrogen in High Purity Aluminum", Scripta Met., Vol. 15, p. 161-164, 1981.

53. R. Outlaw, D. Petersen and F. Schmidt, "Diffusion of Hydrogen in Large Grain Aluminum", Scripta Met., Vol. 16, pp. 287-292, 1982.

54. Mears et al., "A Generalized Theory of Stress Corrosion of Alloys," Symp. On SCC of Metals, ASTM/AIME, 1945, pp. 323-339.

55. M.O. Speidel, "Stress Corrosion Cracking of Aluminum Alloys," Met. Trans., Vol. 6A, April 1975, pp. 631-651.

56. R.A. Oriani, P.H. Josephic, Acta Metall. , Vol. 22, 1074,, p. 1065.

57. H. Yukawa, M. Morinaga, and Y. Takahashi, "Interactions Between Hydrogen and Solute Atoms in Aluminum Alloys", Advanced Materials '93, III/A: Computations, Glassy Materials, Microgravity and Non-Destructive Testing, edited by T. Masumoto, et. al., Trans. Mat. Soc. Jpn., Vol. 16A, 1994, pp. 225-228.

58. C.L. Briant, R.P. Messmer, Phil. Mag. Vol. 42, 1980, p.569.

59. S.M. Follies, M.I Baskes and M.S. Daw, Phys. Rev. B, Vol. 33, 1986, p. 7983.

60. D.H. Sherman et al., Trans. AIME, Vol 242, 1968, p. 1775.

61. D.G. Westlake, Trans. ASM, Vol. 62, 1969, p. 1000.

62. S.P. Lynch, Acta Metall. Vol. 36, 1988, p. 2639.

63. S.P. Lynch, J. Mater. Sci. Vol. 21, 1986, p. 692.

64. T.R. Beck, M.J. Blackburn, and M.O. Speidel, "Stress Corrosion Cracking of Titanium Alloys: SCC of Aluminum Alloys, Polarization of Titanium Alloys in HCl and Correlation of Titanium and Aluminum SCC Behavior", Quarterly Progress Report No 11, Contract NAS 7-498, March, 1969.

65. F.S. Bovard, 195th Meeting of The Electrochemical Society, Seattle WA, October 1999.

66. W.D. Vernam and W.A. Anderson, U.S. Patent 3,171,760, March 2, 1965.

67. J.T.Staley, "Effect of Stretching After Solution Heat Treatment on Mechanical Properties of Alloy 70750 Plate", Alcoa Report No. 56-75-HH62, January 7, 1975.

68. B.F. Brown, "The Application of Fracture Mechanics to Stress Corrosion Cracking", Metallurgical Reviews, Review No. 129, 1968, pp. 171-183.

69.   M.V. Hyatt, "Use of Precracked Specimens in Stress Corrosion Testing of High Strength Aluminum Alloys", CORROSION, Vol. 26, No, 11, November 1970, pp. 487-503.

70.   "Standard Practice for Making and Using Precracked Double Cantilever Beam Stress Corrosion Specimens", ASTM Designation: G168-00, Annual Book of ASTM Standards, Vol. 3.02, 2001, pp. 696-705.

71.   M.V. Hyatt and M.O. Speidel, Stress Corrosion Cracking of High Strength Aluminum Alloys, Report No. D6-24840, Boeing, Seattle, WA, 1970.

72.   D.O. Sprowls and B.W. Lifka, "Transgranular SCC in High Strength Al Alloys", ASM-ASTM Symposium, October 19, 1972.

73.   P. Guyot and L. Cottignes, "Precipitation Kinetics, Mechanical Strength and Electrical Conductivity of Al-Zn-Mg-Cu Alloys", Acta Mater., Vol. 44 No. 10, pp. 4161-4167, 1996.

74.   J.W. Christian, "The Theory of Transformations in Metals and Alloys", Intl. Series of Monographs in Meta Physics and Physical Metallurgy, Pergamon Press, 1965, pp. 19, 23 and 471-496.

75.   H. Vehoff, "Hydrogen Related Matrial Problems", in Hydrogen in Metals III, edited by H. Wipf, Springer-Verlag, p. 215-278., 1997.